ABSTRACT

Title of Document: EVALUATING THE SUSCEPTIBILITY OF ELECTRONIC COMPONENTS ASSEMBLED WITH LEADED SOLDER TO FLEXURAL FAILURES, WITH HIGH RATE CONSIDERATIONS.

James Robert Watkins
Doctor of Philosophy, 2008

Directed By: Professor Donald B. Barker
Department of Mechanical Engineering

Multilayer ceramic capacitors (MLCCs) are subjected to high strain rate flexural loading via drop tower and air gun tests, with PWB strain rates ranging from 1/s to 10/s. Three MLCC part sizes, three different manufacturers, and standard and flexible termination parts are included in the study.

Standard termination capacitors failed via the well documented flex crack failure mechanism. However in all cases this crack followed a vertical path not typical of this failure mechanism.

Flexible termination capacitors failed via a newly discovered failure mechanism involving delamination in the end cap metallization between the silver filled epoxy and the nickel-tin plating. For size 1206 parts, this delamination was seen in both end caps, and the part detached from the test board. For size 0603 parts, this delamination occurred in one end cap, while the opposite end cap fractured

though the ceramic in a manner similar to a flex crack. Size 0603 parts also failed via the vertical flex cracks documented in standard termination parts.

All of the documented failures of MLCC devices at PWB strain rates of $\geq 1/s$ occurred at maximum PWB strain values greater than an order of magnitude lower than those seen in lower strain rate testing. This rate dependency of MLCC part failures has vast implications for products intended for high rate environments. Additionally, when the PWB strain rate was increased along with PWB maximum strain, flexible termination capacitors performed worse than their standard termination equivalents. This brings to issue the role of these next generation parts in portable consumer electronic devices as well as other designs with high rate implications.

Ball grid array (BGA) devices are subjected to four point bend tests via a servo-hydraulic testing machine at PWB strain rates $\leq 0.1/s$. The resulting BGA data is found to adhere reasonably well to the Coffin-Manson low cycle fatigue relationship. Independently generated BGA data that differs with respect to many testing variables is plotted alongside the experimental data. The high correlation of the data set indicates the possibility of creating a BGA mechanical failure model that is independent of failure site, package type, and test specifications.

EVALUATING THE SUSCEPTIBILITY OF ELECTRONIC COMPONENTS ASSEMBLED WITH LEADED SOLDER TO FLEXURAL FAILURES, WITH HIGH RATE CONSIDERATIONS.

By

James Robert Watkins

Dissertation submitted to the Faculty of the Graduate School of the
University of Maryland, College Park, in partial fulfillment
of the requirements for the degree of
Doctor of Philosophy
2008

Advisory Committee:
Professor Donald Barker, Chair
Professor Abhijit Dasgupta
Associate Professor Mark Austin
Associate Professor F. Patrick McCluskey
Associate Professor Peter Sandborn

Dedication

To my wife Kelly, who did not know me in my early graduate studies, but supported me through the most difficult year that any Ph.D. student goes through – their last.

I love you.

Acknowledgements

I would like to thank:

- My parents. Without their love and support it would not have been possible for me to complete this work.
- My advisor Dr. Barker, who always gave excellent guidance and support.
- My committee members, Dr. Dasgupta, Dr. Austin, Dr. McCluskey, and Dr. Sandborn.
- My fellow "Team Barker" members. Morrigan and Aaron Johnson, Patrice Gregory, Gil Sharon, Saifa Hasin, Rachel Emmel, Alan Yu, and the "old school crew" as well. Special thanks go to Patrice for help with experimental work, Rachel for lending her cross-sectioning skills, and Gil for FEA assistance.
- Morris Berman at ARL for his assistance with the drop tower experiments.
- Ed Szymanski and Abe Abrahamian at ARL, for their assistance with the air gun experiment.

Table of Contents

List of Tables

List of Figures

List of Acronyms

ARL: Army Research Laboratory

BGA: Ball grid array

CALCE: Center for Advanced Life Cycle Engineering

LCCC: Leadless ceramic chip carrier

MEMS: Microelectromechanical systems

MLCC: Multilayer ceramic capacitor

MOR: Modulus of rupture

OBR: On-board recorder

PWB: Printed wiring board

QFP: Quad flat pack

SOIC: Small outline integrated circuit

SOT: Small outline transistor

Chapter 1: Introduction

Modern electronic components are expected to perform in a very wide range of operating environments. High rate mechanical loading is one of the more demanding environments that electronic components have to contend with. A component can experience high rate loading in the consumer electronic industry from the dropping of a portable electronic device. The military puts much higher demands

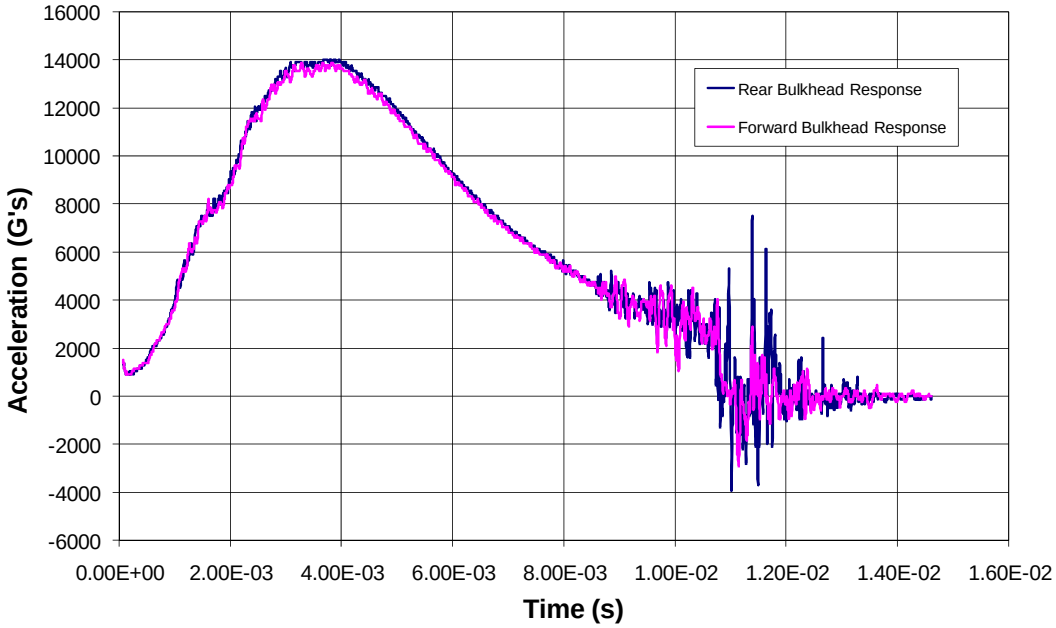

Figure 1.1: Forward and rear bulkhead response data for 155mm round.

on its electronic components. For example, the guidance systems in smart munitions must survive the launch cycle of the round, which can impart 15kGs of acceleration as the round travels down the muzzle, in addition to muzzle exit buffeting pulses in the 5kG range. Figure 1.1 shows an example of the launch profile for a 155mm smart

munition. The pulses due to muzzle exit buffeting occur on the microsecond timeframe, putting them well within the loading rate criteria for a dynamic event.

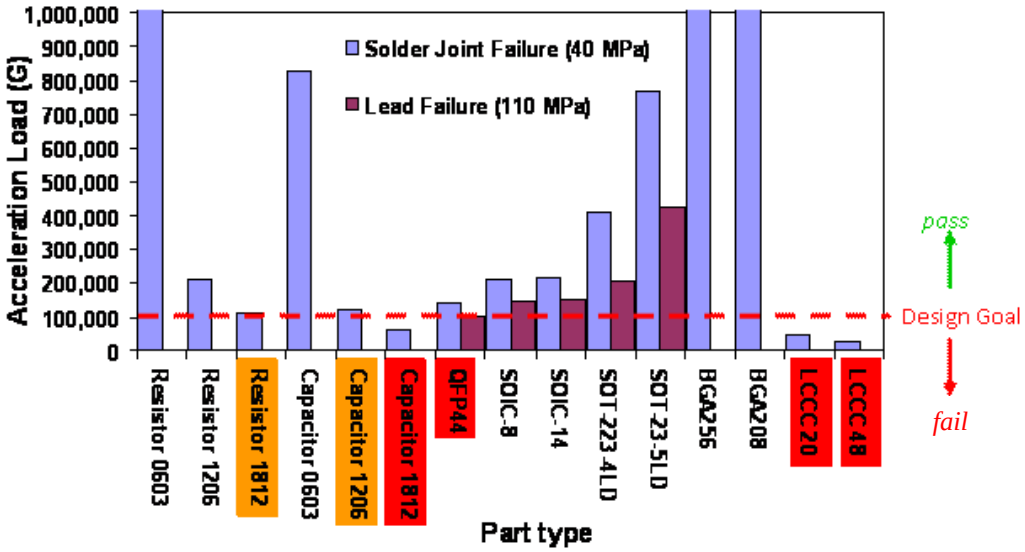

Figure 1.2: Evaluation of different package types for inertial loading.

This project originated with the intention of obtaining a better understanding of how common electronic components perform when subjected to high rate loading. Army Research Lab (ARL) provided funding for the research. Together with ARL a group of components was selected for study. This selection was made by first eliminating components whose mass compared to their board attach area made them susceptible to failure due to inertial effects, and thus unsuitable for high G environments. There are three types of relative motion or loading of component with respect to the substrate that can cause failure. These are motions normal to the substrate, motions transverse to the substrate, and bending motion. Typical failure sites include the component attach (such as in the solder joint or lead), the PWB (such as in a metallization trace, land, or plated through hole/via), and the component itself (such as in the lead frame, wire bonds, or silicon die). To evaluate the potential risk

of failure due to either normal or transverse motion, a simple calculation can be performed by dividing the load due to acceleration by the total cross sectional area of the package attach. This calculation is shown for a variety of components in Figure 1.2. The load is equivalent to the package mass multiplied by the proposed acceleration. Our intention is to see the package survive a maximum acceleration of 100,000 G's. This design goal is labeled in Figure 1.2, and based on this criterion certain packages can be deemed unfit for use in the intended application. Bending was determined to be the critical board motion, since inertial effects were negated by the component selection process. Two of the critical component types were determined to be multilayer ceramic capacitors (MLCCs) and ball grid array (BGA) devices. These two electronic components are the focus of this dissertation.

The experimental agenda first focused on obtaining bending data in the quasi-static rate regime (PWB strain rate ≤ 0.1/s). This testing was done using a four point bend fixture and an MTS servo-hydraulic test machine. Chapter 5 focuses on this work for BGA devices. This testing was also done for capacitors (see Appendix A). The next stage of testing involved qualifying components in the high rate regime (PWB strain rate ≥ 1/s). Capacitors were the focus of this research effort, and the bulk of this dissertation covers the results of this work. A drop tower and an air gun setup were both used to obtain high rate bending data. Chapter 3 of this dissertation focuses on the high rate results for standard termination MLCCs, while chapter 4 addresses flexible termination MLCCs.

Chapters 3, 4, and 5 of this dissertation are written as standalone journal papers, and will be submitted to peer review journals for publication. As such, there

is some repetition in the introductory sections between chapters 3 and 4, which both cover MLCC devices. Chapter 3 will be published first, and is referenced by chapter 4 in a few sections to avoid further repetition.

Chapter 2: Literature Review

Since the majority of this work focuses on MLCC devices, the current state of knowledge on MLCC failures due to board flexure will be addressed here. Flex cracking is the major cause of failure in MLCC devices, as the manufacturing technology has advanced enough to greatly diminish other failure modes [1].

A study was conducted by Hillman, Blattau, and Barker to establish guidelines to help avoid flex cracking in MLCCs [2]. FEA results were combined with published data to create a list of contributors to flex cracking. A reduction in part length was cited as a way to improve reliability, the tradeoff being a reduction in capacitance for a given voltage rating in smaller parts. Switching to a dielectric with a higher fracture toughness was also suggested. The accepted trend for fracture toughness of dielectric materials is C0G > X7R > Z5U. However, C0G is a less stable dielectric and may not be suitable for certain applications. Using a thicker PWB was suggested to reduce the board's susceptibility to flexure. Finally, it was suggested to keep rework to a minimum, since work by Condra et al. demonstrates that reworked MLCCs show consistently higher failure rates than those assembled via standard reflow techniques [3].

The Ph.D. dissertation of N. Blattau developed rapid assessment models to predict failures in leadless chip components subjected to bending loads [4]. The models were developed using manufacturer supplied data, and no in house experimental data was used in their formulation. To create the model, analytic stress

analysis techniques were used to calculate the maximum stress in the ceramic capacitor body for an input PWB strain level. These stress levels were then compared to critical stress values for the ceramic to predict the failure probability of the capacitor. The models have been validated in the low strain rate regime (PWB strain rate ≤ 0.1/s).

An investigation into the flexure strength, or modulus of rupture (MOR), of MLCC devices was conducted by Al-Saffar, Freer, Tribick, and Ward using three point loading tests [5]. The samples evaluated in the experimental study included size 3220 components with a variety of active electrode counts (3, 9, 17, 25, 33, and zero, i.e. blanks). The selected dielectric materials included Z5U and X7R. The parts themselves were evaluated via 3-point loading, meaning that the parts were not attached to a PWB for testing. The X7R dielectric was found to have a higher flexure strength than the Z5U formulation. Flexure strength was found to decrease with increasing specimen thickness. Increasing the number of active electrodes was found to increase the resulting MOR for the X7R dielectric, while no sizable increase was seen for the Z5U dielectric. This was believed to be due to the modulus of elasticity (E) values for electrodes in each of the dielectric types compared to E for the ceramic matrix. Z5U capacitors use a high fire ceramic formulation, and thus noble metals (typically palladium) are essential for the internal electrodes. X7R capacitors use a low fire ceramic formulation, which allows less expensive alloys (typically Ag-Pd with a high silver content) to be used. The Z5U electrode has a value of $E \approx 110$ GPa, while the X7R electrode has a value of $E \approx 84$ GPa. The ceramic matrix for both dielectric types is $E \approx 100$ GPa. Since the E for the X7R electrode is less than

the E for the ceramic, the electrode is able to be more plastic and provides increasing support as the number of electrodes is increased. This is not the case for the Z5U dielectric. Once a crack was initiated, failure analysis showed that for the X7R dielectric the more plastic internal electrodes were able to absorb some of the energy from the advancing fracture wave front. This helps the capacitor to withstand higher loads before failing. The ink laydown concentration, or the thickness of the electrode material, was also varied in experiment. For the X7R dielectric, the MOR was found to decrease with increasing electrode thickness when the part was not fitted with an end termination. This is thought to be due to the higher number of ceramic bonds or "pillars" formed through the electrodes at reduced thicknesses during part production. However, once the part was terminated and annealed, the MOR was found to be consistently high regardless of the electrode thickness.

Recent work has been done to evaluate the effects of isothermal aging on the bending performance of MLCCs by Keimasi, Azarian, and Pecht [6]. Both standard and flexible termination parts were evaluated in this study. Boards were assembled using standard Sn37Pb eutectic solder as well as lead free Sn3.0Ag0.5Cu solder. Three sample groups were prepared with respect to aging, these being 150˚C for 200h, 100˚C for 200h, and un-aged. The samples were then evaluated using a four point bending setup. Results showed that the boards assembled with the lead free solder were less susceptible to flex cracking than those assembled with leaded solder for all aging conditions. This was believed to be due to the lower tensile stresses in the ceramic portion of the MLCC as a result of board flexing, resulting from the different elastic-plastic mechanical properties of the two solders. An additional

contributing factor was believed to be the higher compressive stress in the lower portion of the ceramic where flex cracks originate in the lead free case, due to the higher solidification temperature of the lead free solder. Franken et al. conducted FEA studies to show that the lower portion of the MLCC closest to the PWB is in compression and the top portion is in tension resulting from cooling after solder reflow, and these results are consistent with those findings [7]. With regard to aging, the lead free samples were more significantly affected by the aging process than the leaded samples. The stress relaxation of the solder was believed to reduce the higher compressive stress in the ceramic for the lead free case. It was concluded that applications intended for high temperature environments would not benefit from the increase in reliability from lead free solder, due to the stress relaxation effect which served to make the lead free reliability equal to that of the leaded case. In all cases flexible termination MLCCs outperformed their standard termination equivalents by a sizable margin. This superior performance is evident when comparing the PWB strain at 10% failure of a standard termination MLCC assembled with leaded solder and aged at 100˚C, which was 2220 με, to that of a flexible termination MLCC with the same specifications, which logged only 1 failure at a PWB strain level of 8300 με.

An additional study was conducted by Azarian, Keimasi, and Pecht that investigated the effects of different dielectric materials in addition to leaded versus lead free solder [8]. Two different sizes of MLCCs were evaluated (1812 and 0805), as well as two different dielectric materials (C0G and X7R) and three different part manufacturers. The standard eutectic solder being evaluated was Sn37Pb, and the selected lead free solder was Sn3.0Ag0.5Cu. Again, the performance of lead free

solder (un-aged samples) was superior to that of leaded solder. There was some variation in reliability when comparing parts from different manufacturers assembled using lead free solder. This was attributed to differences in solder fillet geometry and the differences in the compressive stress in the ceramic resulting from reflow. The C0G dielectric material was shown to be greatly superior to X7R. Testing on size 1812 C0G parts yielded no failures at maximum PWB strains of 13000με, where the PWB strain at 10% failure for size 1812 parts of the same manufacturer in X7R dielectric were 1700με and 2300με for leaded and lead free solder, respectively. However, parts containing the C0G dielectric were found to be much more expensive than their X7R equivalents, and were not available in nearly as large a range of capacitance values due to the lower dielectric constant of C0G. The smaller size 0805 parts were found to be more rugged than size 1812 parts. This finding was consistent with results from Prymak and Berganthal, who showed that the susceptibility of an MLCC to flex cracking increases with increasing size [1].

Varghese and Dasgupta established a test methodology to evaluate the durability of surface mount interconnects in a drop environment [9]. The damage parameters selected for use are those of the localized PWB response, these being the PWB strain, strain rate, acceleration, and number of flexural cycles. This contrasts with the traditional method of selecting the loading specifications as damage parameters, such as incident kinetic energy or shock response spectrum. Product level drop tests conducted by Lim et al. [10, 11] and Seah et al. [12] showed a large variation in the strain and acceleration recorded at a given PWB site when the drop orientation of the electronic product was altered. This disparity drove the choice to

select the local PWB response near the failure site for the damage parameters, so as to remove the dependence on the testing conditions. The first step in implementing the proposed test methodology was to gather strain gage and accelerometer data from a drop experiment. This data must be determined to be repeatable in nature, and the number of impact to failure is then logged for the repeatable impact event. Using wavelet analysis, the contribution of each mode in the transient response of the PWB is extracted from the strain and accelerometer data. Rainflow analysis is then used to count the number of cycles and the corresponding amplitudes for each of the modes identified. FEA is then used to identify the stress at the failure site for a given PWB strain, strain rate, and acceleration. Using an appropriate damage model, this stress is related to damage based on the number of cycles recorded for a given PWB mode. This damage is then accumulated for all the identified modes, to arrive at the total damage sustained by the interconnect as a result of the complex drop event. A case study is conducted for a PBGA assembly, in which the test specimen is impacted in both in-plane and out-of-plane orientations. The damage constants are found to agree for both impact orientations, demonstrating that the methodology is independent of boundary conditions and impact orientation.

Varghese and Dasgupta established an experimental approach to characterize the rate dependant failure envelopes and failure site transitions in surface mount devices [13]. A dynamic impact event delivered to a PWB assembly can be characterized by the maximum strain and strain rate measured on the PWB. A test matrix is created that will subject a PBGA test coupon to a range of PWB strains over a range of four orders of magnitude of PWB strain rates (from .001/s to 1/s). A

servo-hydraulic test machine was used for the lower strain rate testing, and a drop tower was used for the higher strain rate testing. Failure analysis was performed after the testing to determine the failure site. Two failure sites were identified, these being the bulk solder and the FR4/copper trace. The FR4/copper trace failure was identified as being either bond pad liftoff or a fracture of the trace between two solder balls on the BGA. A failure site transition zone is identified for some critical combinations of PWB maximum strain and strain rate. Failure envelopes are defined as the range of combinations of maximum PWB strain and PWB strain rate that result in failure at a specific failure site. When low maximum PWB strain is combined with a low PWB strain rate, the failure was found to occur in the bulk solder, and this combination of strain and strain rate is defined by the bulk solder failure envelope. Once these values move beyond the failure site transition zone, the failure occurs in the FR4/copper trace, and this region is defined by the FR4/copper trace failure envelope. A failure map is defined as a plot of PWB maximum strain versus PWB strain rate, on which the failure site transition zone and failure envelopes corresponding to different failure sites are identified. The BGA failure data resulting from these experiments is published in this study, and is used in a comparative study in Chapter 5 of this dissertation.

Methods of qualifying electronic components in high acceleration environments are relevant to this dissertation. Microelectromechanical systems (MEMS) technology is an up and coming field, and a number of studies exist that attempt to qualify a MEMS package in a high acceleration environment. Cheng et al. employed FEA techniques to study the behavior of a packaged MEMS accelerometer

in a high G environment [14]. Attempts were made to obtain the package response resulting from an acceleration impulse load of 100kG. The study was purely FEA based, and mainly dealt with examining the effects of potting materials on the behavior of the package. The study cites the importance of examining the mode shapes and natural frequencies of each package type and of the board structure as a whole, given that the structure will be impulse loaded and should be expected to exhibit dynamic behavior. Brown et al. of ARL conducted a series of experiments to determine the feasibility of using MEMS devices in DOD munitions [15]. Air gun and shock table testing was used to qualify MEMS components for G loads of up to 100kG. Brown provides additional detail concerning this study in his publication entitled "Harsh Military Environments and Microelectromechanical (MEMS) Devices" [16]. The details of the air gun setup used are not provided, but the focus was to subject the MEMS package itself to a high acceleration pulse and to study the sensor response. An applicable point stemming from this work is that the package can experience much higher G level loading than the projectile itself will see, due to the manner in which the load propagates through the projectile structure. Katulka of ARL outlines the typical smart munitions operating conditions that MEMS devices would be expected to survive, as well as presenting some experimental results on silicon carbide MEMS pressure sensors [17].

An interesting study by Guo et al. seeks to optimize the shape and location of BGA solder joints in a high acceleration condition [18]. The definition of high acceleration at 7 G's falls well short of the G levels that are being addressed in this dissertation. Results from the study indicate that the location of the solder joint takes

precedence over the shape of the solder joint in terms of susceptibility to mechanical loading.

Electronic flight data recorders would be expected to have some resiliency to high G loads. Hill-Lindsay et al. outline a digital data recorder that is used in flight testing of anti-tank missile systems and can survive high speed impact where the deceleration magnitude approaches 150kG's [19]. However, the device did not have the limitations in terms of the mounting conditions and packaging requirements that the smart projectile environment must adhere to. The design allowed for potting material to be used, and bending loads were not a significant factor since the boards could be rigidly supported.

Chapter 5 of this dissertation outlines experiments in which PCBs populated with BGA components are subjected to a bending load via a four point bend apparatus. A JEDEC standard exists that outlines the procedure for conducting four point bend tests for the purpose of characterizing the fracture strength of a component's board-level interconnects, and the applicable requirements of this standard were followed for the proposed study [20]. The bend testing of electronic packages for qualification purposes is well documented in the literature [21-34]. Much of the available research has been performed without the goal of attempting to qualify the test package in a high speed dynamic environment. Those that do focus on the loading rate are still not interested in rates on the order of those seen in a launch condition of a smart artillery round. Geng et al. consider the rate of loading in their study, and although the extremely high loading rates that are relevant to this dissertation are not considered, the methodology of the study is relevant [22]. The

study examines the response of BGA devices to three different loading rates. It was noted that as the strain rate was increased, solder joint failure occurred at much less board deflection.

There is a deficit in the literature in the area of the response of MLCC devices to high rate loading. MLCC devices are the weak point of most electronic assemblies, and there is a great need to fully understand their behavior across a broad range of loading rates. This dissertation addresses this deficit and provides fundamental and previously undocumented insight into the performance of this vital electronic component.

Chapter 3: Rate Dependent Failure Behavior for Ceramic Chip Capacitors Subjected to Bending Loads

Introduction

Passive components play a key role in electronic assemblies. Multilayer ceramic capacitor (MLCC) components in particular are prevalent in today's designs, appearing in consumer grade, professional grade, and military products. Many of these electronic assemblies have the potential to experience some degree of high rate

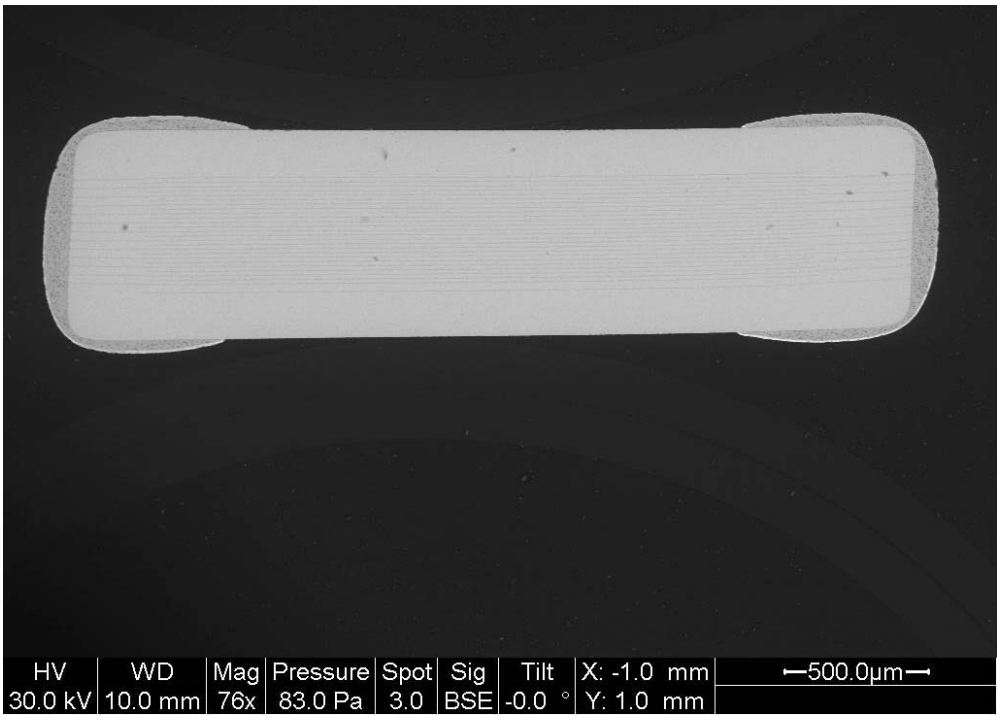

Figure 3.1: Cross section of size 1206 Kemet capacitor.

loading during their life cycle. Examples of this include the dropping of a portable consumer electronic device by the end user and the launch cycle of smart munitions

or near blast loading for military applications. As such, an understanding of the behavior of MLCC devices when subjected to high rate loading is required.

Figure 3.2: Cross section of size 1206 Kemet MLCC, illustrating flex cracking.

Figure 3.1 shows a cross section of a size 1206 MLCC manufactured by Kemet. The component is made up of interlacing metalized layers separated by and encased in a ceramic dielectric. Metal end caps made of a tin-nickel alloy are used as the electrical contacts to the solder pads on the PWB.

This paper will focus on the behavior of MLCC devices when subjected to high rate bending. The loading rates will be quantified as strain rates, with the strain values being taken from the surface of the PWB.

The behavior of MLCC devices when subjected to low to medium rate bending (PWB strain rate < 0.1/s) has been well documented in the literature. The failure mechanism resulting from these loading criteria has been observed to be a diagonal crack in the lower portion of the ceramic near the solder attach (see Figure

3.2). This is the only observed failure mechanism identified in the literature for MLCCs subjected to bending loads.

Experimental Setup

Table 3.1 shows the capacitors that were selected for the experimental study outlined in this paper. The list includes standard termination MLCC capacitors of size 1206, 0603, and 0402.

Manufacturer	Size	Dielectric	Capacitance	Voltage	Tolerance	Termination
AVX	1206	X7R	0.1μF	50V	±10%	standard
Kemet	1206	X7R	0.1μF	50V	±10%	standard
Kemet	0603	X7R	0.1μF	50V	±10%	standard
Kemet	0402	X7R	0.01μF	50V	±10%	standard

Table 3.1: Capacitors selected for experimental evaluation.

The test board used for the experiments is shown in Figure 3.3. A round board was designed so that the perimeter of the board could be clamped to produce a diaphragm-type motion. This configuration was chosen due to the ability to obtain a radial strain distribution on the board, and thus have capacitors subjected to a variety of maximum strains for a single experimental trial. The test board was double sided, and contained 148 parts per side (296 total). Three areas per board side were reserved for strain gage placement. The board diameter was 6 inches. The outer 0.5 inches of

the board was clamped during testing, resulting in an active board area of 5 inches. A nominal 1/16 in. board thickness was selected. Standard 60/40 Sn/Pb eutectic solder

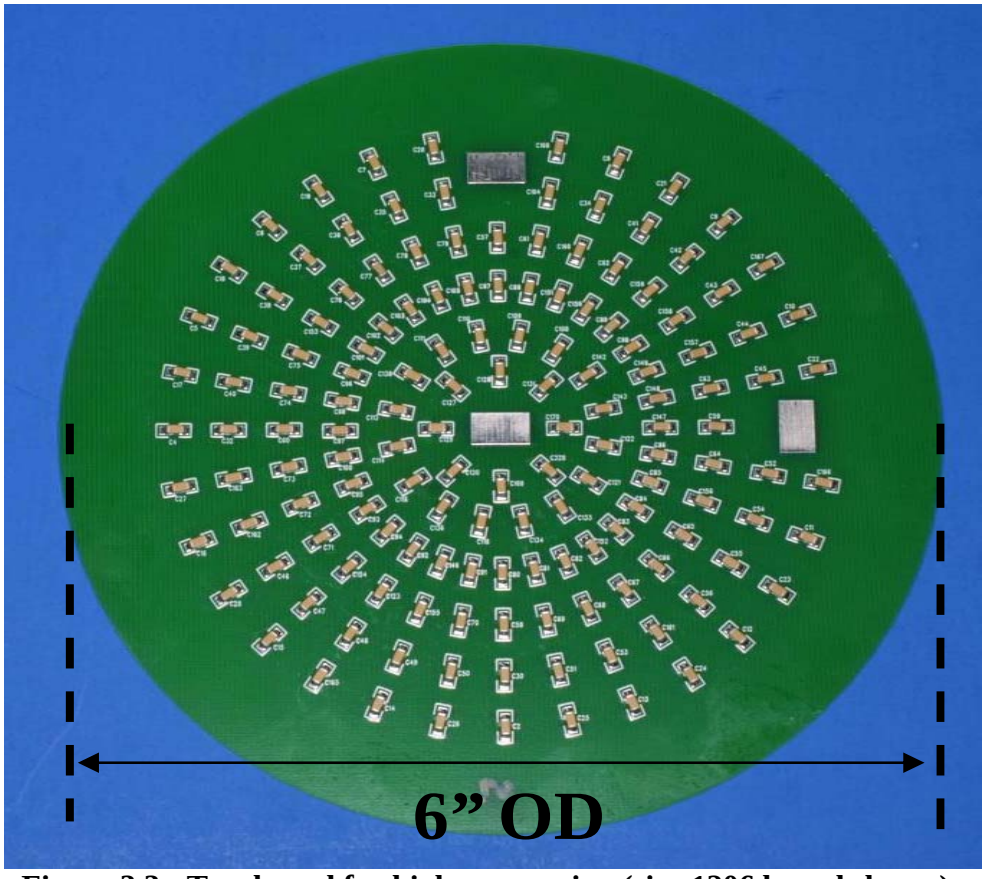

Figure 3.3: Test board for high rate testing (size 1206 board shown).

was used, and the boards were assembled using an automated pick and place machine and a reflow oven at a commercial board assembly shop.

The first experimental method used to obtain high rate failures was an air gun test, which was conducted at the Army Research Lab facility in Adelphi, MD. Figure 3.4 shows a schematic of this test. A test vehicle was designed to house 3 test boards, as well as a data acquisition device (on-board recorder, or OBR). Figure 3.5 shows a schematic of the test vehicle, which was 7 inches in diameter. This test vehicle was inserted into a 300 foot-long launch tube. A vacuum was drawn in the tube, and the

air pressure was raised behind the test vehicle. When the pressure reached a predetermined value the test vehicle was released, at which time it accelerated down

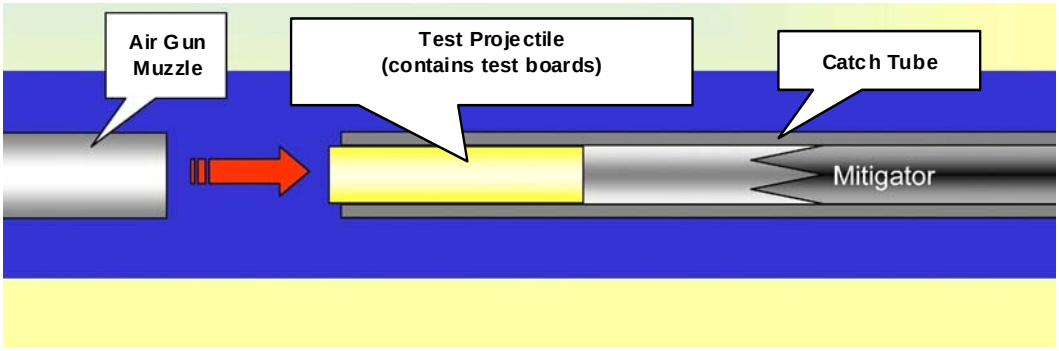

Figure 3.4: Schematic of air gun test.

the launch tube and entered the catch tube. There it impacted a honeycomb mitigator, which was shaped in such a way as to precisely tailor the deceleration profile of the

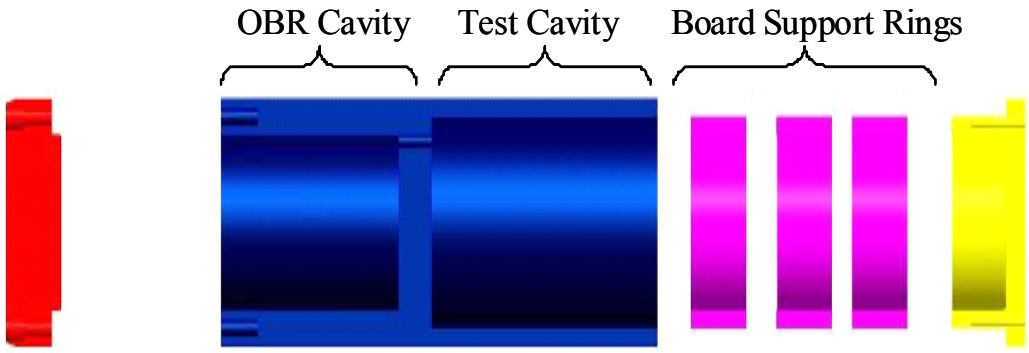

Figure 3.5: Schematic of air gun test vehicle.

test vehicle. This rapid deceleration constituted the test pulse. The OBR was triggered using G-switches which activated the device on its way down the launch tube to allow it to capture the impact event, and switched the device into standby mode once the event was complete. Data collected included three channels of strain data taken from gages in three positions on a single test board, plus one channel of accelerometer data. Only size 1206 components were evaluated in the air gun test.

Prior to the experiment, an FEA study using LS-DYNA was conducted to determine the appropriate acceleration load to achieve a maximum PWB strain on the order of 3500 με for the air gun test. This was the approximate strain value that resulted in size 1206 MLCC failure during bending experiments conducted by the authors at PWB strain rates < 0.1/s (see Appendix A). This maximum strain value was selected as a good starting point for a high rate study of these components.

The second experimental method used to obtain high rate failures was a drop

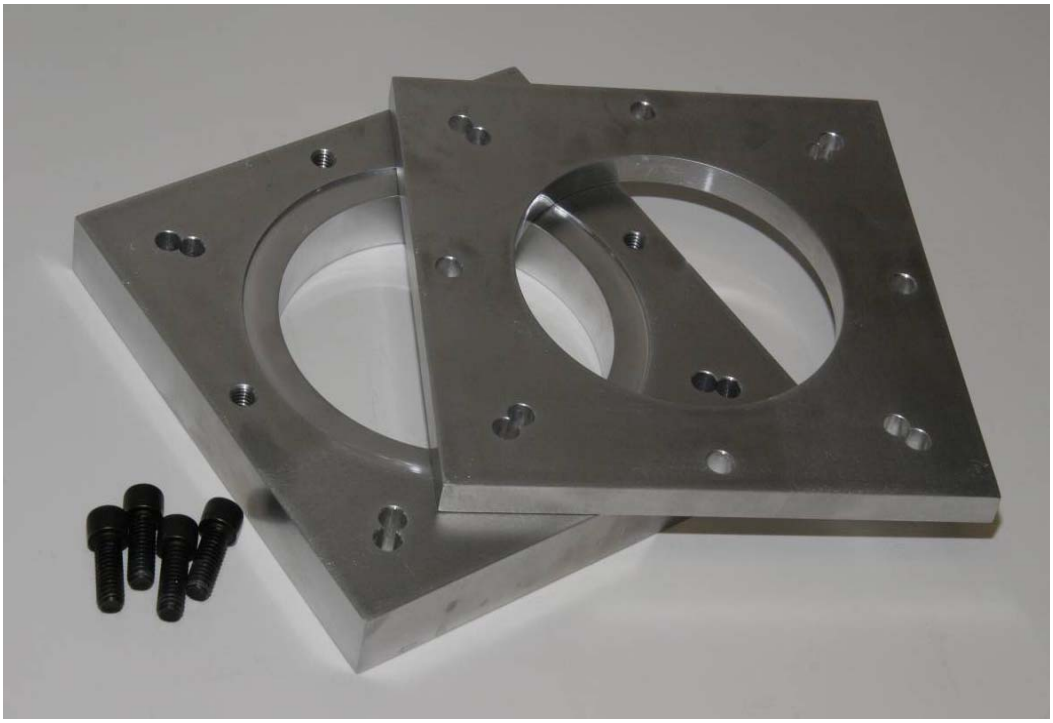

Figure 3.6: Drop tower test fixture.

test. An Impac drop tower was used for these tests. Figure 3.6 shows the fixture that was designed to hold a single round test board for use with the drop tower. This fixture was bolted onto the drop tower table, which was then raised to a predetermined height and released. The table struck the impact surface and was caught on the rebound by the machine, generating a single impact event. The acceleration profile could be tailored by changing the impact media placed between

the drop table and the impact surface. A felt pad was used as the impact media for these experiments. Strain measurements were taken from three locations on the test board, along with accelerometer data. A high speed video camera was also used to document the drop event. The camera was time-synced with the data acquisition system so that the board strain could be determined for any given video frame.

A second support condition for the drop experiment was utilized, in which the

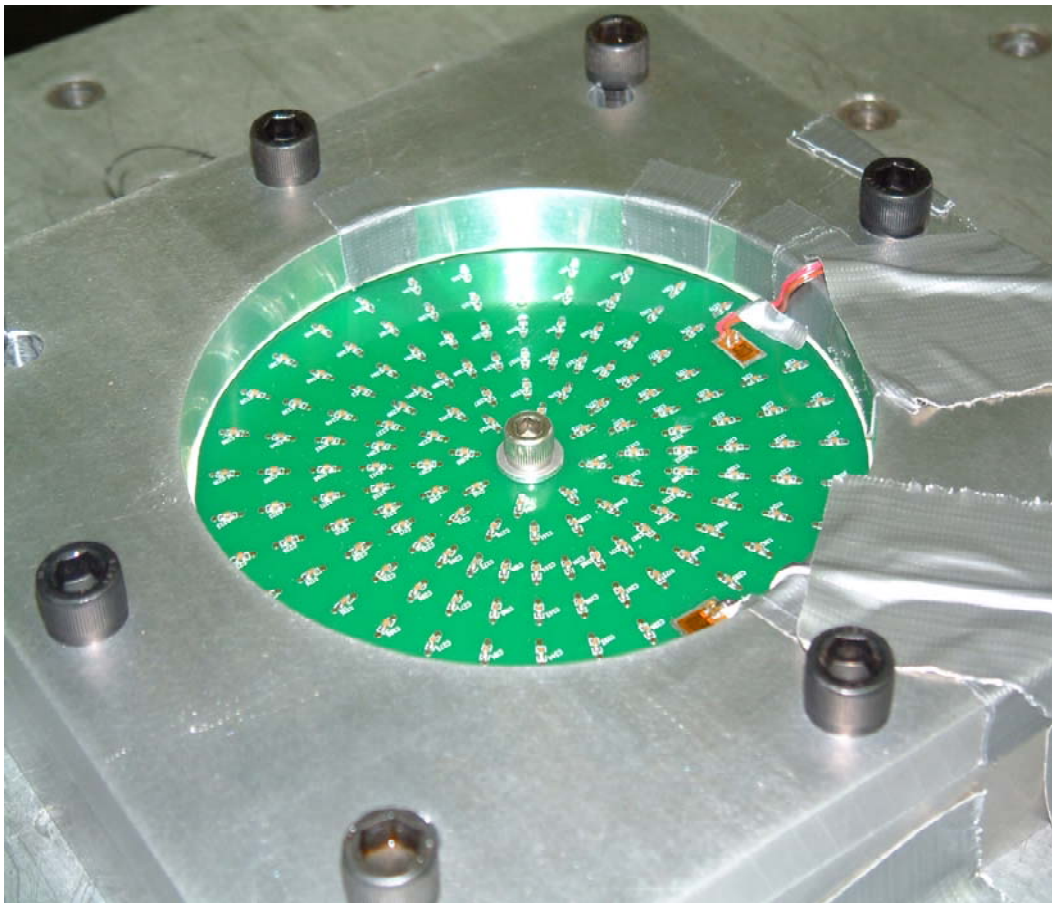

Figure 3.7: Drop support condition with fixed center.

center of the test board was fixed in place with a standoff support. This test condition allowed data to be collected at a higher PWB strain rate than the condition in which the board was only clamped along its perimeter. Figure 3.7 shows the setup for this support condition.

For each of the test methodologies, the capacitors being evaluated were probe tested prior to and after the test to determine failure. Failure was defined as a 10% decrease in capacitance.

Experimental Results

Table 3.2 shows the PWB strain rates calculated from each of the high rate experimental setups outlined in the paper. These PWB strain rate values vary from approximately 1/s to 10/s.

Test Description	Strain Rate
Drop tower test, full diaphragm condition	0.878/s (≈ 1/s)
Drop tower test, board fixed in center	5.93/s (≈ 5/s)
Air gun test	9.69/s (≈ 10/s)

Table 3.2: PWB strain rates for each experimental setup.

Two trials were conducted using the air gun methodology, with peak acceleration pulses of 29kG and 12kG. Figure 3.8 shows the acceleration profile from the 12kG experiment, as calculated using results from high speed video data of the event. In both cases, damage was much more extensive than what was estimated during preliminary experiment simulation. In the 29kG trial, the PWB strain rate was calculated as ≈ 10/s (see Table 3.2). Due to a premature activation of the OBR during experimental setup, no strain data was collected for the 12kG experiment.

Upon reviewing the results from the air gun experiments, a decision was made to move to a simpler and less costly experimental platform. A drop tower experiment was selected, due to its ability to obtain a cleaner acceleration pulse at a lower maximum acceleration amplitude.

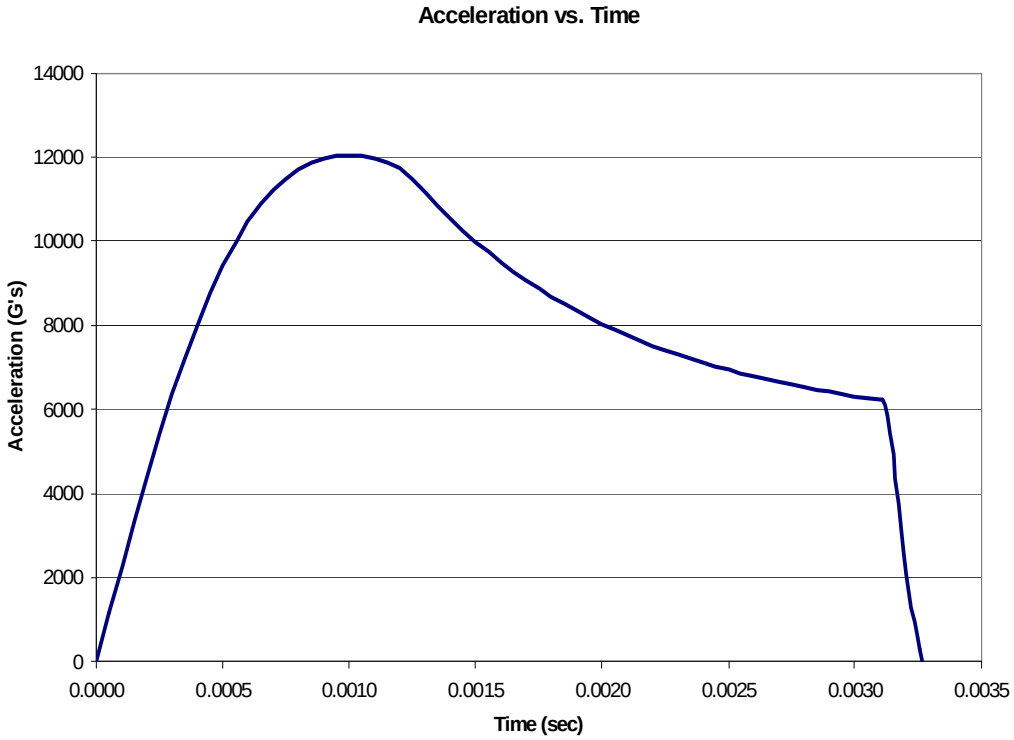

Figure 3.8: Acceleration profile (calculated) of 12kG air gun trial.

The peak acceleration for the drop tower experiments was selected as 5kG, with all experimental trials utilizing this acceleration profile. Figure 3.9 shows an example of the selected acceleration profile. Figure 3.10 shows an example of the PWB strain response, as measured from a strain gage located at the outer edge of the board for the simple diaphragm support condition. The resulting PWB strain rate for this test condition was calculated to be ≈ 1/s (see Table 3.2). The PWB strain rate for the fixed center support condition was calculated to be ≈ 5/s (see Table 3.2). Figure 3.11 shows an example of the PWB strain response, as measured from a strain gage

located at the outer edge of the board for the fixed center support condition. This strain plot shows the same amount of time as Figure 3.10 for the simple diaphragm support condition. However, the number of strain cycles achieved in this time is higher, resulting in a higher strain rate for the fixed center support case. This higher strain rate is a result of the structure being stiffened by the inclusion of the center support.

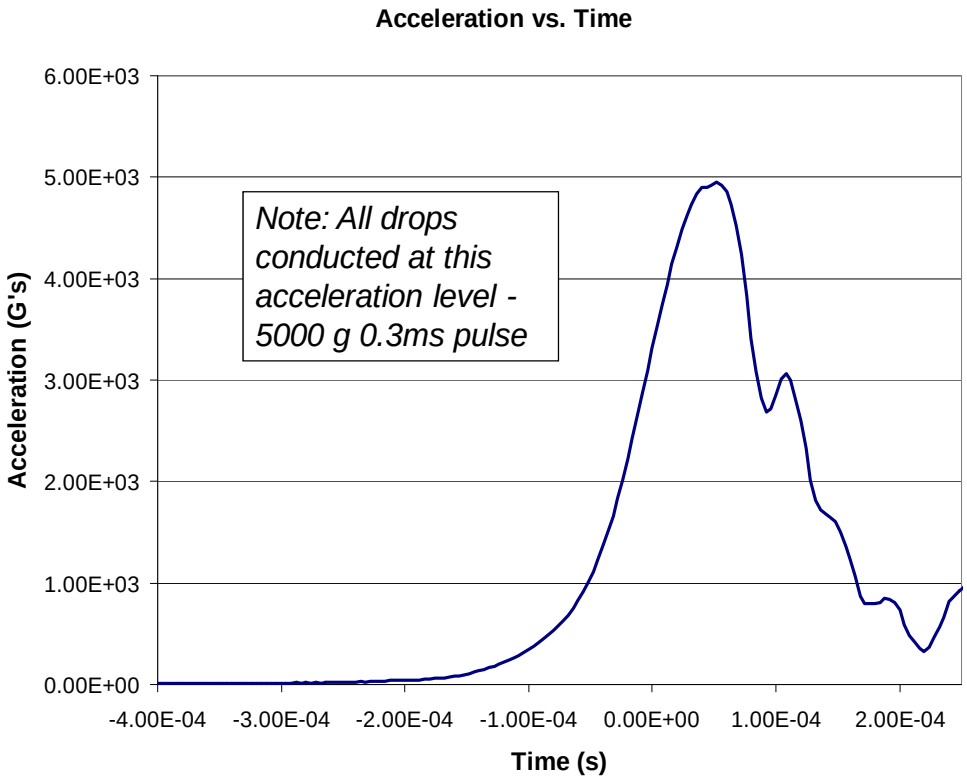

Figure 3.9: Acceleration profile for drop tower tests.

A set of experiments was conducted to determine the strain level experienced by each component mounted on the PWB based on its location. A radius on the PWB was lightly milled to create a smooth surface. Six strain gages were then mounted along the radius, with one gage representing each of the rings of components mounted on the PWB. Dropping these boards allowed the strain response at each component

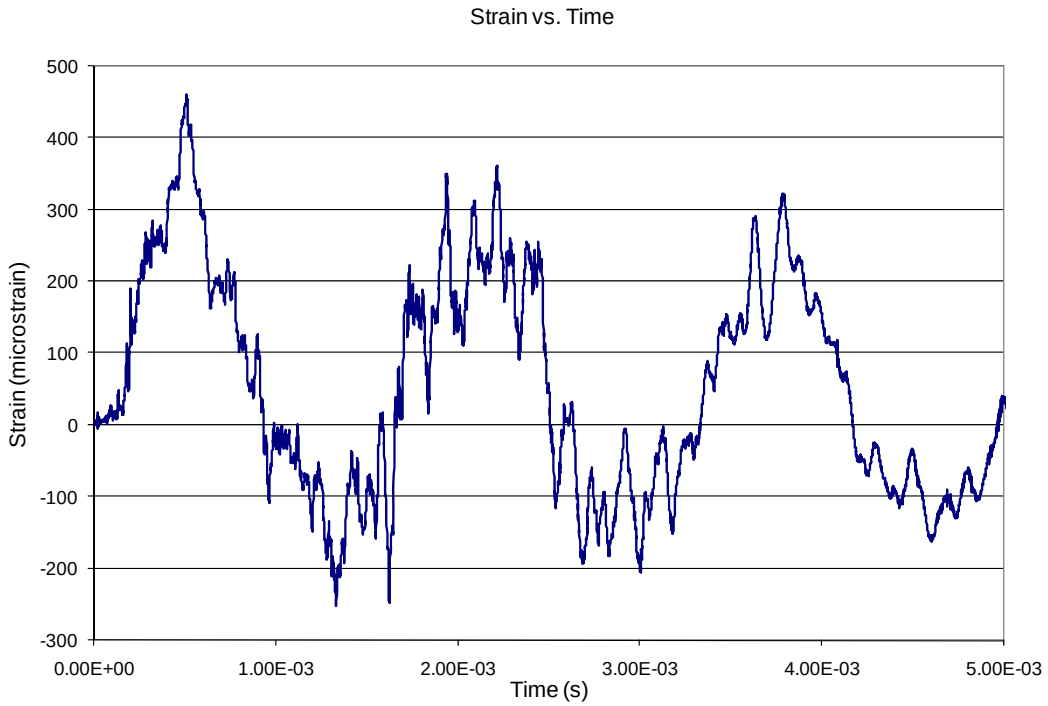

Figure 3.10: Strain response at board edge for full diaphragm condition.

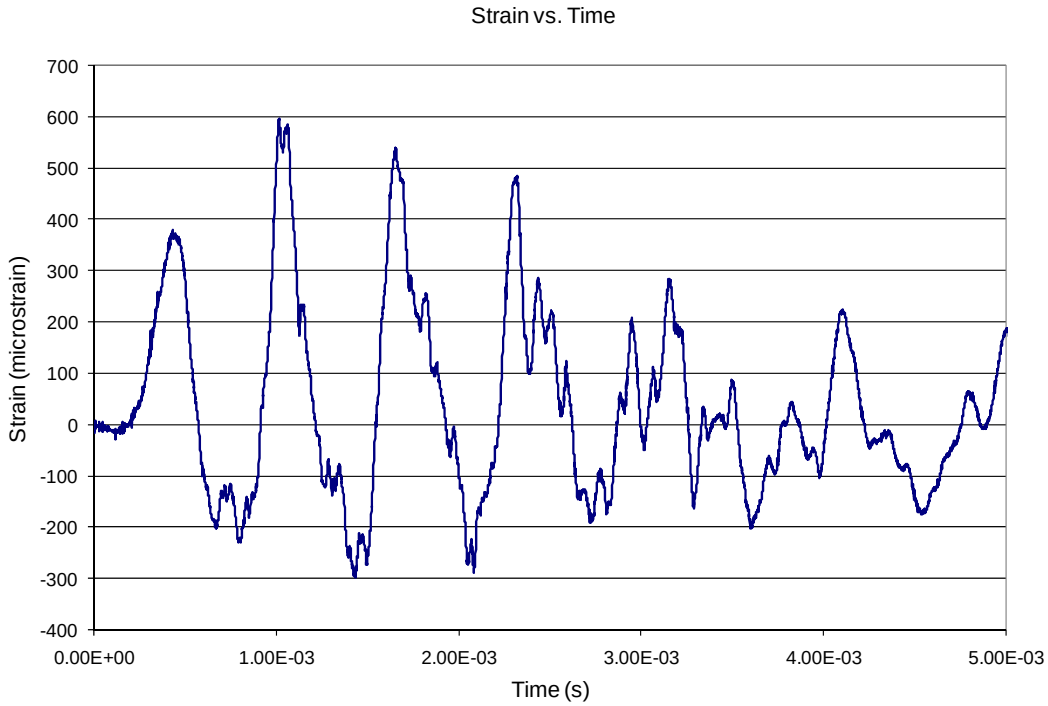

Figure 3.11: Strain response at board edge for fixed center condition.

location to be determined. This test was conducted for both the simple diaphragm and fixed center support conditions. Two trials were run for each support condition,

with the averaged results for maximum strain summarized in Table 3.3. Table 3.3 also shows the radius of each ring and its assigned label. The rings were labels A-F,

Ring ID	Radius (mm)	Free Center Strain (με)	Fixed Center Strain (με)
A	11	450	716
B	18	335	900
C	27	407	1006
D	37	260	737
E	46	354	509
F	56	440	612

Table 3.3: Maximum strain values at each ring position on test board.

with ring A being the smallest ring and ring F being the largest. The results show that the fixed center support condition experienced higher maximum strains than the simple diaphragm support condition for each of the ring locations. The board motion was shown to be radially symmetric in experimental trials by comparing the results of the gages that were placed 90 degrees apart at the edge of the PWB. The two gages showed identical response, verifying the motion to be radially symmetrical.

Table 3.4 gives a summary of the drop tower results. Size 0402 and 0603 parts show great performance advantage over size 1206 parts, with 2% or less failed for both smaller part sizes in both support conditions. The percentage failed for size 1206 Kemet devices roughly doubled when the PWB strain rate was increased from 1/s to 5/s. However, the size 1206 AVX components showed a small improvement for the same increase in PWB strain rate. Since the maximum strain values also increased for the higher strain rate case, it cannot be conclusively determined whether the increase in strain rate or the increase in maximum strain resulted in the higher

number of failures for the size 1206 Kemet parts.

These failures occurred at strain levels well below those corresponding to failure in medium to low rate environments. Examples in the literature, in addition to preliminary testing conducted by the authors, indicate that size 1206 standard

Size	Manufacturer	Center Support?	# Failed	% Failed
0402	Kemet	No	2 / 296	0.7
0603	Kemet	No	2 / 296	0.7
0603	Kemet	No	0 / 296	0.0
1206	Kemet	No	103 / 296	34.8
1206	AVX	No	121 / 296	40.9
0402	Kemet	Yes	6 / 296	2.0
0603	Kemet	Yes	0 / 296	0.0
1206	Kemet	Yes	202 / 296	68.2
1206	AVX	Yes	92 / 296	31.1

Table 3.4: Summary of results for MLCC drop testing.

termination capacitors can survive PWB strains of approximately 3500 με in low to medium rate bending before cracking is seen in the body of the ceramic (see Appendix A). Table 3.3 gives the strain values experienced by capacitors at each radial position, and they are much lower than the documented medium to low rate value of approximately 3500 με for failure. This disparity illustrates the influence of loading rate on the performance of chip capacitors.

The maximum strain that each ring of components on the test board experienced varied, with the maximum strain at each ring location summarized in Table 3.3. The percentage of failed components at each ring location also varied. Figure 3.12 and Figure 3.13 plot the percentage of components failed at each ring

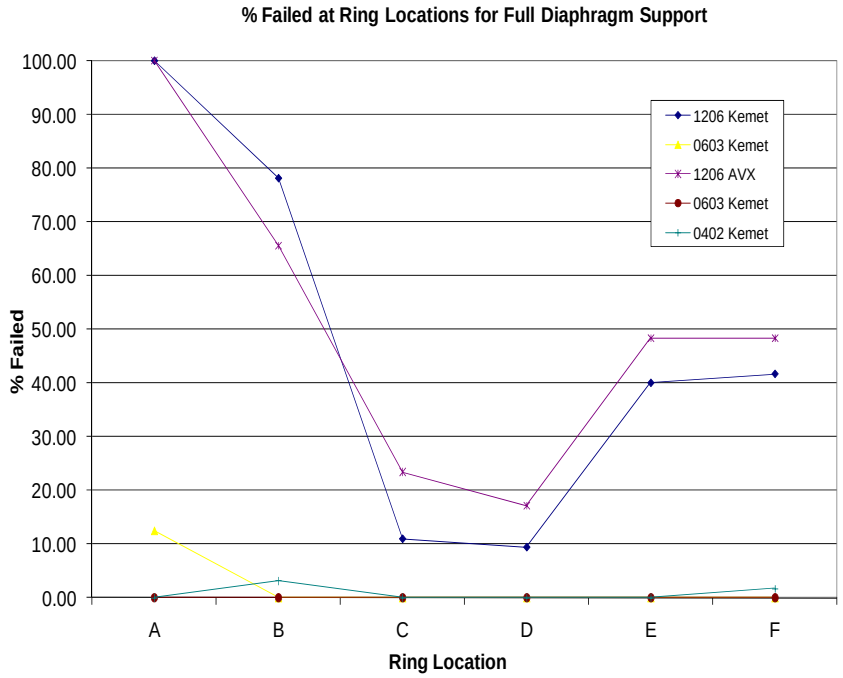

Figure 3.12: Failed components per ring location for diaphragm support.

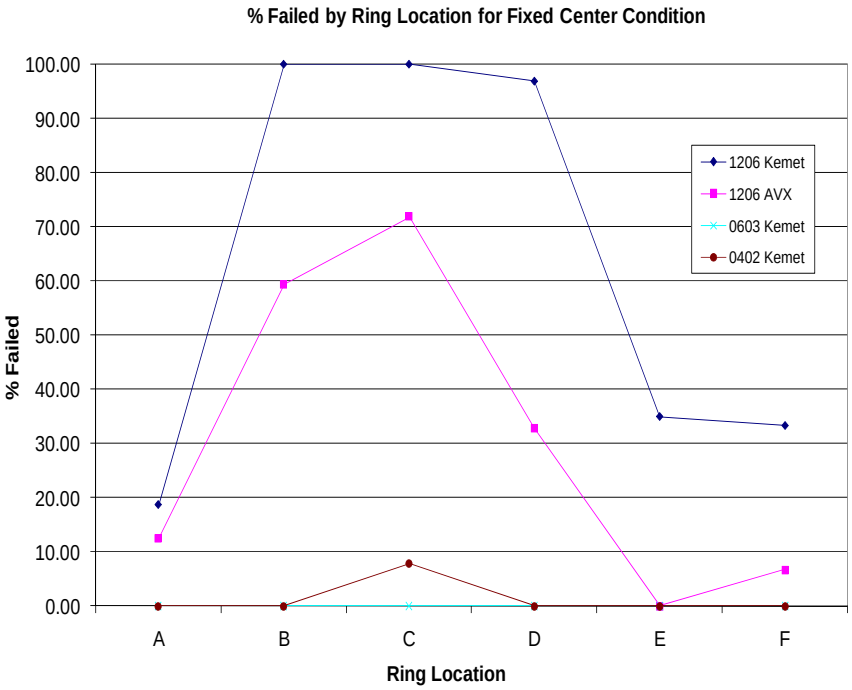

Figure 3.13: Failed components per ring location for fixed center support.

location for each of the experimental trials conducted in the free diaphragm and center clamped support conditions, respectively. Based on this plot it is evident that

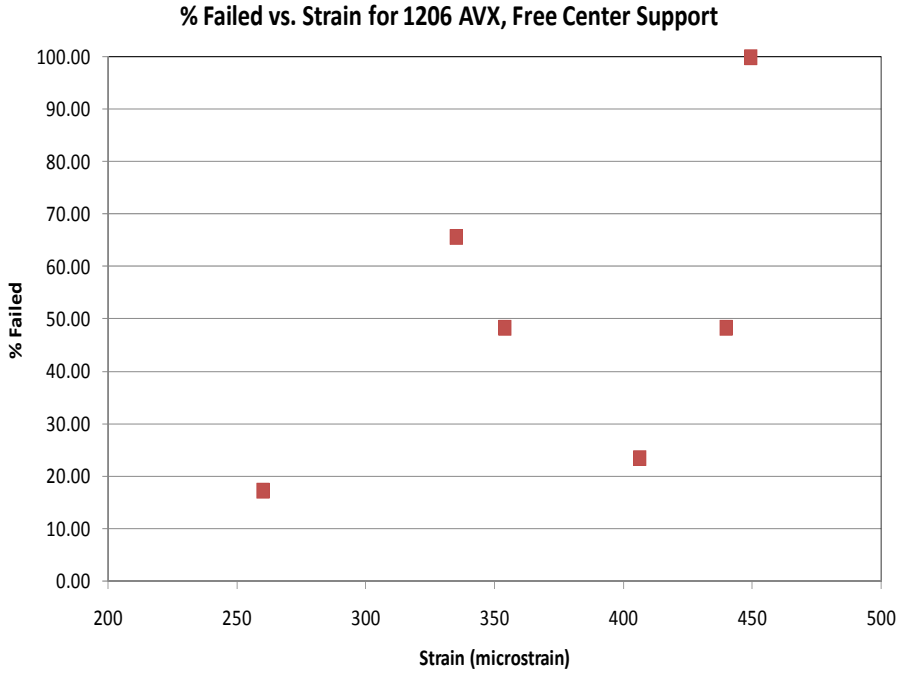

Figure 3.14: Percent failed vs. strain for 1206 AVX, free center.

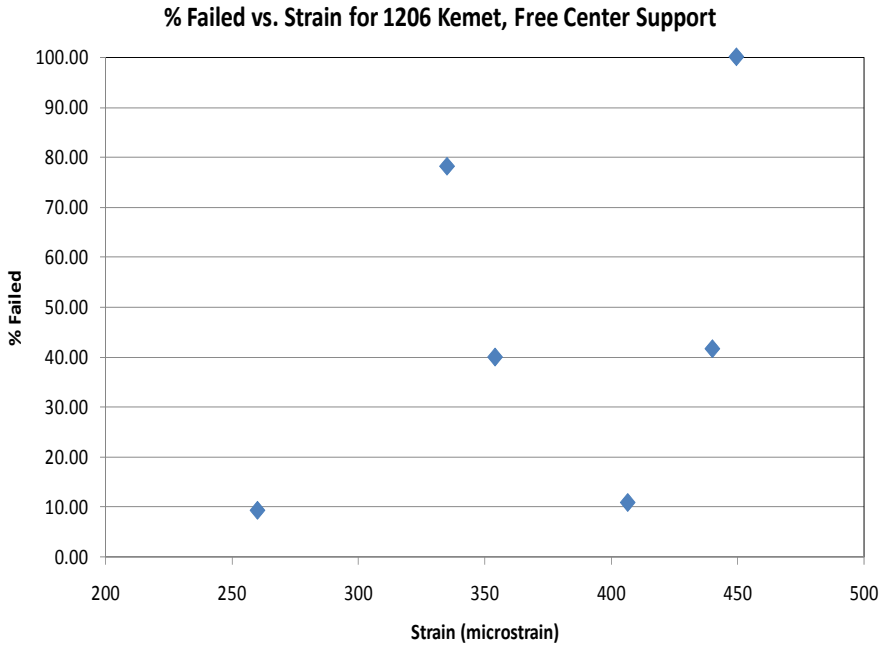

Figure 3.15: Percent failed vs. strain for 1206 Kemet, free center.

the failures follow a pattern across each of the component types. For the free diaphragm support condition, the components lying on the rings closest to the center

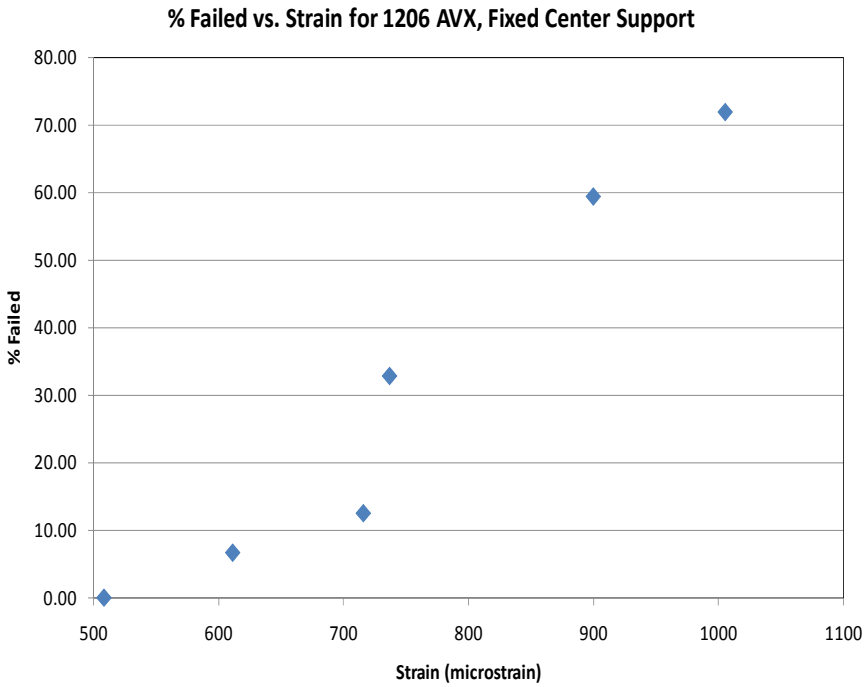

Figure 3.16: Percent failed vs. strain for 1206 AVX, fixed center.

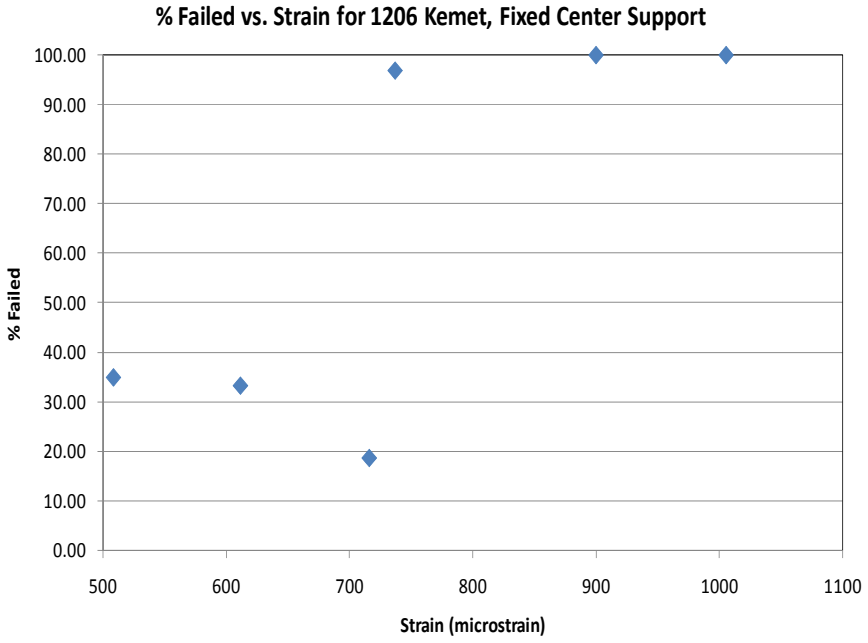

Figure 3.17: Percent failed vs. strain for 1206 Kemet, fixed center.

and the edge of the board experience the most failures. The opposite is true for the center clamped support condition, in which the most failures occur in the rings

midway between the center and the edge of the board. Figures 3.14 and 3.15 plot the percentage of components failed versus strain for the size 1206 component tests performed via the free diaphragm support condition. Figures 3.16 and 3.17 plot the percentage of components failed versus strain for the size 1206 component tests performed via the center clamped support condition. Each data point on these plots represents a maximum strain value at a given ring location and the percentage of components failed at that location. Only the size 1206 components were plotted due to the low incidence of failure among the smaller component sizes. The plot for the AVX devices in the fixed center support condition (Figure 3.16) displays the expected positive trend, illustrating that failures increased with increasing maximum strain. However Figures 3.14 and 3.15, the plots for the free diaphragm support condition, as well as Figure 3.17 for the fixed center support condition, do not show the same convincing positive trend indicative of the percentage of failed components consistently increasing with increasing strain. This result may have been influenced by the presence of additional modes beyond the fundamental mode (simple diaphragm motion) in the dynamic response of the board. The presence of such modes is evident in the transient board response which damps out after 6ms for the free center case. These higher order modes can lead to localized maximums on a given component ring. Additionally, each of the failure percentages shown as data points on all four figures are in realty represented by failure distributions. It may be that component failure was occurring in the tails of the distribution for a number of the components, causing the total failures at each ring to not increase as expected with maximum PWB strain. This phenomenon is further exacerbated by the narrow

range of maximum PWB strain values recorded on the board, with a range of less than 200 microstrain for the free center condition.

To better understand the relationship between the percentage of failures at a given ring location and the maximum strain value at that location for the simple diaphragm support condition, the results were compared to the strain values expected on the board based on analytical calculation. Equations 3.1 and 3.2 give the moments in the radial and theta directions, respectively, for a circular plate with fixed edges under a uniform lateral pressure load [36].

$$M_{rr} = \frac{p_0 a^2}{16}\left(1 + v - (3 + v)\left(\frac{r}{a}\right)^2\right) \tag{3.1}$$

$$M_{\theta\theta} = \frac{p_0 a^2}{16}\left(1 + v - (1 + 3v)\left(\frac{r}{a}\right)^2\right) \tag{3.2}$$

For Equations 3.1 and 3.2, p_0 is the uniform lateral pressure load, a is the radius of the plate, r is the variable plate radius, and v is Poisson's Ratio. Upon calculating the resulting moments in the radial and theta directions, the strain in the radial direction can be calculated using Equation 3.3.

$$\varepsilon_{rr} = M_{rr} - vM_{\theta\theta} \tag{3.3}$$

The uniform pressure load p_0 was adjusted to result in a strain profile that reasonably approximated the maximum strains recorded at each ring location for the high rate drop experiments. The resulting calculated maximum strain distribution was assumed to approximate that of the fundamental mode in the dynamic experiment. The calculated strain distribution is plotted in Figure 3.18 along with the experimentally derived data. The theoretical strain at each of the component ring locations on the board was calculated and then plotted versus the percentage of failed components at

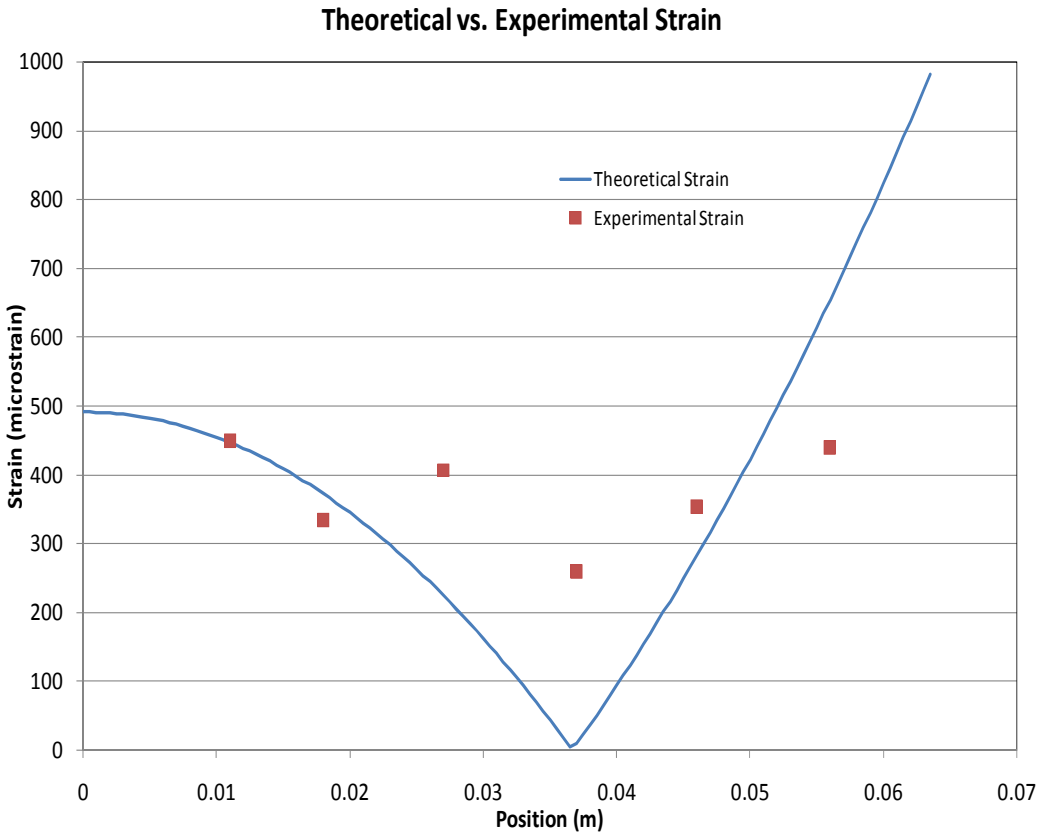

Figure 3.18: Theoretical strain distribution vs. experimental results.

that location. These plots are shown in Figures 3.19 and 3.20. These plots show the percentage of failed components increasing more consistently with increasing strain. This is due to the strain data representing the fundamental mode of the board, which is a better determinant of the strain that the components at a given ring location on the board will see. The experimental strain data was gathered along a single board radius, and is prone to localized maximum strain values due to the influence of higher order modes. The outlier on each of these figures is the last data point, which occurs at roughly 650 με on both plots. This data point represents the strain at the outer edge of the board, which is at the clamped boundary condition. The fact that these values do not fall as expected on the plot can be attributed to the inability of the theoretical result to accurately predict the strain at the boundary condition. These plots also

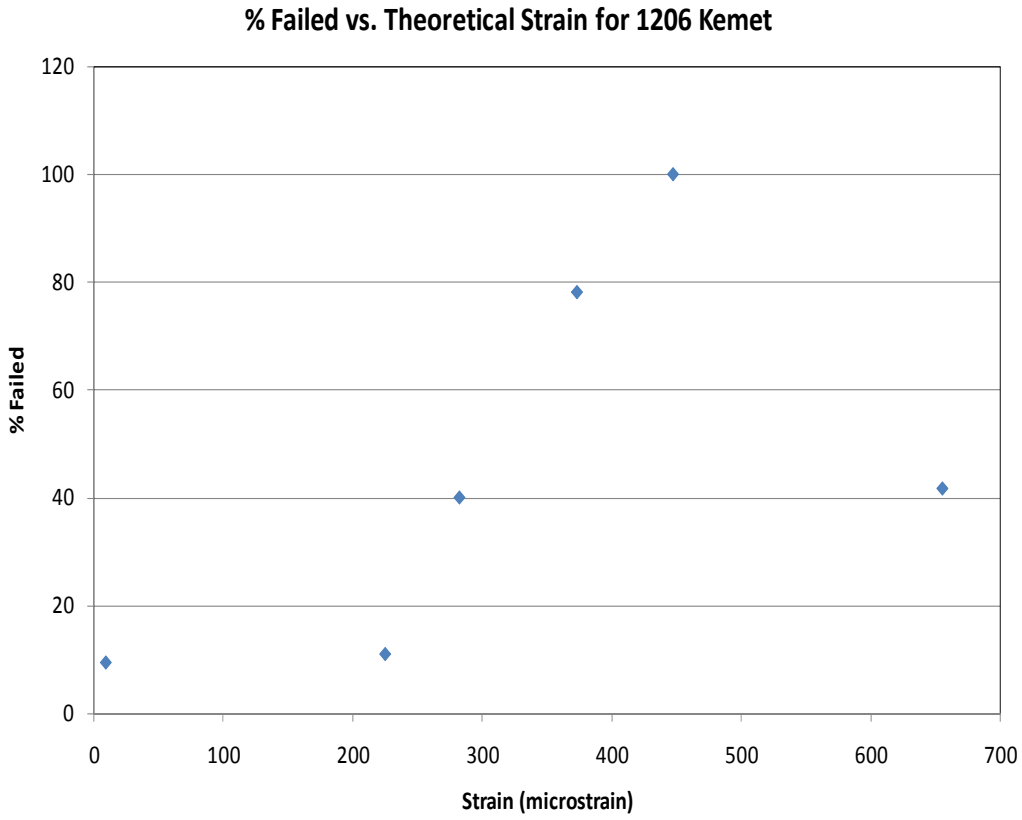

Figure 3.19: Percent failed vs. theoretical strain for 1206 Kemet

show a number of failures at a strain value of nearly zero, due to the fact that this location lies near the sign reversal point on the theoretical strain plot. Although this location is shown to have the lowest amount of failures on the board, its PWB strain value is understated in the theoretical result.

Upon reviewing the high speed videos of the drop events, it was determined that component failure occurred within the first 3 board oscillations in all cases of failure. These first few cycles of board motion represent the transient response, which damped out after 4-5 full cycles of board oscillation. Thus, the possible fatigue influence due to the steady state damped sinusoidal response of the test board after impact can be negated. This effect would have been negligible in any case, since the

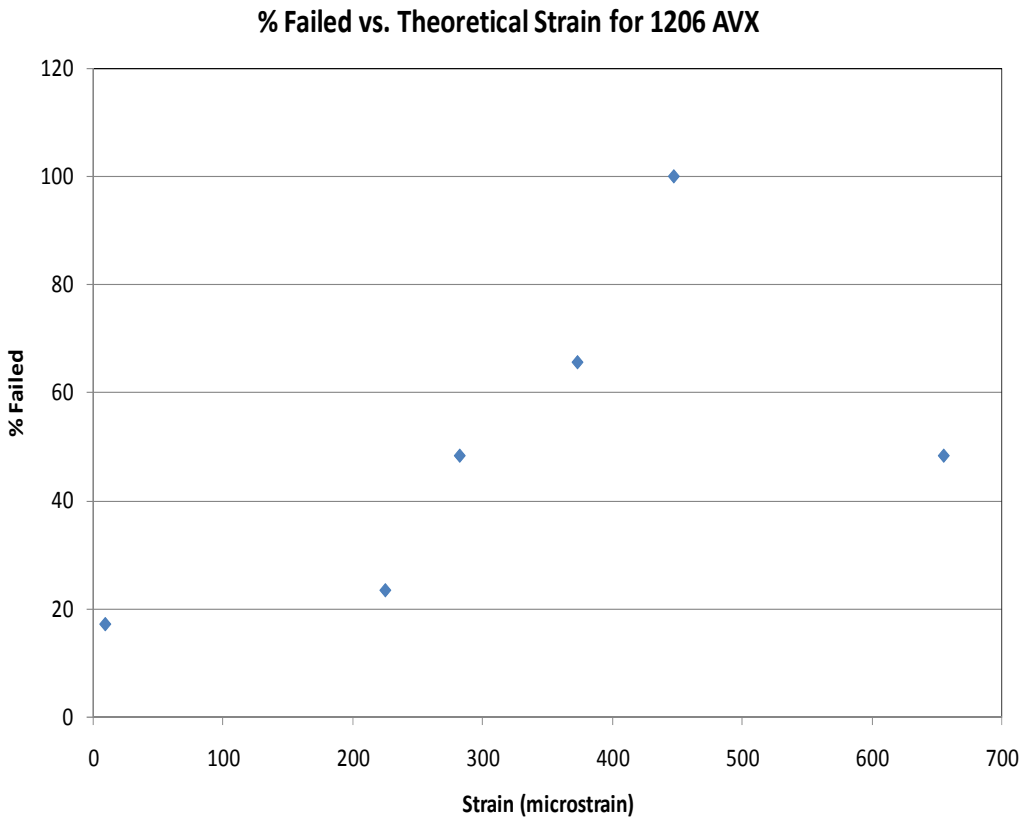

Figure 3.20: Percent failed vs. theoretical strain for 1206 AVX

cracking occurred in the ceramic portion of the MLCC and ceramics are not susceptible to fatigue due to their brittle nature.

Failure Analysis

Failure analysis was conducted for failed components from both the air gun and drop test experiments. In all cases, failure occurred via an unusual failure mechanism, whose defining characteristic is the vertical fracture surface that occurs in the ceramic near the solder attach. Figure 3.21 shows a cross sectioned example of this failure mechanism in a size 1206 AVX component, taken via ESEM. This failure mechanism is similar to the well documented low-to-medium rate failure mechanism

for ceramic capacitors, except that the crack in the failure mechanism observed here is seen to propagate vertically through the capacitor body. The crack angle for the well documented low-to-medium rate failure mechanism has been identified in the literature to be between 30 and 70 degrees, measured from the plane of the PWB [6]. The site of crack initiation is the same for both failure mechanisms. It is believed that the failure mechanism observed here is not a new mechanism but rather a variant of the classic flex cracking failure mechanism.

In some cases of failure, once the part cracked completely through the ceramic as shown in Figure 3.21, it then lifted away from the board by cracking through the ceramic at the opposite solder attach. This phenomenon is shown in Figure 3.22.

In all documented instances of failure, the failure was observed to occur via the failure mechanism exhibiting the vertical cracking. This is true for all of the MLCC sizes evaluated in this study (size 1206, 0603, and 0402). Figure 3.23 shows a 0603 Kemet part with a visible crack in the upper portion of the ceramic near the solder attach. Figure 3.24 shows a vertical crack through the ceramic on a size 0402 Kemet part.

Capacitor failure in the high rate experiments outlined in this paper ($\geq$ 1/s PWB strain rate) occurred at a much lower maximum strain value than the well-documented failure regime for medium to low-rate failures. As mentioned above, literature review in addition to bending experiments conducted by the authors at PWB strain rates $\leq$ 0.1/s confirms the occurrence failure in size 1206 MLCC devices at strain levels on the order of 3500 $\mu\varepsilon$ (see Appendix A). However, the new failure mechanism that has been documented here occurs at strain values as low as 260 $\mu\varepsilon$;

an over one order of magnitude lower value. This phenomenon explains why the air gun testing in this study resulted in much higher failure rates than those predicted using LS-DYNA simulation, since failure was occurring via the new failure mechanism at a much lower than expected maximum strain value. Additionally, these results raise concerns about the use of MLCC devices in applications that will experience high-rate loading, due to their unexpected decrease in ability to survive a high-rate PWB deflection event.

A hypothesis was developed to explain the occurrence of failure at lower maximum PWB strain values than those observed in lower rate experiments, as well as the observed failure mechanism in which the part lifts up from the PWB after first cracking at the opposite attach. Failure at a lower maximum PWB strain value is believed to be due to strain rate hardening in the solder. Solder is known to have strain rate dependent material properties. In lower rate testing, the solder behaves more compliantly and mitigates a larger amount of stress in the ceramic. However as the loading rate is increased, strain hardening in the solder increases its effective elastic modulus which results in a higher stress load transferred to the ceramic. Thus, the component fails at a lower maximum PWB strain value.

The fracture at the opposite attach which causes the part to lift up from the PWB or break away completely can be attributed to inertial effects. Once the part has fractured through the ceramic near the first attach, the part can be approximated as a beam fixed at one end with a uniform load applied to it. Using beam theory, the stress at the opposite attach can then be approximated. To illustrate this concept, the size 1206 MLCC part will be used as an example. Using a microbalance, the weight

of the part was determined to be 0.0369 g. The dimensions of the part are length = 0.126 in., width = 0.063 in., and height = 0.063 in. The moment of inertia of the part, I, can be calculated using Equation 3.4.

$$I = \frac{1}{12} bh^3 \tag{3.4}$$

The resulting moment of inertia for the part is 5.464e-13 m^4. The Young's modulus, E, of the ceramic is roughly 30 GPa. The line pressure load on the beam due to the increased gravitational load is calculated using Equation 3.5.

$$P = \frac{mg}{L} \tag{3.5}$$

Here, m is the part mass, g is the gravitational load, and L is the part length. The gravitational load here was approximated to be 10 kG on the PWB, based on an amplification factor of 2 over the measured table peak acceleration of 5 kG. The resulting line pressure load is 1130 N/m. The maximum moment in the beam can then be calculated using Equation 3.6.

$$M_{max} = \frac{L^2 P}{2} \tag{3.6}$$

The resulting maximum moment is calculated to be 0.00579 N-m. The resulting maximum stress at the attach can then be calculated using Equation 3.7, where c is the distance from the neutral axis to the extreme fibers, or height/2.

$$\sigma_{max} = |M_{max}| \frac{c}{I} \tag{3.7}$$

The resulting maximum stress is calculated to be 8.35 MPa. This stress is thought to play a role in the fracture at the attach opposite that of the first fracture for the part. An amplification factor of 2 was selected here to represent the acceleration on the

board based on the measured value on the drop table, but this factor may actually be higher.

Verification of Experiment

The test boards used for these experiments were double sided boards, with components directly opposite each other on both board sides. This test board design was thought to possibly play a role in the experimental results, due to the localized stiffening effects of components on the opposite board side. To rule out the possibility of this influence, both a FEA study and a set of experiments were conducted.

A FEA study was conducted to investigate the point of highest stress in the ceramic, and thus the likely area for crack initiation. The crack initiation point for the observed failure mechanism is in the lower portion of the ceramic near the solder attach. A FEA model was constructed to determine whether this stress concentration occurred in the same location for a double sided test board like the one used in this study. The model used 2-dimensional 8-noded structural solid elements. A single component was located on the test board and the board was loaded at its end with a downward force to simulate a bending moment. The supplied force generated a PWB surface strain of roughly 3000 με. Figure 3.25 shows the model for the single sided board case, created as a comparison point for the study. The expected stress concentration in the lower portion of the ceramic near the solder fillet is clearly visible in the magnified view shown in Figure 3.26. Figure 3.27 shows the model for the double sided board case, which was created by simply mirroring the component

on the opposite board side. Again, the stress concentration occurs in the lower portion of the ceramic near the solder fillet, as can be seen in the magnified view shown in Figure 3.28. This illustrates that the use of a double sided test board did not have an effect on the crack initiation site in the ceramic.

An experimental effort was also conducted to determine the effect of the test board and fixture design on the high speed experimental results. Testing was done using an MTS servo-hydraulic material testing machine at a PWB strain rate of 0.1/s. The goal was to determine if the vertical fracture surface in the ceramic appeared in slower rate testing when the experimental setup was held constant, and thus determine if a factor inherent in the experimental design itself resulted in the vertical fracture surface. The test board and test fixture used in the drop tower tests were used in these experiments. The test board was positioned on the lower plate of the test fixture, and was not clamped with the top plate as it was in the drop test setup. The MTS machine was fitted with a small plate that pressed on a ring that sat on the test board. The ring outer diameter was 4 inches, with a 0.5 inch wall thickness. The resulting board motion mimicked the diaphragm motion seen in the drop tower testing. Figure 3.29 shows the test setup. PWB strain was monitored during the test, and capacitors were probe tested prior to and after the test to determine failure. Failure was defined as a 10% decrease in capacitance, as it was also defined in the drop tower testing. Only size 1206 components were evaluated in this experiment, and both the Kemet and AVX parts used in the drop tower testing were selected.

A single sided test board was evaluated in addition to a double sided board for both components. The single sided board was the same round test board seen in

Figure 3.3, but was only populated on one side. A single sided board was selected for evaluation in addition to the double sided board configuration used in the drop tower testing to determine the influence, if any, of having components located directly opposite one another on both board sides on test results. The test loaded the components in tension only, with a full test cycle being measured from zero to tension and back to zero.

The test was displacement controlled, and each board was subjected to a series of increasing displacement loads and probed after each trail until failures were achieved. A single strain gage was located in the center of each the test board on the designated strain gage pad. The strain measured during the test was correlated with the strain on a calibration board that was fitted with a strain gage in its center, as well as at each ring location on a single radius. In this way, the strain that each ring of components experienced at each displacement level was ascertained. Table 3.5 shows the strain levels at each ring location corresponding with each displacement level that was used in the experiment.

Table 3.6 shows the number of failures for each board type, the displacement level that resulted in those failures, and the location of the failures on the test board. All of the documented failures occurred in ring E on the side of the board where the components experienced tensile loading. This location was directly opposite of the point of load application, as they were located opposite of where the ring fixture applied the displacement load to the test board. Table 3.5 shows that the strain at this location was the highest on the board, which explains the occurrence of failures there. The load applied to one of the test boards, the Kemet double sided board, was

increased until failures were documented at ring D as well. This was done to allow for failure analysis on components lying away from the point of load application, in case that location experienced abnormalities in failure mode or mechanism.

Failure analysis was performed on all of the documented failures. In all cases, failure occurred via the same failure mechanism documented for the high rate drop testing. Figure 3.30 shows a cross section of a failed KEMET component from the testing. The same vertical crack through the ceramic near the solder attach is visible. Comparing the results from the single sided and double sided boards, it was concluded that the double sided boards had no effect on component performance. This was because both the maximum strain at failure and the failure mechanism were identical for both board configurations.

In summary, it was initially believed that the higher loading rates in the drop tower experiments led to the occurrence of the unusual vertical cracks in the ceramic. However, the low rate bending tests performed with the same board configuration resulted in the same failure mechanism for the components, proving that the loading rate did not play a role.

The diaphragm type loading of the test board was then thought to possibly be the cause of the vertical cracking in the ceramic. To evaluate this influence, material from a circular test board was cut away on the top and bottom. This board is shown in Figure 3.31. The board was then tested using a standard four point fixture attached to an MTS servo-hydraulic test machine. Strain was monitored in the center of the board, and the board was displacement loaded and probe tested after each load cycle to determine part failure. Failure was defined as a 10% decrease in capacitance, as it

was also defined in all the experimental work outlined in this paper. The critical component region was the region of the board where the components were oriented lengthwise parallel to the length dimension of the board. These critical components are located inside the red triangles in Figure 3.31. The board was loaded at a PWB strain rate of 0.1 /s. Two components in the critical region failed at 3507 με, and two additional failures were recorded at 4190 με. These strain values correlate well with the values for failure from the MTS diaphragm testing. Failure analysis was conducted on the failed parts, and it was determined that the failures occurred via the same failure mechanism characterized by the vertical cracking of the ceramic. Thus the diaphragm loading condition was not a cause of the vertical cracking in the ceramic.

Conclusion

The failure of MLCC devices at high loading rates (PWB strain rate ≥ 1/s) occurs at a maximum strain value that is oven an order of magnitude lower than that documented for low to medium-rate failures. Component size is a driving factor for high rate failures, as size 0603 and 0402 ceramic capacitors show a great performance advantage over size 1206 capacitors.

An unusual variation on the classic flex cracking failure mechanism for MLCC devices has been observed. This failure mechanism is characterized by a vertical crack through the ceramic near the solder attach. Extensive testing was performed to determine the influence of a number of possible drivers on this failure mechanism. Factors eliminated as possible causes include loading rate, the use of a

double sided test board versus single sided, and the displacement profile of the test board (diaphragm versus simple linear bending profile).

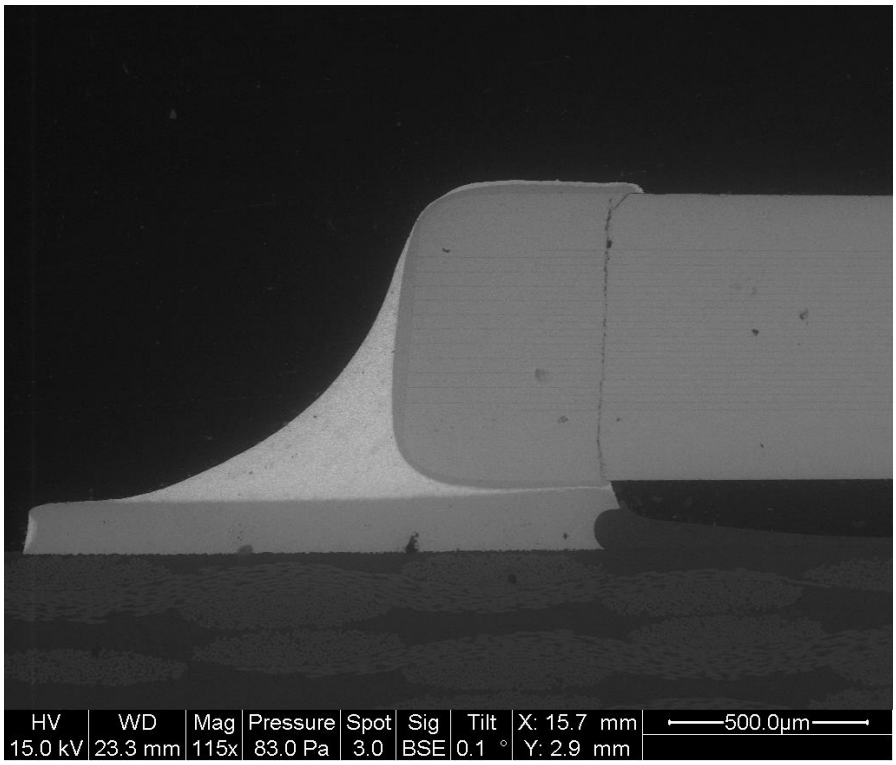

Figure 3.21: Cross section of failed 1206 AVX MLCC, with vertical crack.

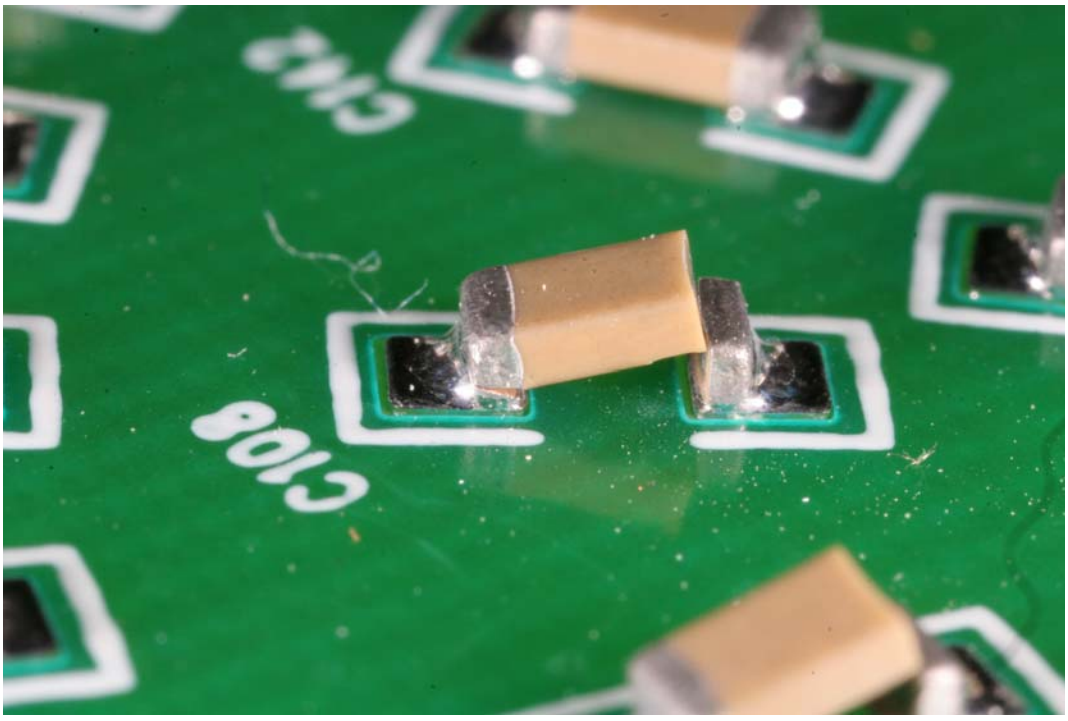

Figure 3.22: 1206 AVX MLCC lifting away from PWB.

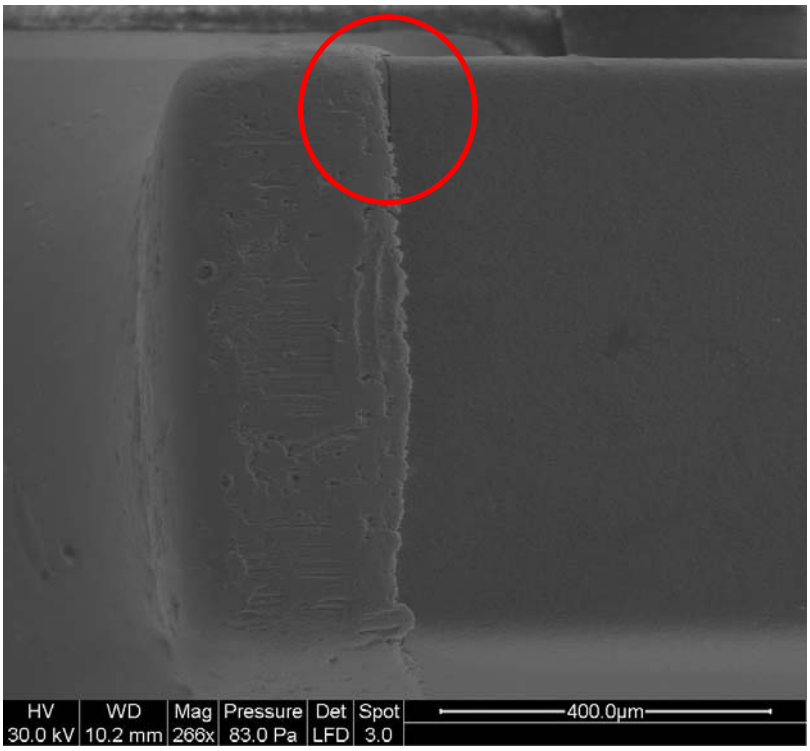

Figure 3.23: Kemet 0603 MLCC with visible crack in top ceramic surface.

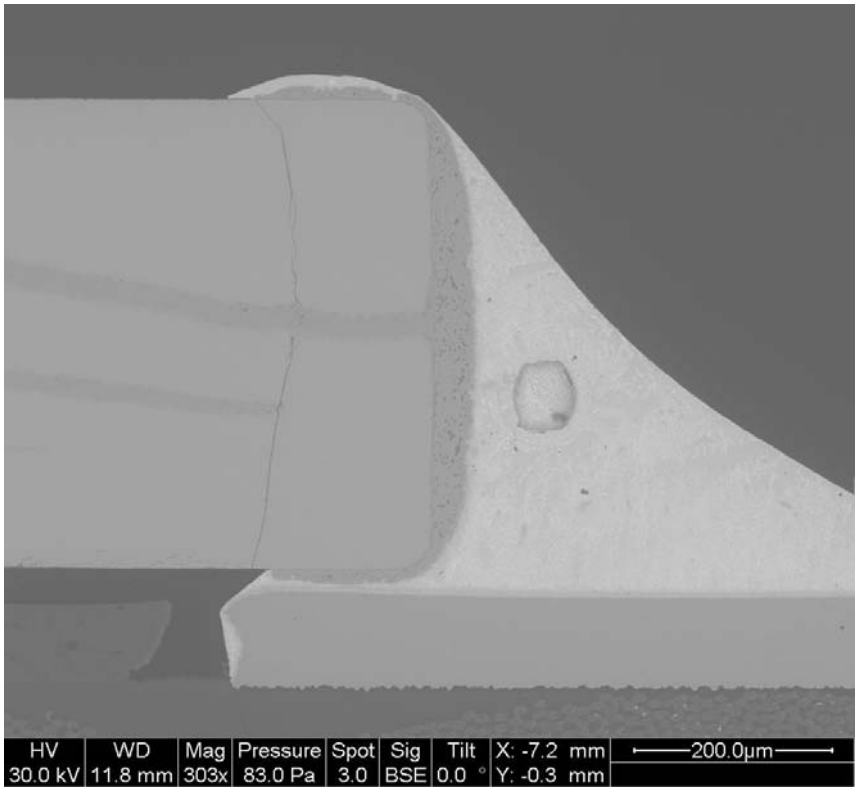

Figure 3.24: Kemet 0402 MLCC with vertical crack through ceramic.

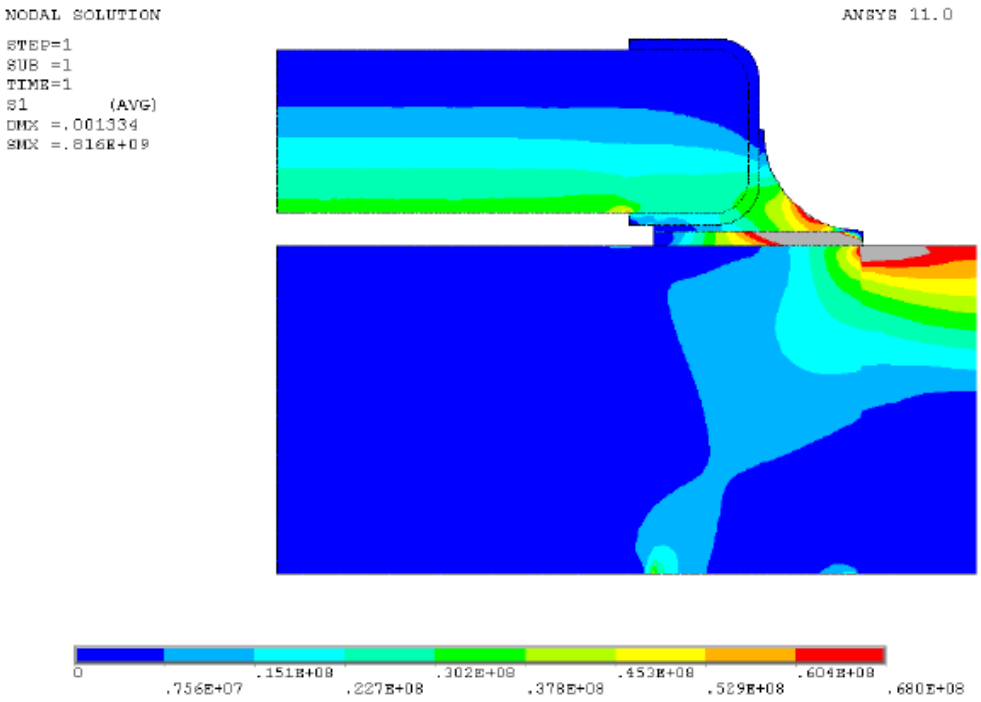

Figure 3.25: FEA model of MLCC component mounted on one board side.

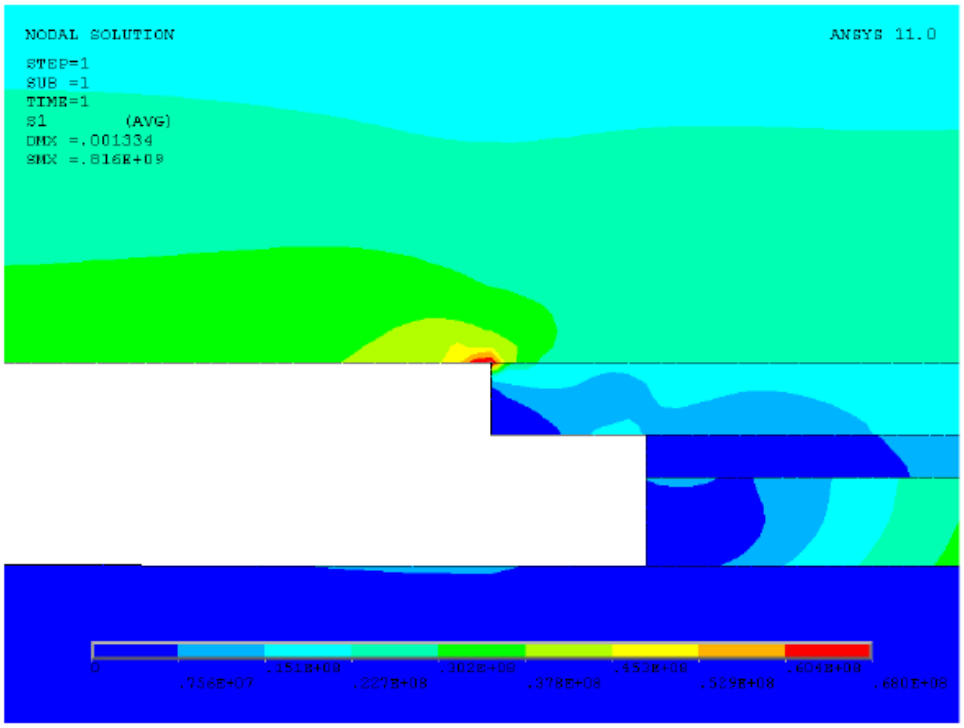

Figure 3.26: Magnified view of critical stress region, single sided case.

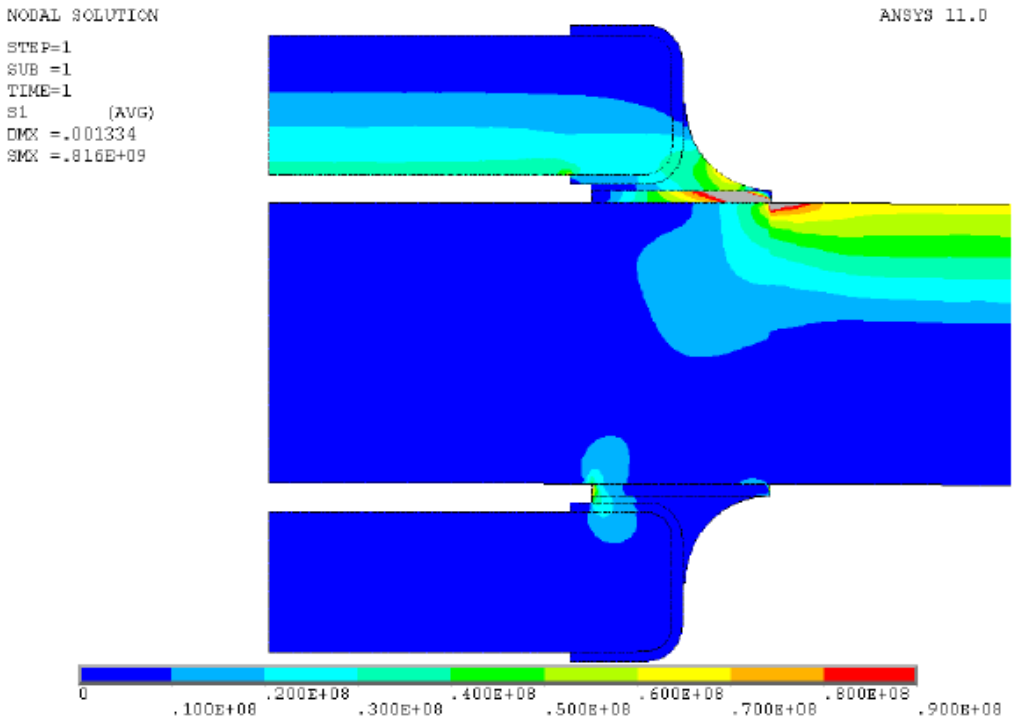

Figure 3.27: FEA model of MLCC component mounted on both board sides.

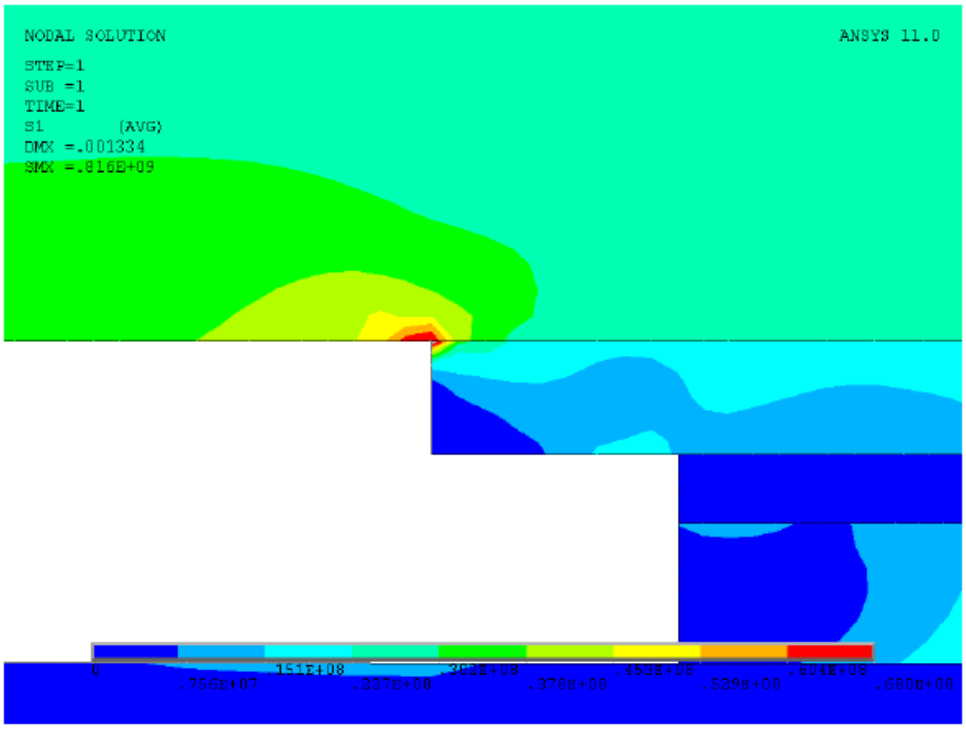

Figure 3.28: Magnified view of critical stress region, double sided case.

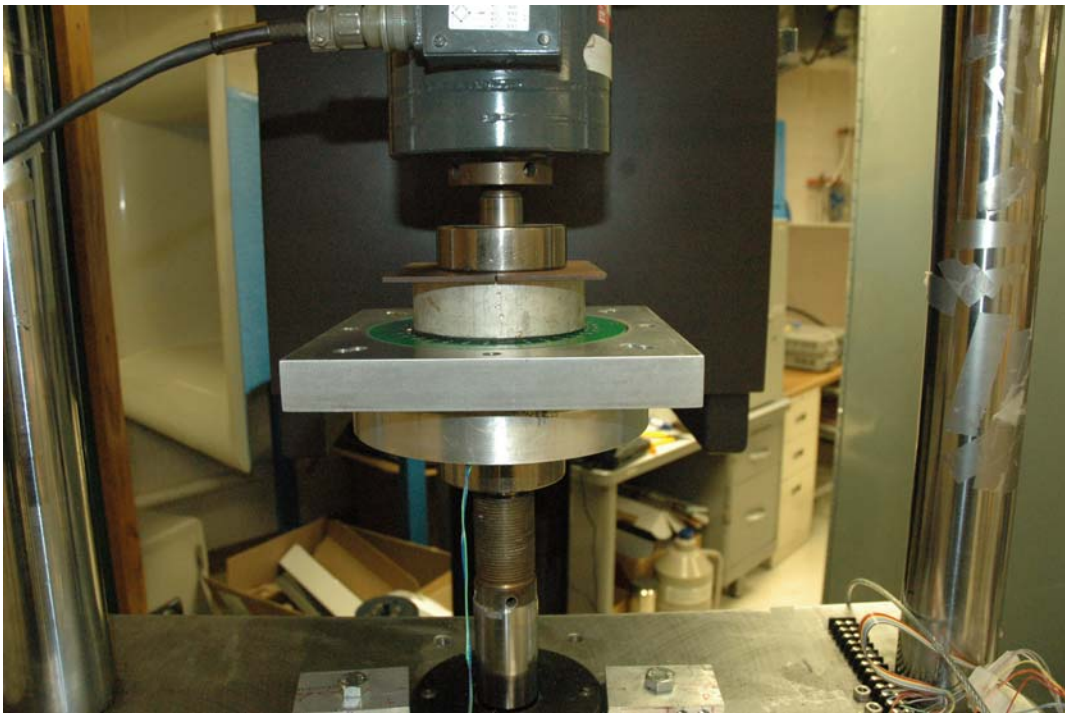

Figure 3.29: MTS bending test setup with round test board.

Displacement Level	Strain at ring location (με)					
	A	B	C	D	E	F
3	583	773	514	638	597	261
6	1228	1296	1179	1682	2024	977
9	1570	1649	1768	2817	4367	2012
12	1818	1910	2261	3953	5881	3309

Table 3.5: PWB strain levels for each displacement level of the MTS ram.

Capacitor Brand	Capacitor Size	Single/Double Sided	Number of Failures	Displacement Level
AVX	1206	Double	11	9
Kemet	1206	Double	1	12
AVX	1206	Single	27	9
Kemet	1206	Single	9	9

Table 3.6: Summary of MTS bend test results, failures on ring E.

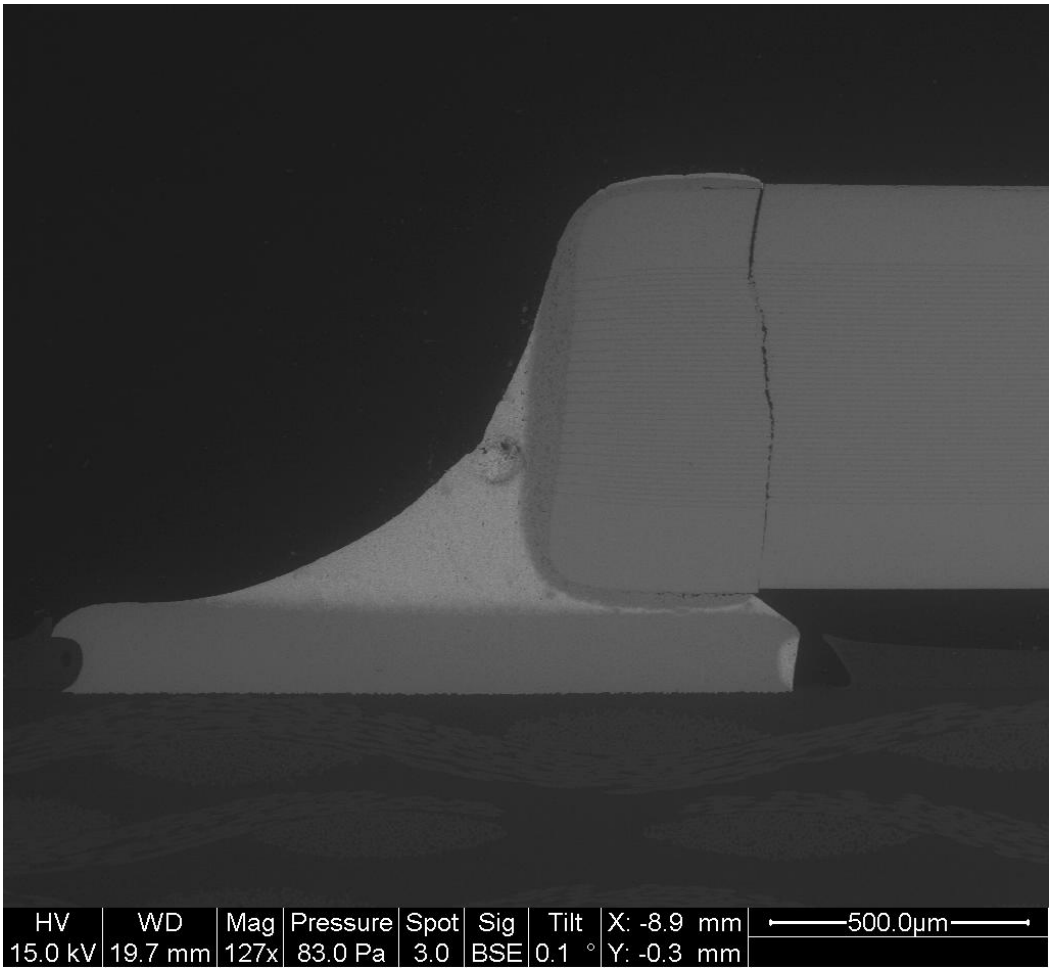

Figure 3.30: Cross section of failed 1206 Kemet MLCC from bend testing.

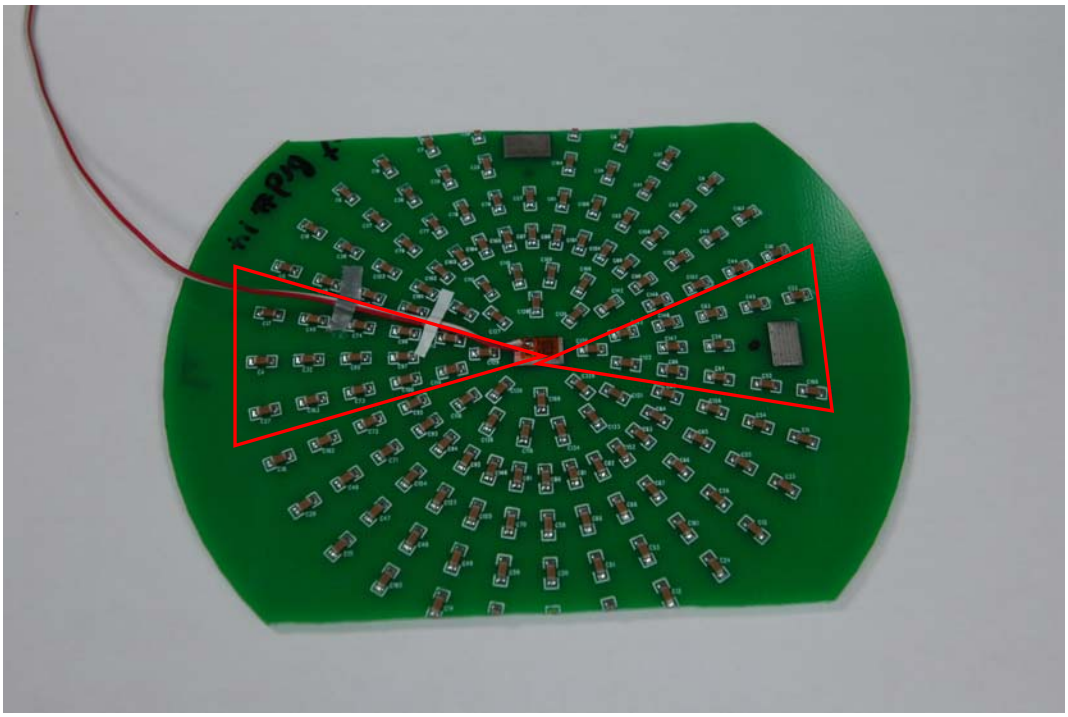

Figure 3.31: Circular board trimmed for use in standard 4-point bend test.

Chapter 4: Degradation of Reliability of Flexible Termination Ceramic Capacitors in High Rate Environments

Introduction

Passive components play a key role in electronic assemblies. Multilayer ceramic capacitor (MLCC) components in particular are prevalent in today's designs, appearing in consumer grade, professional grade, and military products. Many of these electronic assemblies have the potential to experience some degree of high rate loading during their life cycle. Examples of this include the dropping of a portable consumer electronic device by the end user and the launch cycle of smart munitions or near blast loading for military applications. As such, an understanding of the behavior of MLCC devices when subjected to high rate loading is required.

Flexible termination capacitors are the current state of the art in MLCC design. They contain a silver filled epoxy coating underneath the standard tin-nickel end cap metallization. This epoxy layer allows the part to withstand a higher bending load than their standard termination equivalents. Examples in the literature, in addition to preliminary experiments conducted by the authors, confirm that flexible termination capacitors can withstand over twice the PWB strain level that a similar standard termination capacitor can endure [6]. However these examples are all for medium to low strain rate environments, and no studies currently exist to evaluate these parts in a high rate loading environment.

Figure 4.1 shows a cross section of a size 1206 Kemet standard termination MLCC. The component is made up of interlacing metalized layers separated by and encased in a ceramic dielectric. Metal end caps made of a tin-nickel alloy are used as the electrical contacts to the solder pads on the PWB. Figure 4.2 shows a cross section of a size 1206 Syfer flexible termination capacitor. A magnified view of the metal end cap is shown in Figure 4.3. The layer of silver filled epoxy is visible between the ceramic dielectric and the outer portion of the metal end cap. This silver filled epoxy layer is the distinguishing feature of flexible termination capacitors.

This paper will focus on the behavior of flexible termination MLCC devices when subjected to high rate bending. The loading rates will be quantified as strain rates, with the strain values being taken from the surface of the PWB.

The behavior of MLCC devices when subjected to low to medium rate bending (PWB strain rate < 0.1/s) has been well documented in the literature. The failure mechanism resulting from these loading criteria has been observed to be a diagonal crack in the lower portion of the ceramic near the solder attach (see Figure 4.4). This is the only observed failure mechanism identified in the literature for MLCC capacitors subjected to bending loads.

Experimental Setup

Size 1206 and 0603 flexible termination capacitors were selected for this study. Table 4.1 gives an overview of the selected parts.

The test board used for the experiments is shown in Figure 4.5. A round board was selected, with the intention of clamping the edges of the board to produce a

diaphragm-type motion. This configuration was chosen due to the ability to obtain a radial strain distribution on the board, and thus have capacitors subjected to a variety of maximum strains for a single experimental trial. The test board was double sided, and contained 148 parts per side (296 total). Three areas per board side were reserved for strain gage placement. The board diameter was 6 inches. The outer 0.5 inches of the board was clamped during testing, resulting in an active board area of 5 inches. A nominal 1/16 in. board thickness was selected. Standard 60/40 Sn/Pb eutectic solder was used, and the boards were assembled using an automated pick and place machine and a reflow oven at a commercial board assembly shop.

The experimental method used to obtain high rate failures was a drop test. An Impac drop tower was used for these tests. Figure 4.6 shows the fixture that was designed to hold a single round test board for use with the drop tower. This fixture was bolted onto the drop tower table, which was then raised to a predetermined height and released. The table struck the impact surface and was caught on the rebound by the machine, generating a single impact event. The acceleration profile could be tailored by changing the impact media placed between the drop table and the impact surface. A felt pad was used as the impact media for these experiments. Strain measurements were taken from three locations on the test board, along with accelerometer data. A high speed video camera was also used to document the drop event. The camera was time-synced with the data acquisition system so that the board strain could be determined for any given video frame.

A second support condition was utilized, in which the center of the test board was fixed in place with a standoff support. This test condition allowed data to be

collected at a higher PWB strain rate than the condition in which the board was only clamped along its perimeter. Figure 4.7 shows the setup for this support condition.

For each of the test methodologies, the capacitors being evaluated were probe tested prior to and after the test to determine failure. Failure was defined as a 10% decrease in capacitance.

Experimental Results

The peak acceleration for the drop tower experiments was selected as 5kG, with all experimental trials utilizing this acceleration profile. Figure 4.8 shows an example of the selected acceleration profile. Figure 4.9 shows an example of the PWB strain response, as measured from a strain gage located at the outer edge of the board for the simple diaphragm support condition. Table 4.2 shows the PWB strain rates calculated from each of the high rate experimental setups outlined in the paper. The resulting PWB strain rate for this test condition was calculated to be ≈ 1/s. The PWB strain rate for the fixed center support condition was calculated to be ≈ 5/s. Figure 4.10 shows an example of the PWB strain response, as measured from a strain gage located at the outer edge of the board for the fixed center support condition. This strain plot shows the same amount of time as Figure 4.9 for the simple diaphragm support condition. However, the number of strain cycles achieved in this time is higher, resulting in a higher strain rate for the fixed center support case. This higher strain rate is a result of the structure being stiffened by the inclusion of the center support.

Upon reviewing the high speed videos of the drop events, it was determined that component failure occurred within the first 3 board oscillations in all cases of failure. These first few cycles of board motion represent the transient response, which damped out after 4-5 full cycles of board oscillation. Thus, the possible fatigue influence due to the steady state damped sinusoidal response of the test board after impact can be negated.

A set of experiments was conducted to determine the strain level experienced by each component mounted on the PWB based on its location. A radius on the PWB was lightly milled to create a smooth surface. Six strain gages were then mounted along the radius, with one gage representing each of the rings of components mounted on the PWB. Dropping these boards allowed the strain response at each component location to be determined. This test was conducted for both the simple diaphragm and fixed center support conditions. Two trials were run for each support condition, with the averaged results summarized in Table 4.3. The board motion was shown to be radially symmetric in experimental trials by comparing the results of the gages that were placed 90 degrees apart at the edge of the PWB. The two gages showed identical response, verifying the motion to be radially symmetrical and thus a true diaphragm type response.

Table 4.4 gives a summary of the drop tower results. Both size 0603 and 1206 show a significant decrease in performance when PWB strain rate is increased. Size 1206 capacitors show the most dramatic decrease, with 1.4% failed (4 out of 296 components) at a PWB strain rate of 1/s and 96.6% failed (286 out of 296 components) at a PWB strain rate of 5/s. The performance of size 0603 parts was

roughly equivalent to that of the size 1206 parts when PWB strain rate ≈ 1/s, with both part sizes approaching a 100% survival rate. However, size 0603 parts clearly outperformed size 1206 parts for the highest PWB strain rate of 5/s.

These failures occurred at strain levels well below those corresponding to failure in medium to low rate environments. Examples in the literature, in addition to preliminary testing conducted by the authors, indicate that size 1206 flexible termination capacitors can survive PWB strains in excess of 10,000 με in low to medium rate bending. Table 4.3 gives the strain values experienced by capacitors at each radial position, and they are more than an order of magnitude lower than the documented medium to low rate value of over 10,000 με for failure. This disparity illustrates the influence of loading rate on the performance of flexible termination capacitors.

A related study pending publication by the authors investigated the reliability of standard termination capacitors in high strain rate environments. This study subjected standard termination capacitors to the same drop testing methods outlined in this paper. This study did not record a comparable decrease in reliability for standard termination parts as PWB strain rate was increased. Table 4.5 outlines the test results from the related study.

Both of the size 1206 standard termination components had a significant amount of failures at the lower PWB strain rate of 1/s. The percentage failed for size 1206 Kemet devices roughly doubled when the PWB strain rate was increased to 5/s. However, the size 1206 AVX components showed a small improvement for the same increase in PWB strain rate. These results for 1206 standard termination components

are much different than those for their flexible termination equivalents, which saw a percentage failure increase from 1.4% (4 out of 296 components) at 1/s to 96.6% (286 out of 296 components) at 5/s. The 96.6% failed at a PWB strain rate of 5/s for the flexible termination parts contrasts with 68.2% (202 out of 296 components) and 31.1% (92 out of 296 components) failed for Kemet and AVX parts at the same PWB strain rate.

The size 0603 standard termination components performed consistently well at PWB strain rates of 1/s and 5/s, with a roughly 100% survival rate in both tests. However, the flexible termination equivalent evaluated in this paper jumped from 0.7% failed (2 out of 296 components) to 43.6% (129 out of 296 components) failed with an equivalent increase in PWB strain rate.

When the two data sets are compared as such, it is evident that standard termination capacitors outperform flexible termination capacitors in the high strain rate environment. The transition region where the performance of flexible termination capacitors decreases is between the PWB strain rates of 1/s and 5/s. This result is surprising considering the well documented superior performance of flexible termination capacitors in the low to medium strain rate regime.

Failure Analysis

Failure analysis was conducted on failed capacitors from both test conditions. A new failure mechanism was documented for both 1206 and 0603 flexible termination capacitors as a result of this study. This new failure mechanism involves

the silver filled epoxy portion of the metallization end cap delaminating from the tin-nickel portion.

Figure 4.11 shows an example of the new failure mechanism for size 1206 flexible termination parts. Shown is the remaining area on the board where the capacitor was located. For size 1206 parts, the delamination occurred in both end caps and the capacitor separated from the test board with no cracking in the ceramic. Figures 4.12 and 4.13 show magnified views of both solder pads. Figure 4.14 shows the failed capacitor body that detached from the test board during the test. Figure 4.15 shows a magnified view of the end cap portion of this failed capacitor. Figure 4.16 shows a cross section of a size 1206 part that detached from the PWB during the test. The cross section was created by polishing up into the surface of the part that would have been closest to the PWB; basically looking underneath the part. Figure 4.17 shows a magnified view of the bottom right portion of the part shown in Figure 4.16. The delamination between the silver filled epoxy and the tin-nickel plating is clearly visible. This delamination was observed to occur in the same manner for size 0603 parts. Failure only occurred in 1206 parts when the capacitor completely detached from the PWB. When the part remained attached to the PWB, the part was found to survive the test with no discernable damage.

Cracks in the PWB that initiated at the solder pads were observed for size 1206 parts, as shown in Figure 4.18. These cracks were seen to be more prevalent at the solder pads of parts that remained attached to the PWB and thus survived the test. Cross sections were taken to determine the extent of these cracks in the PWB. The cracks were determined to mainly affect the solder mask layer of the PWB, and did

not continue very far through the thickness of the PWB into the FR4 region. Figure 4.19 shows an example of a cross sectioned PWB to give an idea of the board makeup. Figure 4.20 shows a crack in the PWB. As Figure 4.20 illustrates, the cracks extended through the solder mask portion of the PWB and terminated in the first layer of glass fibers in the FR4.

Figure 4.21 shows an example of the new failure mechanism for size 0603 flexible termination parts. For size 0603 parts, the delamination occurred in only one of the part end caps. The opposite end of the part showed cracking through the lower portion of the ceramic near the solder fillet, with the crack following a roughly 45-degree path to the end cap metallization. A magnified view of the end cap that separated due to cracking in the ceramic is shown in Figure 4.22. A magnified view of the end cap that separated due to delamination is shown in Figure 4.23. Figure 4.24 shows a failed size 0603 capacitor that detached from the board during testing. Figure 4.25 shows a magnified view of the capacitor end cap that failed due to delamination.

Failure also occurred in size 0603 parts due to ceramic body cracking alone. Figure 4.26 shows an example of a crack in the ceramic portion of a size 0603 part that resulted in part failure. This vertical crack path was consistent with the vertical flex cracks seen in standard termination MLCCs evaluated in the previously mentioned related study by the authors, the experimental results from which are summarized in Table 4.5. Table 4.6 gives the number of occurrences of each of the observed failure mechanisms for size 0603 flexible termination parts for each of the board support conditions. The vertical flex crack failure mechanism was the

predominant cause of failure, with 113 out of 129 failures (88% of failures) being attributed to it. The cracking of the solder mask layer observed for size 1206 parts was not seen for size 0603 parts.

For both part types, increasing the PWB strain rate from 1/s to 5/s brought about a large decrease in the survivability of the component. Thus the discovered delamination effect appears to be extremely strain rate dependant.

A hypothesis was formulated to explain the delamination effect and its correlation with PWB strain rate. In medium to low rate bending, the silver filled epoxy aids in mitigating the stress in the component and thus improves the component's reliability and allows it to withstand a higher bending load. This is due to its elastic modulus value being lower than that of solder (silver filled epoxy E = 5 GPs versus standard eutectic 63/37 Sn/Pb solder E = 32 GPa). However, increasing the strain rate causes the silver filled epoxy to behave less compliantly due to strain rate hardening. This more rigid epoxy does not mitigate as much stress in the component, and the adhesion forces between the tin-nickel layer and the silver filled epoxy layer are not high enough to withstand this increased stress load. Thus, the component delaminates at the tin-nickel/silver filled epoxy interface.

An alternative hypothesis to explain the delamination effect and its correlation with PWB strain rate is that the adhesion strength between the silver filled epoxy and the tin-nickel is itself dependant on strain rate. Thus, increasing the strain rate would result in the bond delaminating at a lower stress value.

The phenomenon could also be attributed to a combination of the two hypotheses above. In this scenario, the epoxy behaving in a more rigid manner due to

strain rate hardening would not mitigate as much stress in the component, while the necessary stress to cause delamination at the tin-nickel/silver filled epoxy interface would decrease due to the high strain rate. The part would fail first due to delamination, since the critical stress threshold to cause cracking in the ceramic would not be reached.

Conclusion

Flexible termination capacitors have been shown to be unreliable in the high strain rate regime (PWB strain rate $\geq$ 5/s). This is due to a newly discovered failure mechanism that occurs in high rate loading at much lower PWB strain values than expected. This new failure mechanism involves a delamination between the silver filled epoxy and the tin-nickel layers in the component end cap.

When compared to standard termination capacitors subjected to the same PWB strain rate of 5/s, flexible termination capacitors have been shown to perform significantly worse. This result contrasts sharply with the markedly superior performance of flexible termination parts in low to medium rate environments. As a result, designers planning to utilize the state of the art flexible termination capacitors will have to consider the loading rate regime of their design carefully before selecting these parts over their standard termination predecessors.

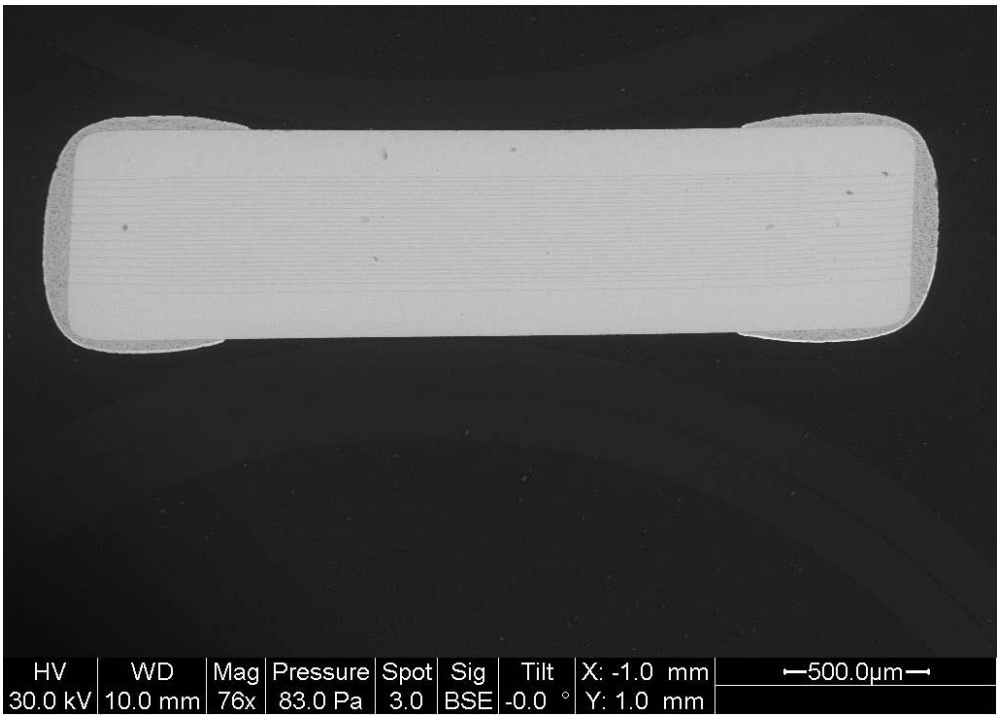

Figure 4.1: Cross section of standard termination 1206 Kemet capacitor.

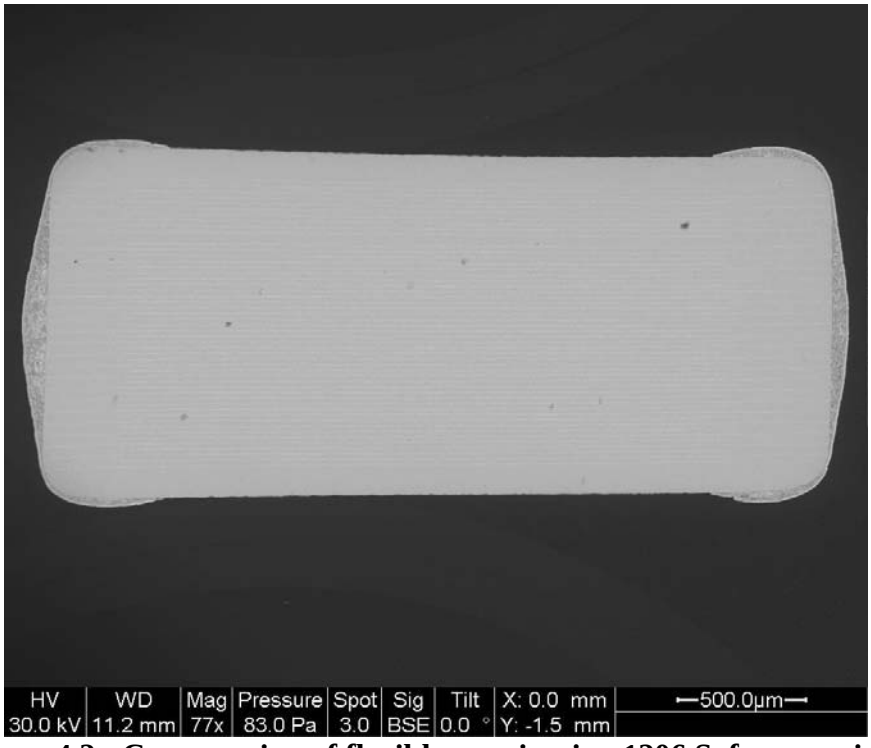

Figure 4.2: Cross section of flexible termination 1206 Syfer capacitor.

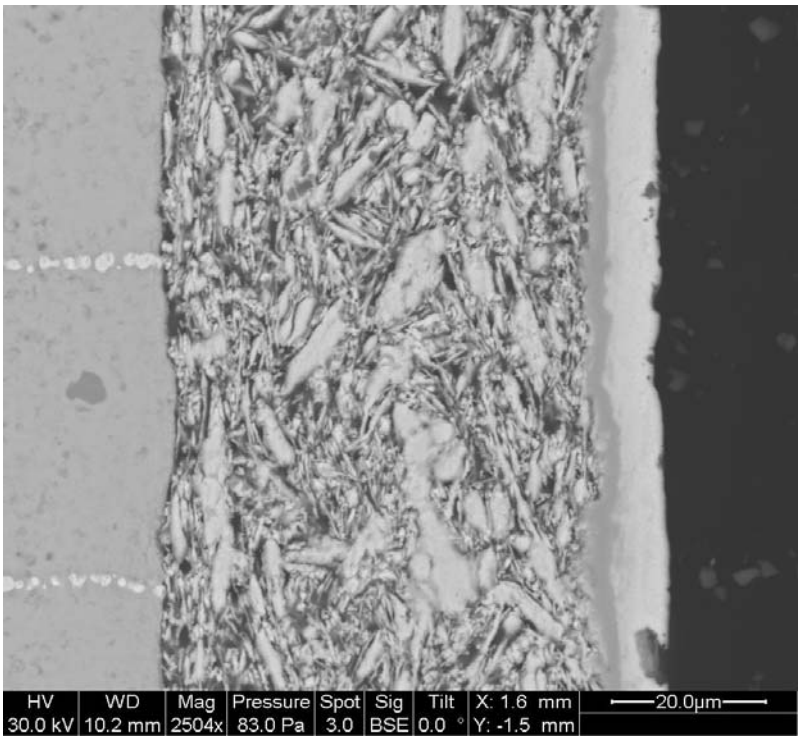

Figure 4.3: Magnified view of flexible termination capacitor end cap.

Figure 4.4: Cross section of 1206 Kemet MLCC, with visible flex cracking.

Manufacturer	Size	Dielectric	Capacitance	Voltage	Tolerance	Termination
Syfer	1206	X7R	0.1µF	50V	±10%	flexible
Syfer	0603	X7R	0.0047µF	200V	±10%	flexible

Table 4.1: Overview of capacitors selected for evaluation.

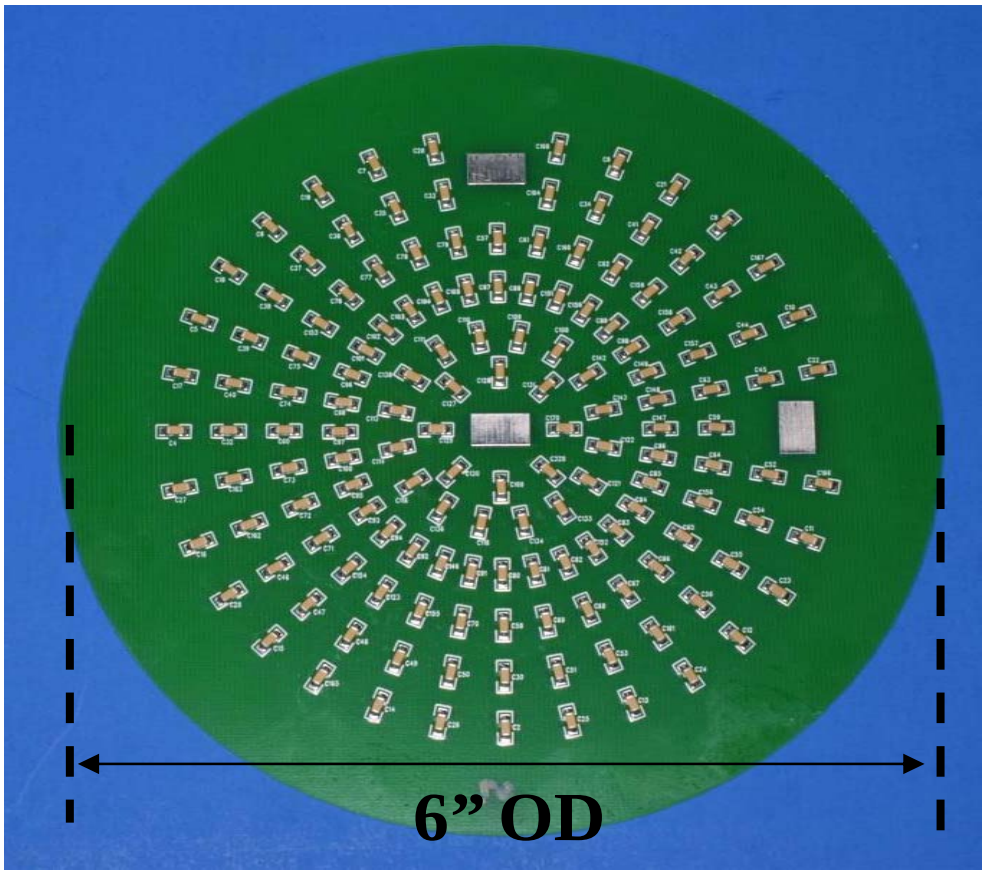

Figure 4.5: Test board for high rate testing (size 1206 board shown).

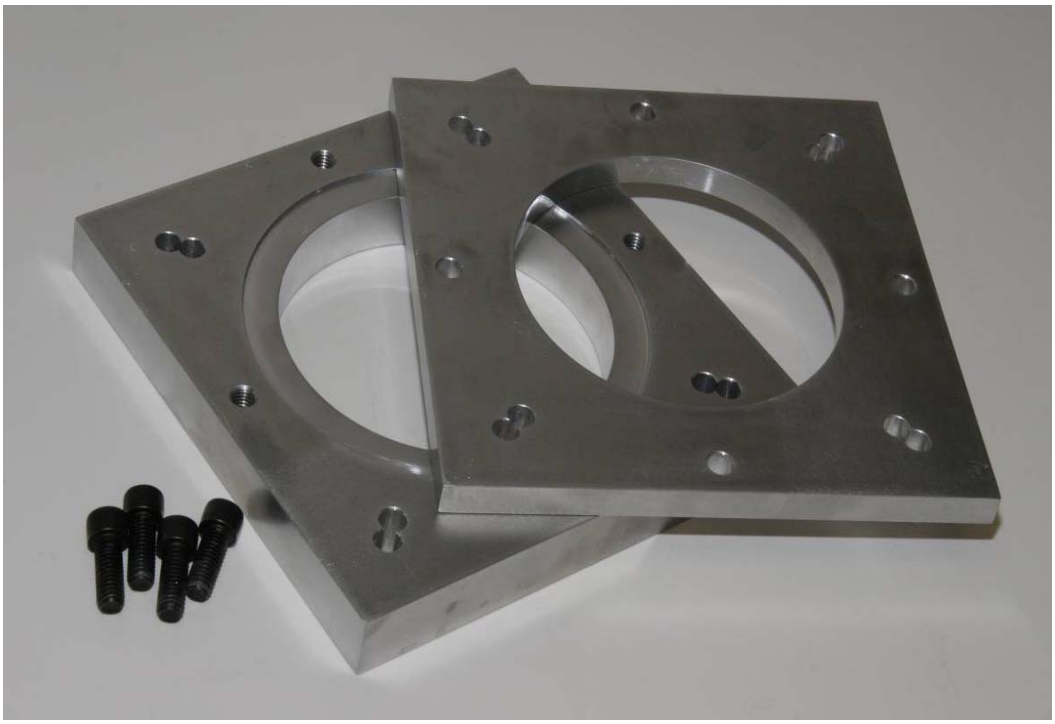

Figure 4.6: Drop tower test fixture.

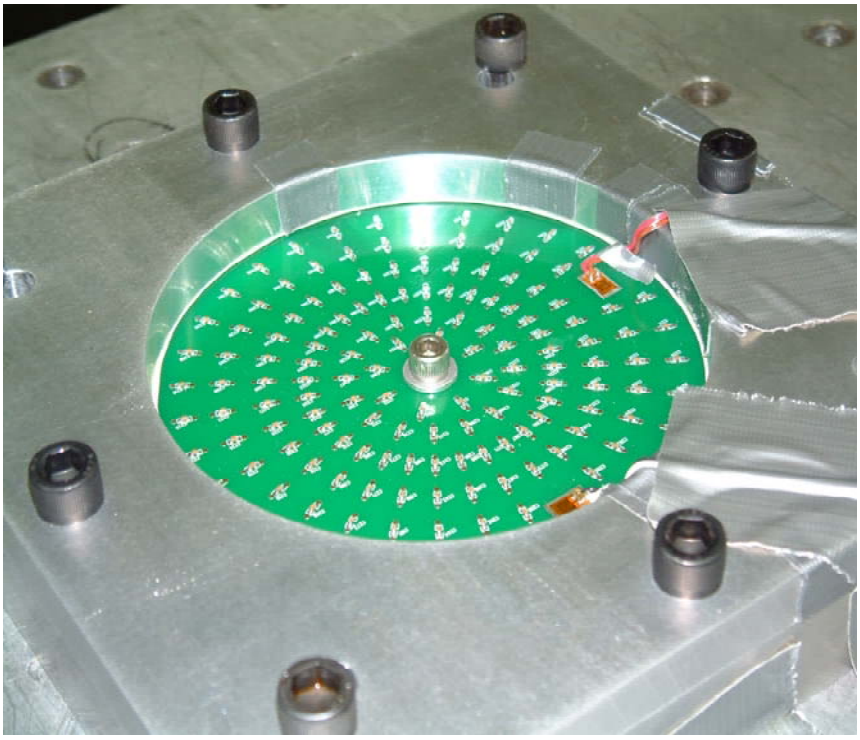

Figure 4.7: Drop support condition with fixed center.

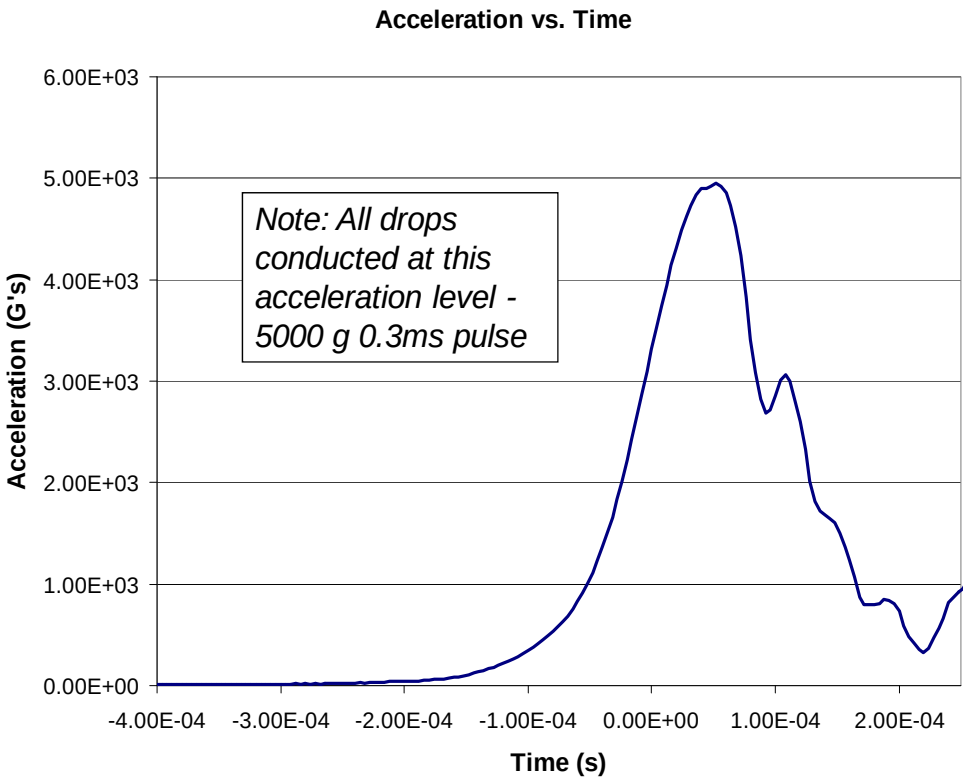

Figure 4.8: Acceleration profile for drop tower tests.

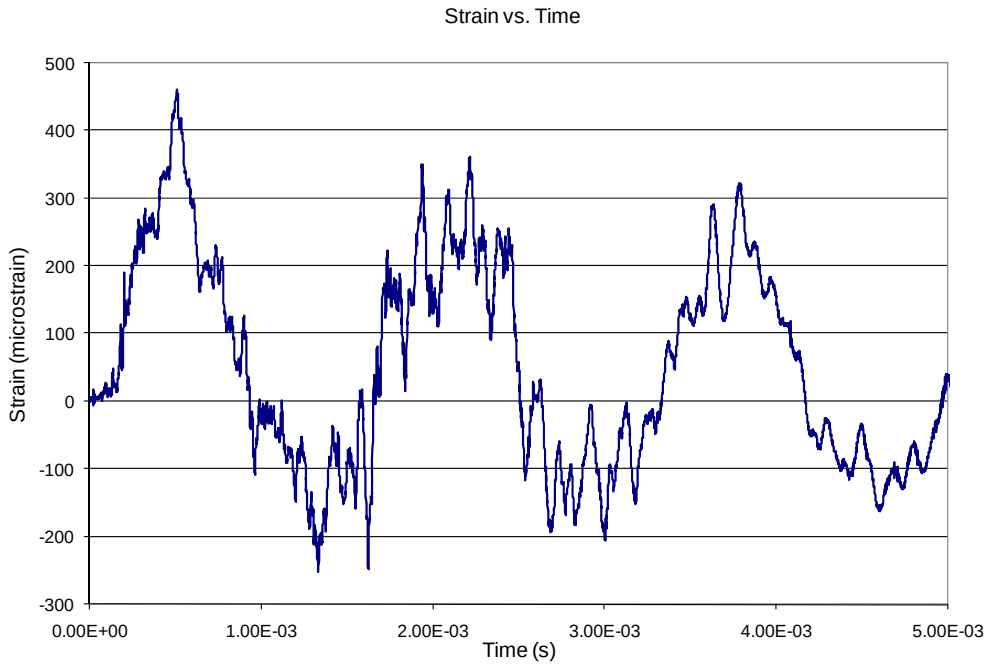

Figure 4.9: Strain response at board edge for full diaphragm condition.

Test Description	Strain Rate
Drop tower test, full diaphragm condition	0.878/s (≈ 1/s)
Drop tower test, board fixed in center	5.93/s (≈ 5/s)

Table 4.2: PWB Strain rates for each support condition.

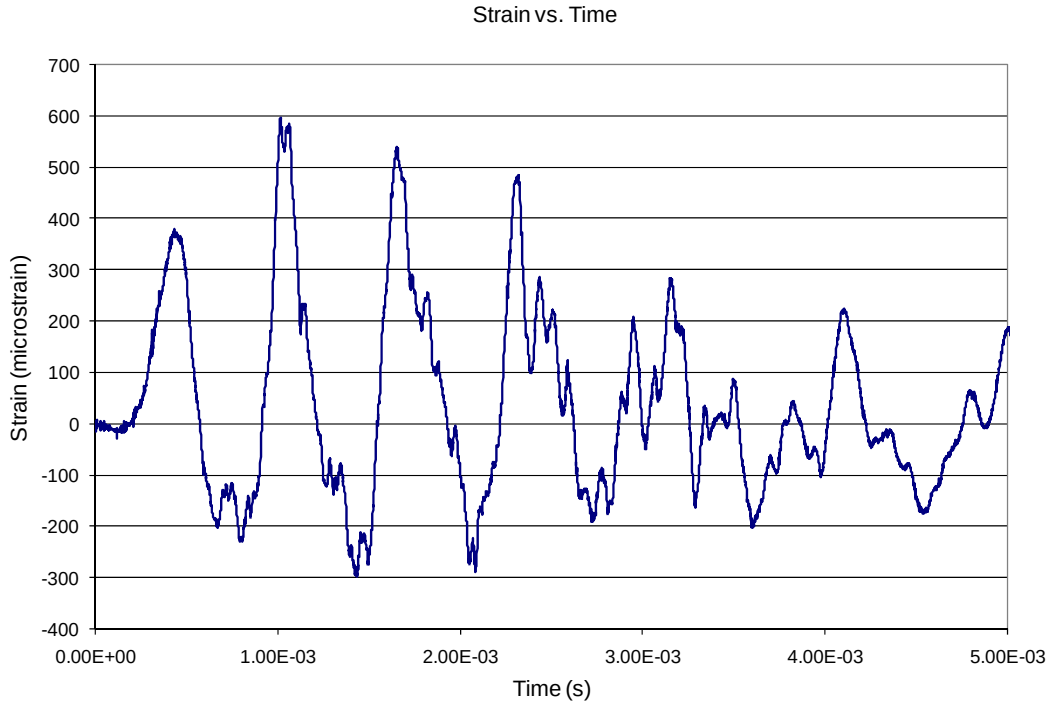

Figure 4.10: Strain response at board edge for fixed center condition.

Ring ID	Radius (mm)	Free Center Strain (με)	Fixed Center Strain (με)
A	11	450	716
B	18	335	900
C	27	407	1006
D	37	260	737
E	46	354	509
F	56	440	612

Table 4.3: Maximum strain values at each ring position on test board.

Size	Manufacturer	Center Support?	# Failed	% Failed
0603	Syfer	No	2 / 296	0.7
1206	Syfer	No	4 / 296	1.4
0603	Syfer	Yes	129 / 296	43.6
1206	Syfer	Yes	286 / 296	96.6

Table 4.4: Summary of results for flexible termination MLCC drop testing.

Size	Manufacturer	Center Support?	# Failed	% Failed
0402	Kemet	No	2 / 296	0.7
0603	Kemet	No	2 / 296	0.7
0603	Kemet	No	0 / 296	0.0
1206	Kemet	No	103 / 296	34.8
1206	AVX	No	121 / 296	40.9
0402	Kemet	Yes	6 / 296	2.0
0603	Kemet	Yes	0 / 296	0.0
1206	Kemet	Yes	202 / 296	68.2
1206	AVX	Yes	92 / 296	31.1

Table 4.5: Prior results from MLCC standard termination drop testing.

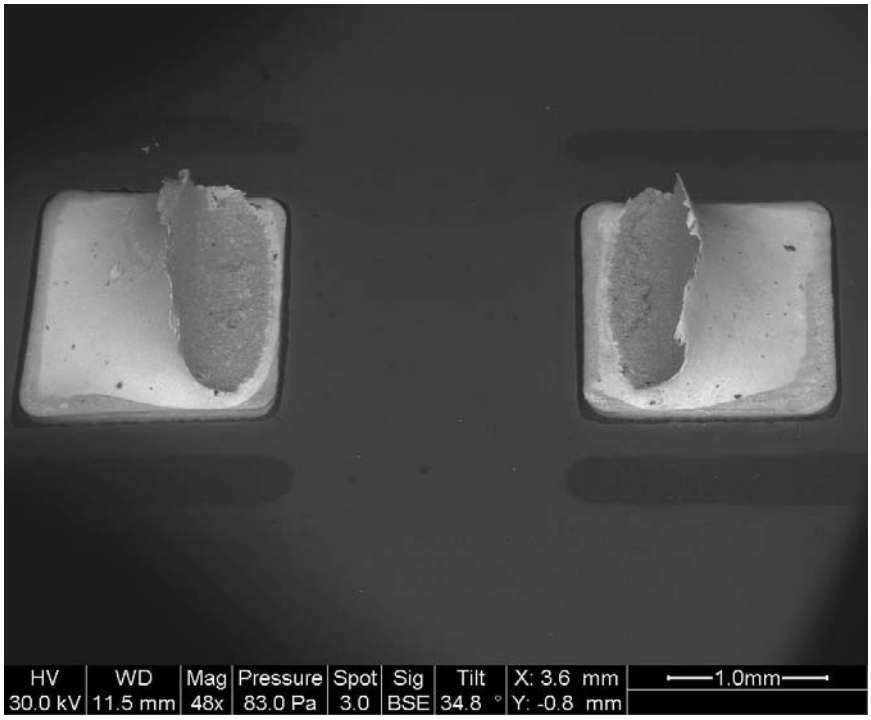

Figure 4.11: Failure of 1206 flex termination MLCC, overview.

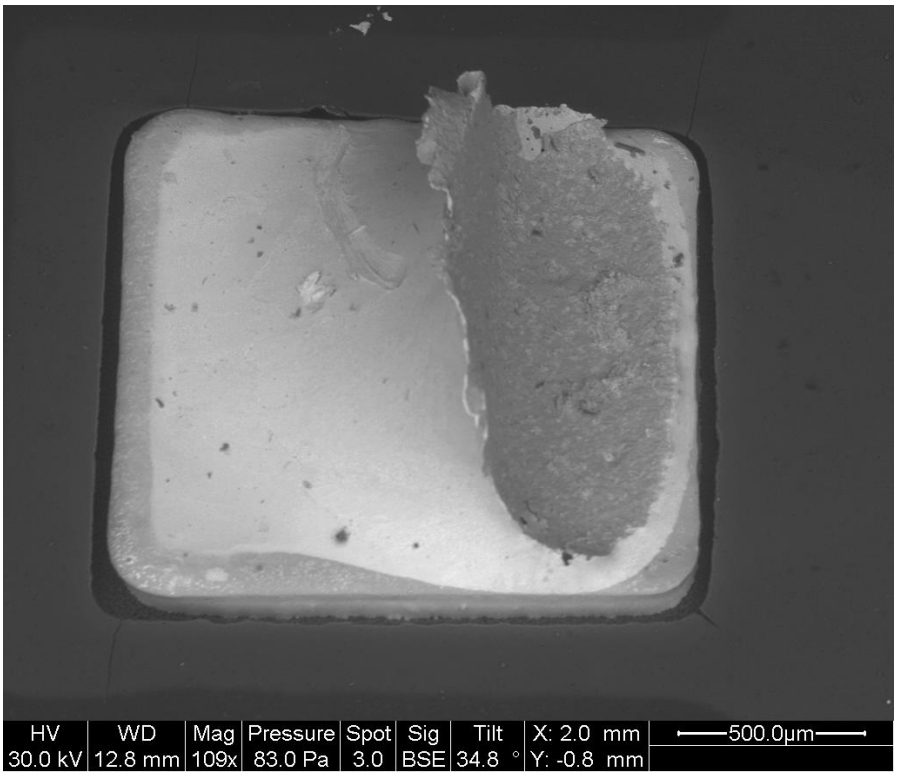

Figure 4.12: Failure of 1206 flex termination MLCC, left pad.

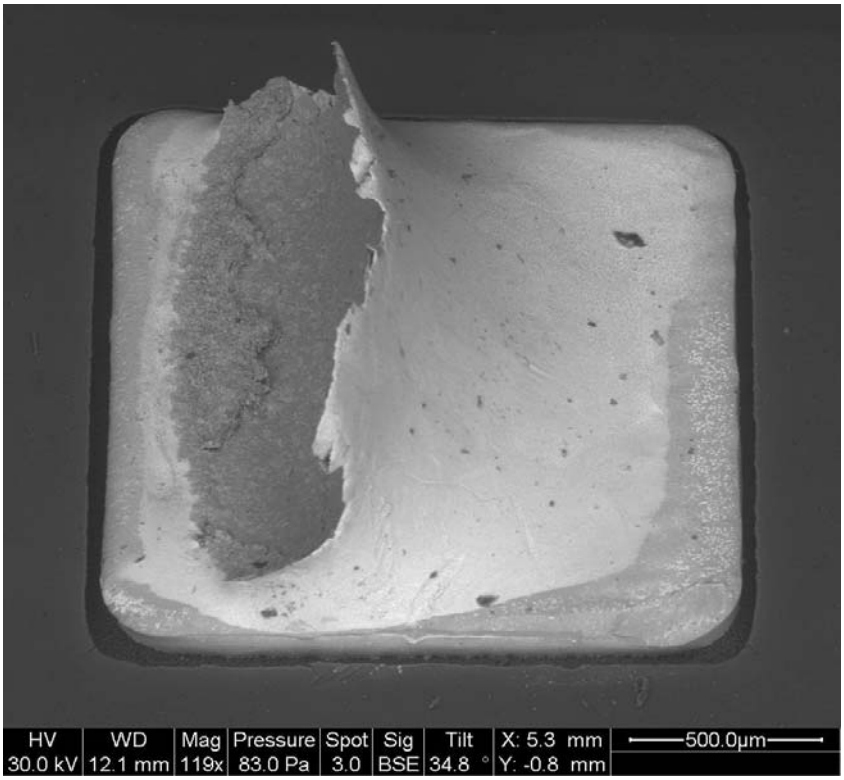

Figure 4.13: Failure of 1206 flex termination MLCC, right pad.

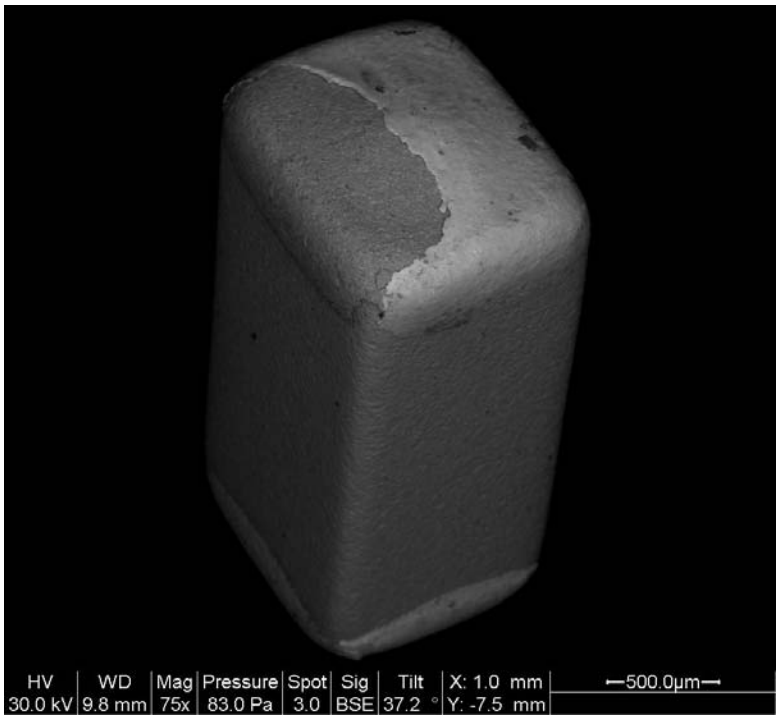

Figure 4.14: Failed 1206 flex termination MLCC, detached during test.

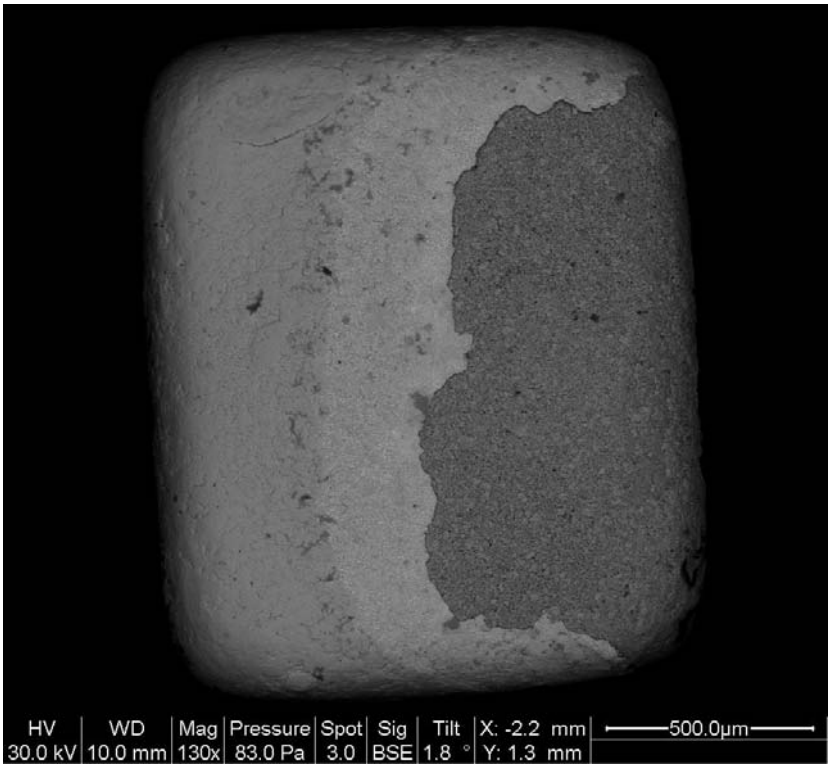

Figure 4.15: Magnified view of end cap, failed 1206 flex termination MLCC.

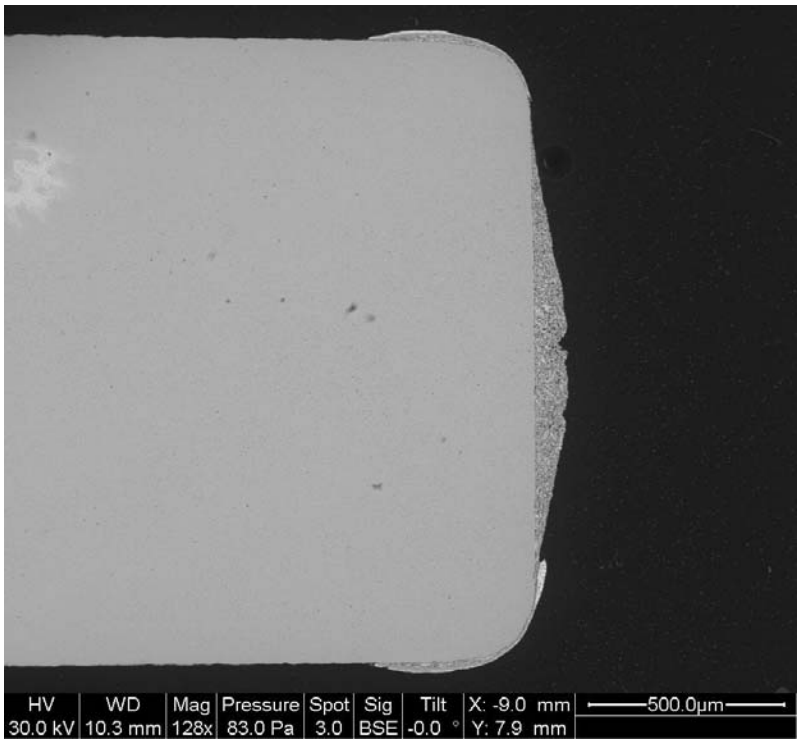

Figure 4.16: Cross section of detached 1206 flex termination MLCC.

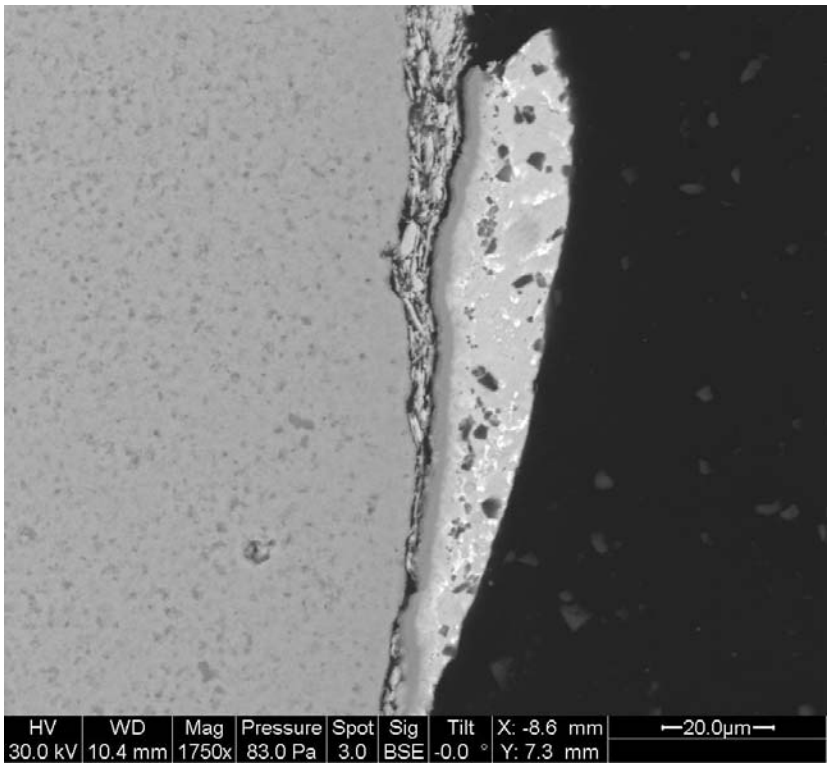

Figure 4.17: Magnified view of detached MLCC showing delamination.

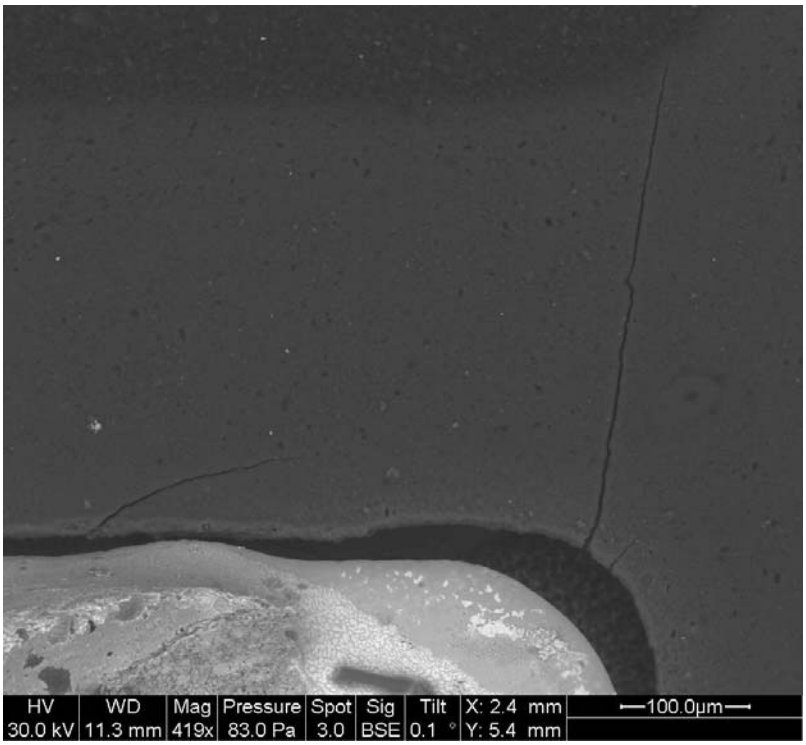

Figure 4.18: Board cracking at solder pad, 1206 flex termination MLCC.

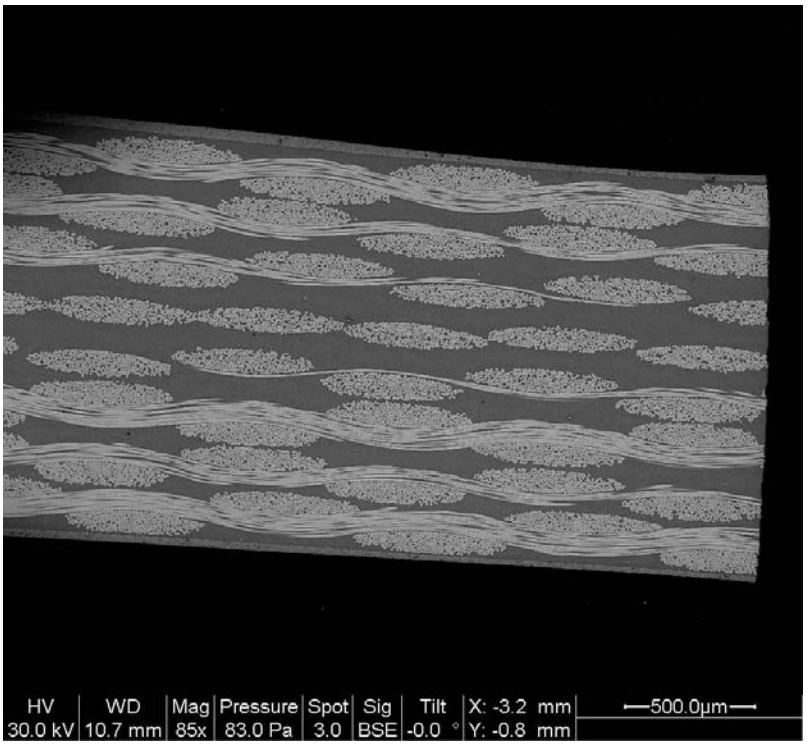

Figure 4.19: Cross section of FR4 test board.

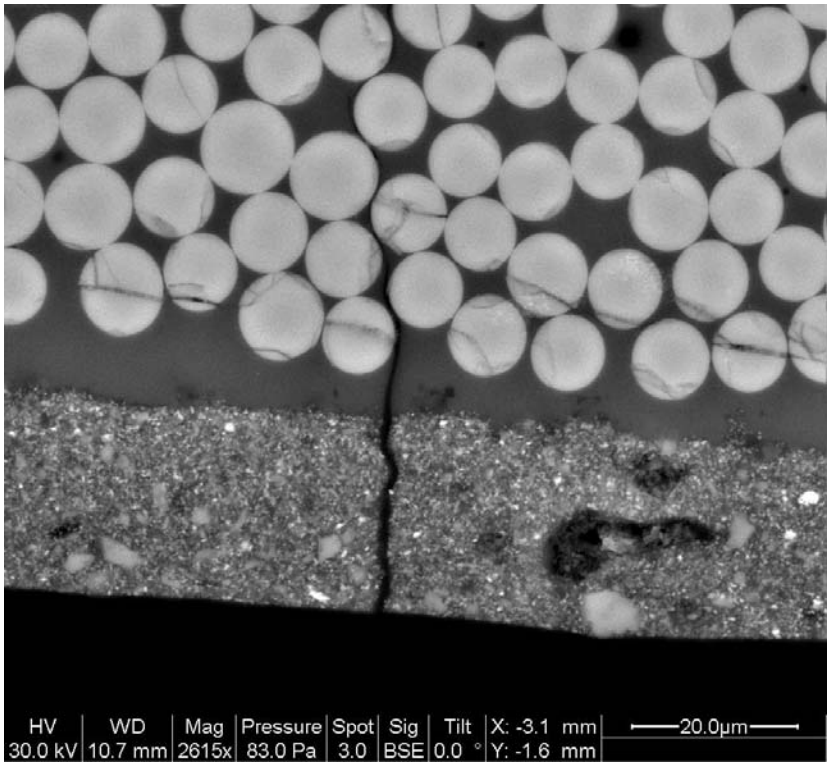

Figure 4.20: Crack through solder mask layer of test board

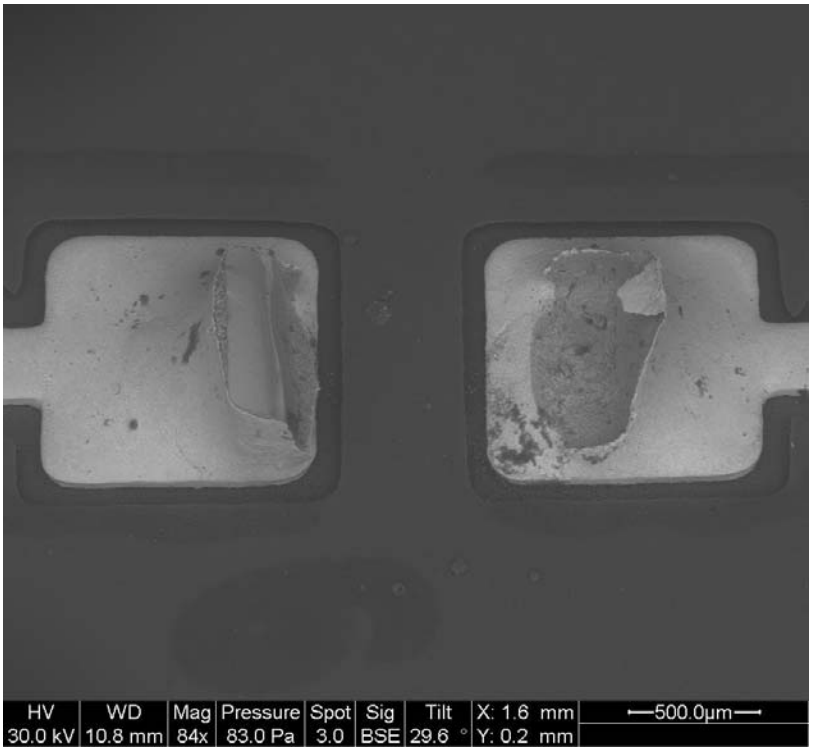

Figure 4.21: Failure of 0603 flex termination MLCC, overview.

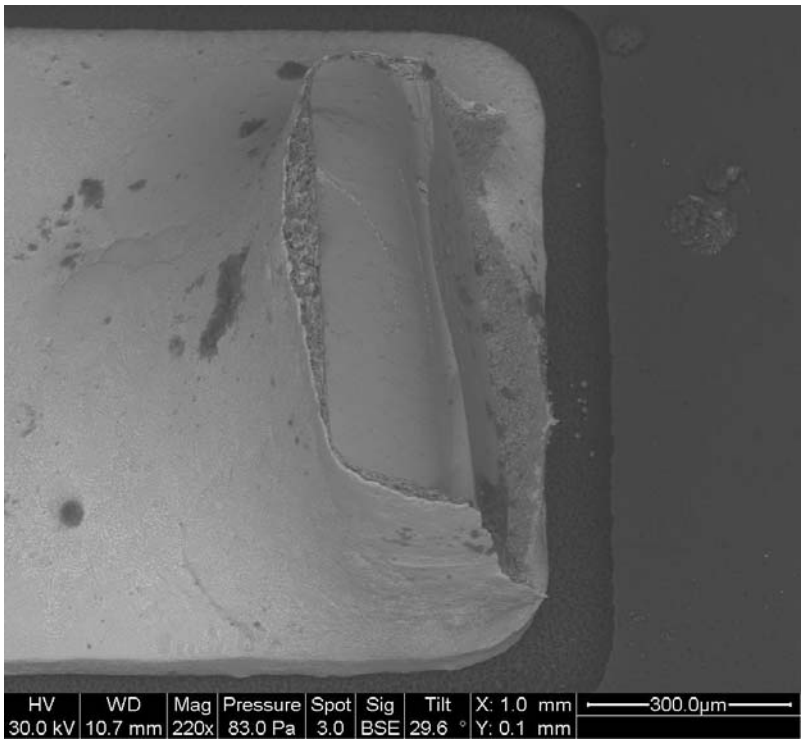

Figure 4.22: Failure of 0603 flex termination MLCC, left pad.

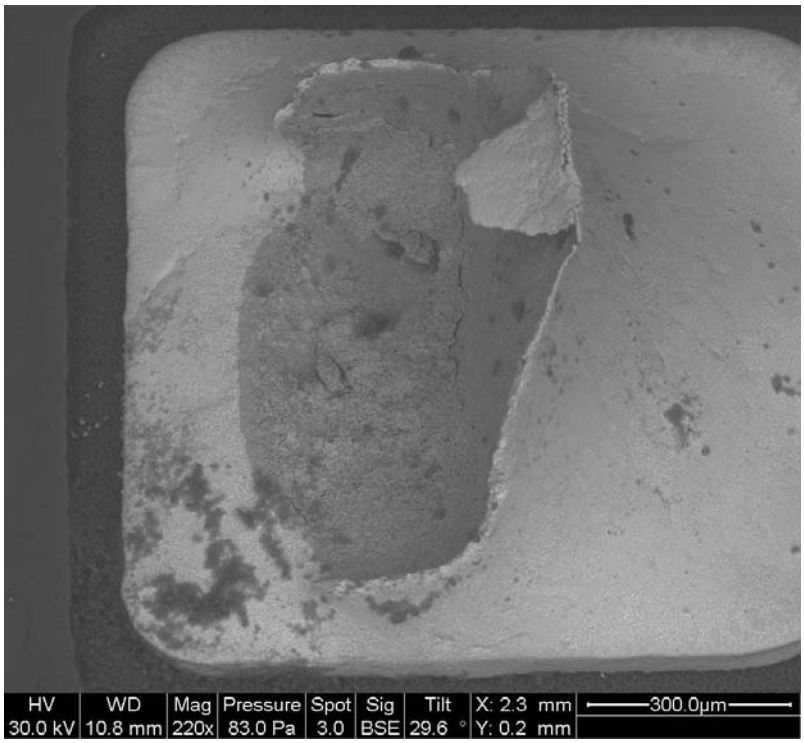

Figure 4.23: Failure of 0603 flex termination MLCC, right pad.

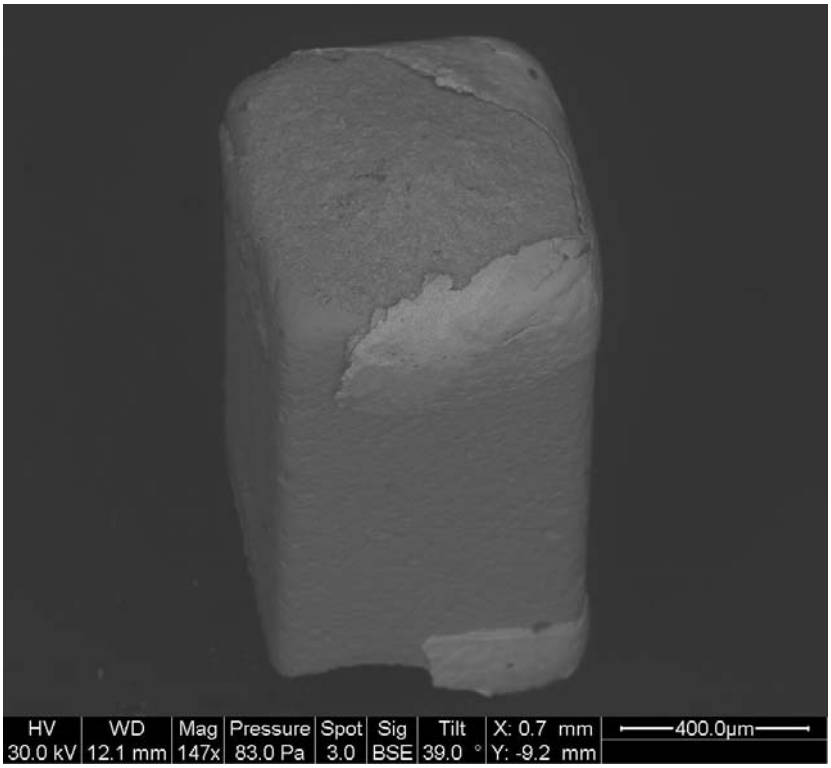

Figure 4.24: Failed 0603 flex termination MLCC, detached during test.

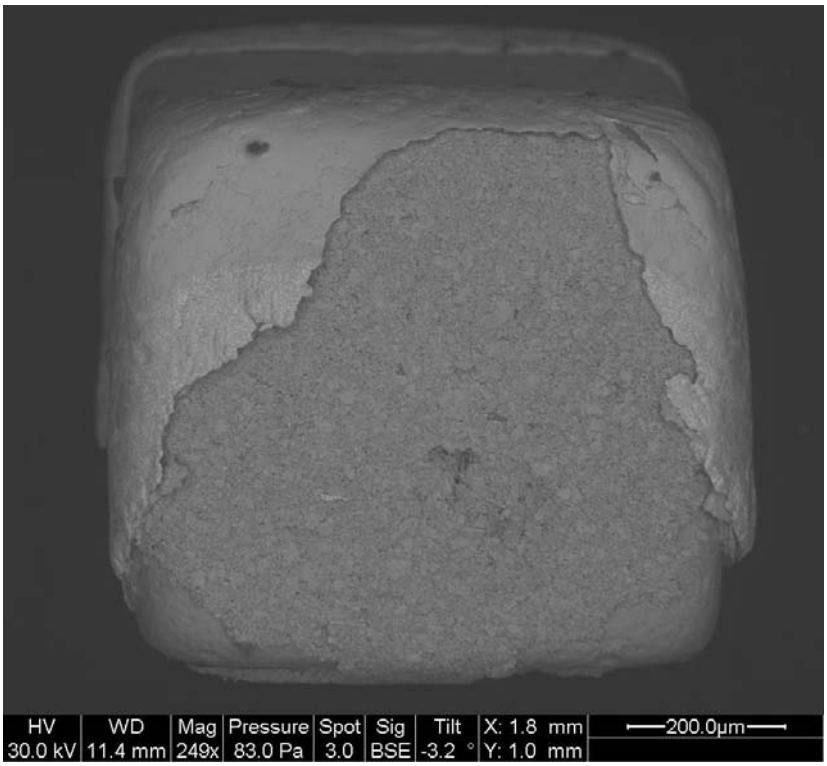

Figure 4.25: Magnified view of end cap, failed 0603 flex termination MLCC.

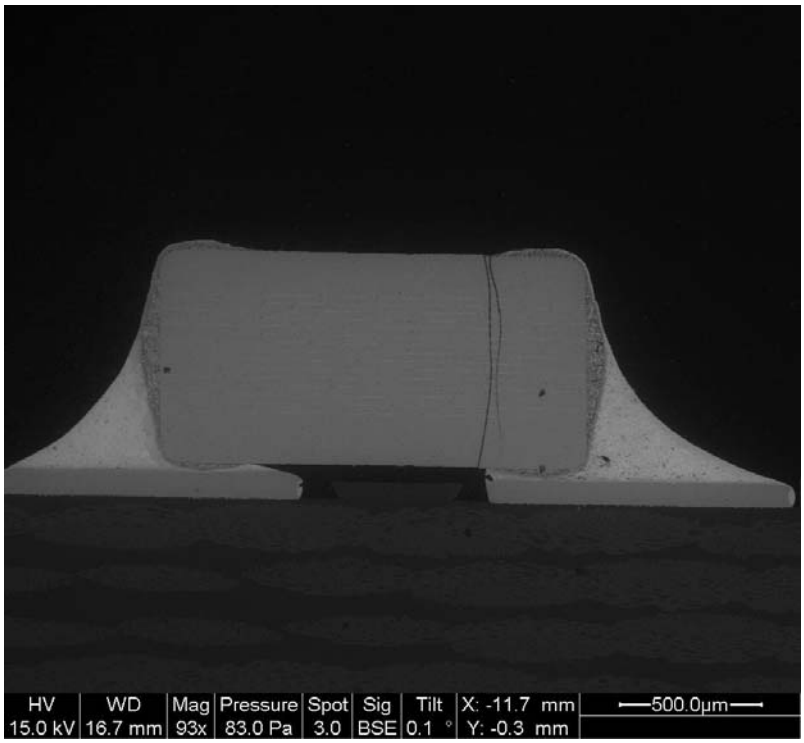

Figure 4.26: Vertical crack through ceramic, 0603 flex termination MLCC.

Support Condition	Failures by Delamination	Failures by Vertical Flex Cracking
Free Center (Strain rate ≈ 1/s)	0	2
Fixed Center (Strain rate ≈ 5/s)	16	113

Table 4.6: Frequency of each failure mechanism for size 0603 flex caps.

Chapter 5: Discovery of Master Failure Curve for BGA Devices Subjected to Bending Loads

Introduction

Ball grid array (BGA) components are currently a popular type of electronic package, due to their ability to accommodate high I/O counts and rugged mechanical performance. These components have the potential to be subjected to bending loads during their life cycle. These loads can be of large amplitude, such as from the dropping of a personal electronic device, or small amplitude, such as from the vibration environment on a vehicle chassis. To evaluate the feasibility of incorporating a BGA device into a given design, a failure curve must be generated to describe the ruggedness of the device when subjected to board flexing.

In this paper, a series of experiments are presented that subject BGA devices mounted to PWBs to bending loads. The resulting data is then compared to an independently generated data set which evaluated different size BGA components, used a different test methodology, and generated different failure mechanisms. This data set is discovered to be in close agreement with the data obtained via the experiments described in this paper, facilitating the ability to create a master curve to describe the reliability of BGA devices subjected to bending loads.

Experimental Setup

BGA components specifically designed for use in mechanical testing were selected to perform the series of experiments outlined in this paper. The components were 256 I/O full array devices manufactured by Top Line. They were internally daisy chained to allow for simplified continuity monitoring during testing. These components contain a dummy silicon die, which is 5mm x 5mm. The device pitch size was 1.0 mm. Figure 5.1 shows an x-ray image of the BGA component being evaluated. This image was taken from a BGA device mounted on a PWB, and PWB traces and microvias are also visible on the image. The die is visible as the darkened portion of the image in the center of the device.

Sample coupons were designed and manufactured, with each coupon containing two BGA devices. Figure 5.2 shows a schematic of the test coupon. Figure 5.3 shows a close up of the center portion of the test board containing the BGA devices. The board was designed so that the continuity of each BGA device could be monitored as a whole during testing. Probe pads were incorporated to facilitate failure site location after the test was complete. These pads are visible around the periphery of each of the BGA packages shown in Figure 5.3. Three strain gage sites were designated on the test board, visible between the two components in Figure 5.3. Figure 5.4 shows a side view of the BGA devices mounted on the test board. The test coupons measure 20 x 5.5 cm. and were 1/16 in. thick.

A four point bend fixture was designed to be used with an MTS servo-hydraulic material testing machine. The test was designed to load the components in tension only, with a full test cycle being measured from zero to tension and back to

zero. Strain measurements were taken from the board surface during the test, and part continuity measurements were time-synced to the strain data so that the exact strain value could be determined when continuity was disrupted. To achieve continuity monitoring, the resistance of the network was continuously monitored by the computerized data acquisition system. When a fracture initiated in the BGA, the resistance of the network would increase due to the decreased contact surface. Once the network resistance increased by 1000 Ω, the part was determined to be failed. Initially, these increases in network resistance followed the board curvature, as the fracture would open when board curvature was increased. When curvature was decreased the resistance would return to a normal level. This phenomenon illustrates the importance of conducting real time continuity monitoring, since probe testing upon completion of an experimental trial would fail to identify a failed part.

These experiments were intended to generate failure data in the ultra-low to low cycle fatigue range. Thus, the loading was performed at very high PWB strain values, with the peak PWB strain being as high as 12,000 microstrain in some trials. The loading was done rapidly, at a PWB strain rate of 0.1/s. PWB strain was used as the failure parameter for this study.

Experimental Results and Discussion

Table 5.1 shows the resulting experimental data. Figure 5.5 shows a plot of the failure data generated in these experiments. The low cycle fatigue failure regime is generally defined as the regime in which failure occurs at less than 10^4 cycles of stress [35]. The cycles to failure in this data set range from 2 to 287, which is well

inside the low cycle fatigue failure regime. When a power law linear regression fit is performed on the data, the resulting fatigue ductility exponent is -0.29. This value is close to the classic Coffin-Manson low cycle fatigue ductility exponent value of approximately -0.5 for most metals [35]. It should be noted that the data contained in Figure 5.5 was collected at PWB strain rates varying from 0.1/s to 0.01/s, and the close correlation of the data set seems to illustrate the lack of effect of strain rate upon the experiment in this range.

Failure analysis was conducted on failed devices. The only failure mechanism discovered was failure due to copper pad pullout. Copper pads from the PWB make contact with solder balls from the BGA to create the electrical interconnects. The copper pad pullout failure mechanism occurs when one of the copper pads delaminates from the PWB and pulls away from the board, while remaining attached to the solder ball from the BGA. A cross sectioned example of this failure mechanism generated in this testing is shown in Figure 5.6.

The data resulting from the experiments outlined in this paper was compared to data found in the literature. Varghese and Dasgupta conducted a series of bending experiments using BGA devices [13]. These experiments used a 256 I/O full array package with a 1 mm pitch made by a different manufacturer than those studied in this paper. A different test board was used for the experiment. Two testing methods were used, one being a four point bend test on a servo-hydraulic testing machine similar to the setup used in the paper, and the other being an impact test that again utilized a four point bend setup. A variety of PWB strain rates were evaluated, ranging from 2.5E-3/s to 2.2E0/s. Documented failure mechanisms included bulk

solder failure and copper trace failure. The data from these experiments and the data generated in this paper are plotted together in Figure 5.7. Despite the many differences between the two experiments, the two sets of data are in reasonable agreement. A power law fit was performed on the combined set of data, and the R^2 value was calculated to be 0.89. The fact that independently generated data correlates well with the data from this paper underscores the validity of this study. Additionally, the close agreement of the two data sets indicates the possibility of generating a master failure curve that can be used to describe the failure of BGA devices irrespective of failure mechanism, testing methodology, and package manufacturer. This failure curve could then be used to create a failure model that can quickly predict the life of a BGA device subjected to a known PWB strain, regardless of the failure mechanism.

Conclusion

An experimental effort has been conducted to generate bending failure data for BGA devices in the ultra low cycle regime. This data has been compared to an independent published data set and found to be in close agreement, even though it differed with respect to the observed failure mechanism, test methodology, part manufacturer, and PWB strain rate. This agreement, along with the closeness of the low cycle fatigue exponent to the classic Manson value, is a strong indicator for the validity of the data. The ability to incorporate data representing different failure mechanisms, part manufacturers, and test methodologies into a single master curve is

advantageous for the development of a rapid assessment model to predict the reliability of a BGA device.

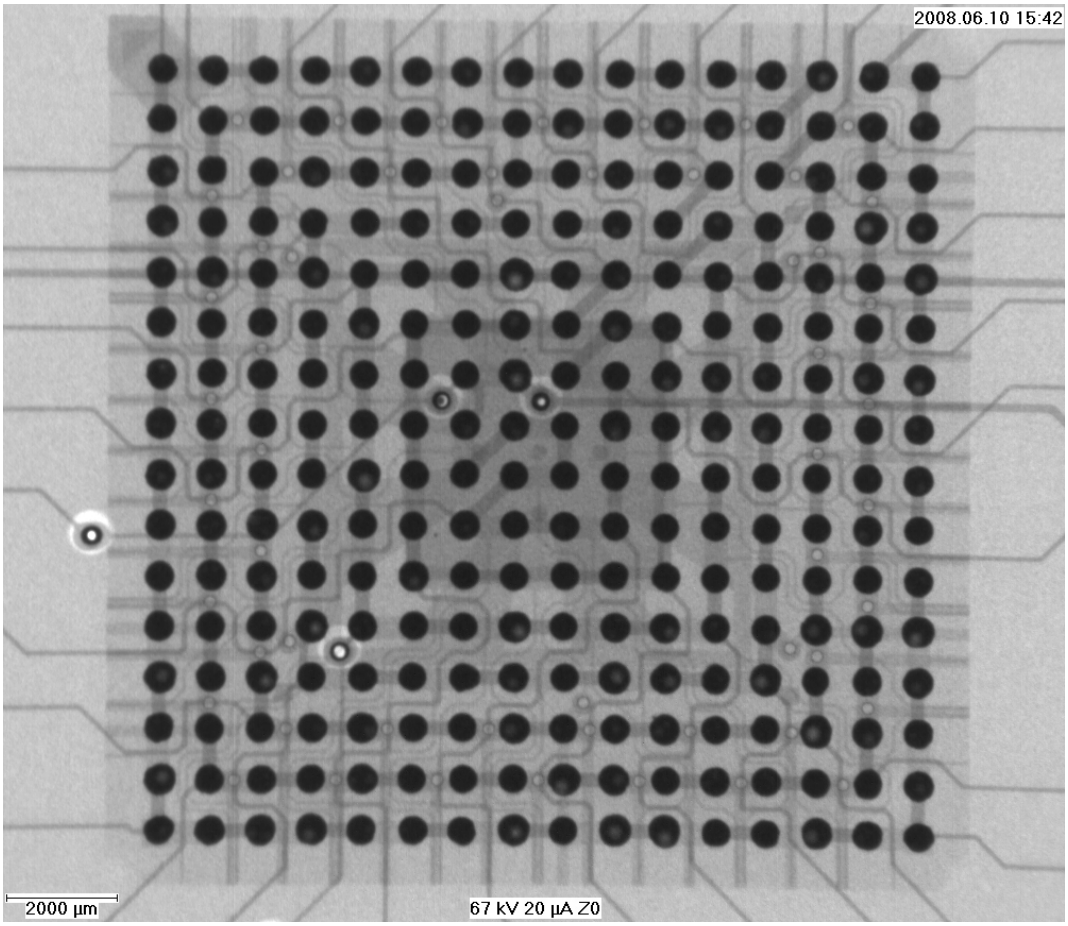

Figure 5.1: X-ray image of BGA component selected for evaluation.

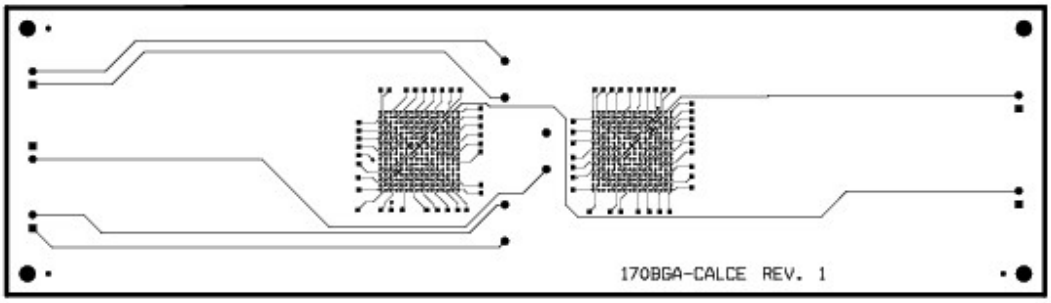

Figure 5.2: Schematic of BGA test coupon.

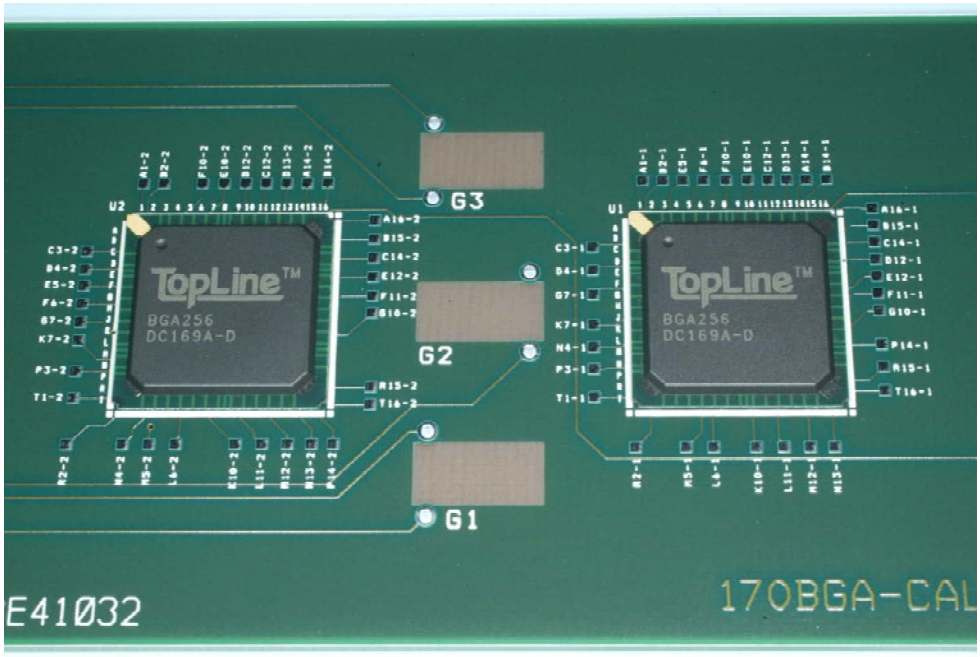

Figure 5.3: Close up of center portion of BGA test coupon.

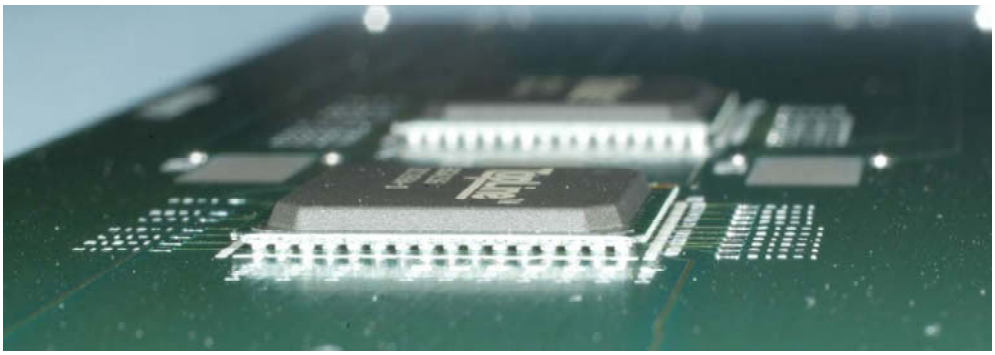

Figure 5.4: Side view of BGA devices mounted on test coupon.

Cycles to Failure	Strain Level	Strain Rate
2	12083	0.1/s
2	12365	0.1/s
2	12365	0.1/s
2	12239	0.1/s
3	11273	0.1/s
3	13035	0.1/s
3	13035	0.1/s
4	11273	0.1/s
4	11229	0.01/s
5	12239	0.1/s
10	8373	0.01/s
11	11229	0.01/s
11	8840	0.1/s
11	7410	0.01/s
16	7563	0.1/s
18	7563	0.1/s
19	8840	0.1/s
26	7597	0.1/s
215	2924	0.01/s
287	2924	0.01/s

Table 5.1: BGA experimental data.

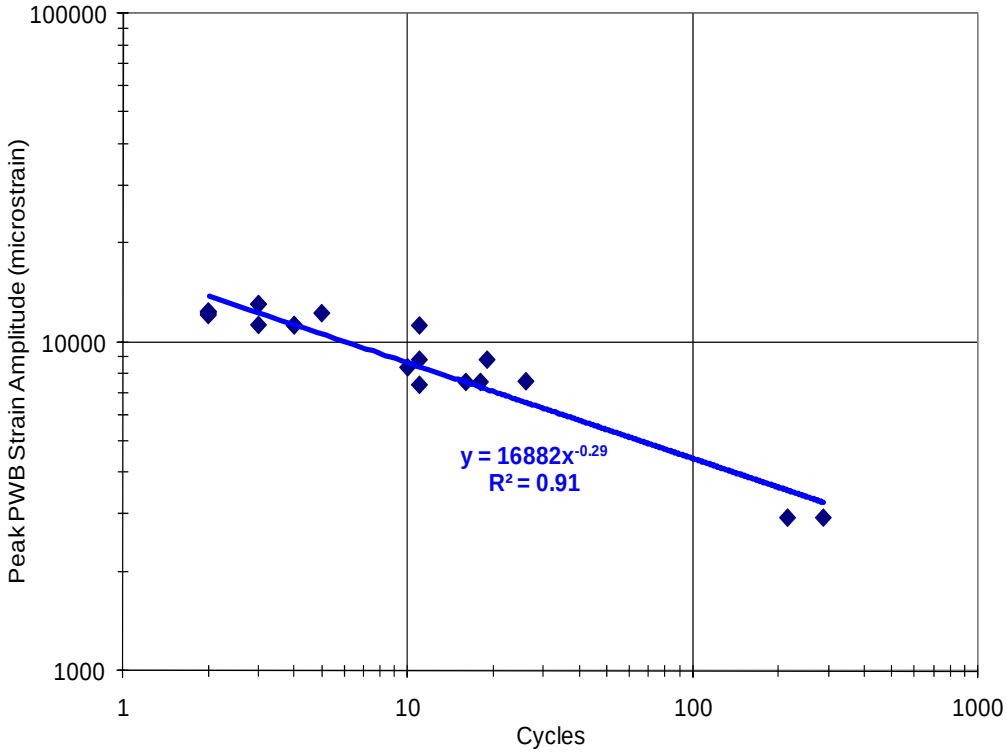

Figure 5.5: Strain vs. cycle plot of BGA failure data.

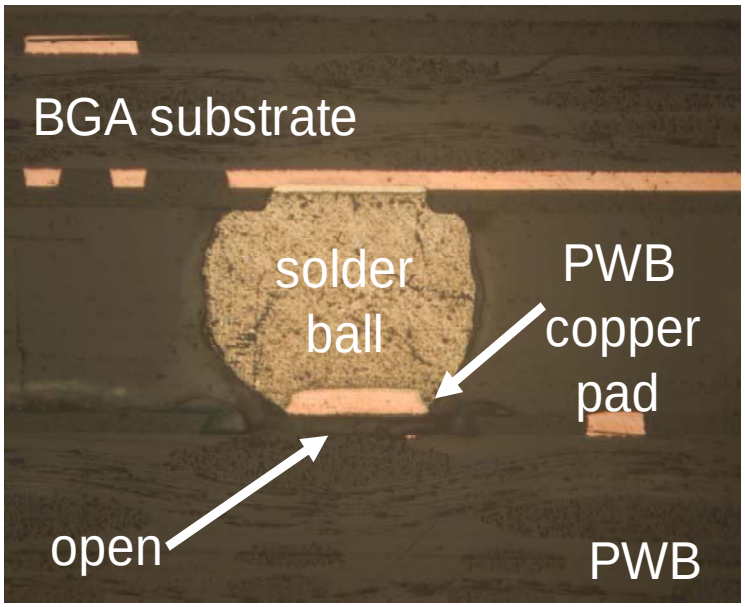

Figure 5.6: Cross section of failed BGA showing copper pad pullout.

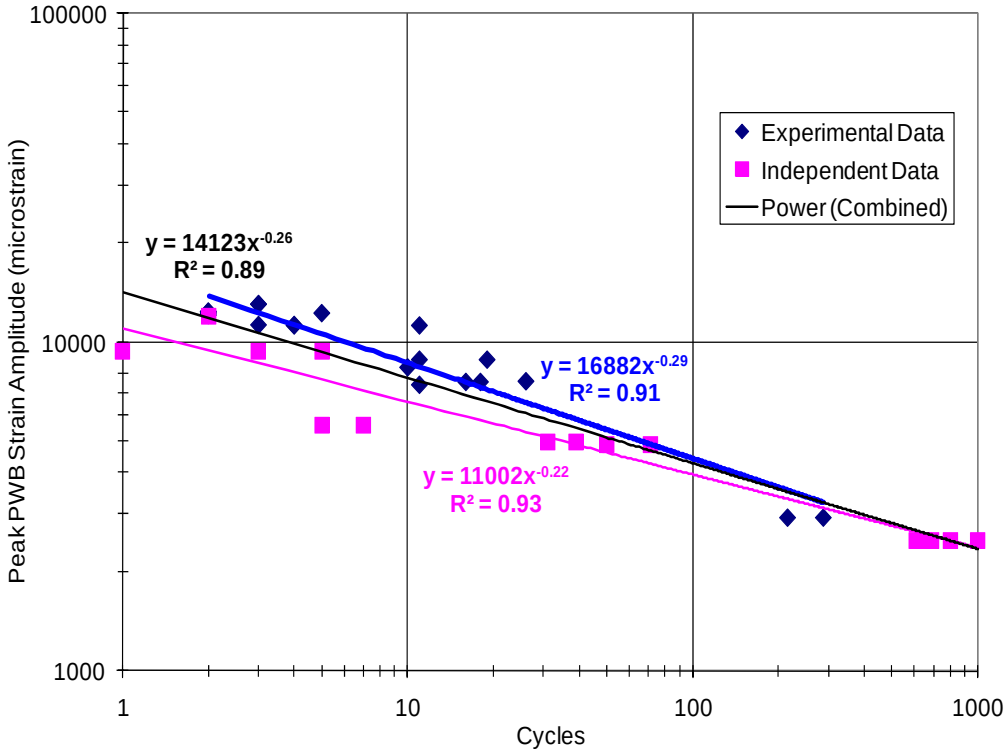

Figure 5.7: Experimental BGA data plotted with independent data.

Chapter 6: Conclusions, Contributions, and Future Work

Conclusions and Contributions

A number of important contributions to the field of electronic packaging come from this work. The first is the rate dependency of failure for MLCC devices. Testing size 1206 MLCC devices at PWB strain rates of up to 0.1/s saw failure at a PWB maximum strain value of around 3500 με. However, the high rate experiments performed in this work at PWB strain rates greater than or equal to 1/s recorded failures at PWB maximum strain values as low as 260 με, an over one order of magnitude lower value. This large discrepancy clearly indicates rate dependant behavior in MLCC devices. Failure at a lower maximum PWB strain value is believed to be due to strain rate hardening in the solder. Solder is known to have strain rate dependent material properties. In lower rate testing, the solder behaves more compliantly and mitigates a larger amount of stress in the ceramic. However as the loading rate is increased, strain hardening in the solder increases its effective elastic modulus which results in a higher stress load transferred to the ceramic. Thus, the component fails at a lower maximum PWB strain value. These results have a substantial impact on the design specifications of electronic assemblies intended for high rate loading environments. Those wishing to implement these parts in designs for high rate loading environments are warned that the part reliability will decrease dramatically with increasing loading rate. Designers should seek to implement parts with a smaller footprint to hedge against this decline in reliability.

Standard termination capacitors were shown to outperform their flexible termination equivalents in high rate loading. This result was unexpected since flexible termination parts show a great performance advantage over standard termination in medium to low rate bending (PWB strain rate $\leq$ 0.1/s). Flexible termination parts showed good performance when testing at a PWB strain rate of 1/s and a maximum PWB strain ranging from 260με to 450με (depending on the components location on the test board). Size 1206 flexible termination parts had 1.4% (4 out of 296) failed versus two different manufacturers size 1206 standard termination parts with failure percentages of 34.8% (103 out of 296) and 40.9% (121 out of 296). Size 0603 flexible termination parts and standard termination parts both had 0.7% (2 out of 296) failed at these test conditions. However, when testing was performed at a PWB strain rate of 5/s and a maximum PWB strains ranging from 509με to 1006με, size 1206 flexible termination parts had 96.6% (286 out of 296) of components on the board fail. Size 0603 flexible termination parts had 43.6% (129 out of 296) of components fail. Comparing these numbers to the two size 1206 standard termination part failure percentages of 68.2% (202 out of 296) and 31.1% (92 out of 296) and the size 0603 standard termination failure percentage of 0% (0 out 296), the standard termination parts show a clear advantage. These results have significant impact on component selection criteria for electronic assemblies expected to see any type of high rate loading. Flexible termination parts have become the go-to component for any application where bending loads are an issue, but design engineers should carefully evaluate the application's loading rate regime to determine if the

parts are acceptable for use. Counter to common intuition, the standard termination equivalent part may be the more reliable choice in high loading rate environments.

A new failure mechanism was discovered for flexible termination capacitors subjected to high rate bending. This mechanism involves the delamination of the tin-nickel and silver filled epoxy layers in the metallization end cap. The occurrence of this failure mechanism is the reason that standard termination capacitors outperform their flexible termination equivalents in the high rate environment. This failure mechanism was the cause of all of the failures in the testing conducted on size 1206 parts at a PWB strain rate of 5/s, in which 96.6% (286 out of 296) of components failed. The previously undocumented failure mechanism is believed to be attributed to strain rate hardening in the silver filled epoxy. The less compliant epoxy does not mitigate as much stress in the system, and the adhesion forces between the tin-nickel layer and the silver filled epoxy layer are not high enough to withstand this increased stress load.

The failure of BGA devices subjected to quasi-static bending loads was found to fall on a single master curve for failures in the ultra low cycle regime. This was the case even when data was compared with independently generated data that differed with respect to the observed failure mechanism, test methodology, part manufacturer, and PWB strain rate. The ability to incorporate data representing different failure mechanisms, part manufacturers, and test methodologies into a single master curve is advantageous for the development of a rapid assessment model to predict the reliability of a BGA device.

Future Work

Evaluating MLCCs at high loading rates

To continue to refine an understanding of the behavior of MLCC devices in high rate bending, the experimental campaign begun in this work should be continued. This work would involve a number of additional tests. A round of additional drop testing would be conducted using a drop tower capable of higher acceleration loads to result in a higher failure percentage for the smaller sized standard termination capacitors, sizes 0603 and 0402. The tests performed in this work were done at the maximum acceleration level possible on the drop tower used, and thus it was not possible to achieve a higher number of failures for the smaller parts.

Shaker table testing should be performed, in which the test board is loaded at its natural frequency, making the strain rate equivalent to that obtained in the drop tower testing. The amplitude of the load would be adjusted to obtain an equivalent level of PWB strain to the drop testing. A shaker table is capable of producing a clean loading function, and would eliminate the unknown contribution of the transient response resulting from a drop event.

The scope of the experimental test matrix should also be expanded to include additional component manufacturers. The selection of flexible termination parts in particular should be expanded. This study investigated the Syfer FlexiCap™ line of flexible termination capacitors. Future work should include additional flexible termination parts such as the AVX FlexiTerm™ line, as well as additional standard termination part manufacturers such as Murata, TDK, and Vishay.

The effect of lead free solder should also be investigated for the high rate loading of MLCCs. Azarian et al. investigated the influence of lead free solder for quasi static bend testing of MLCC devices, and found that reliability increased with its use [6]. The boards in this dissertation were assembled using standard 60/40 Sn/Pb eutectic solder. As the industry shifts away from leaded solder, the effects of its lead free alternative must be explored.

Silver Filled Epoxy Investigation

The new failure mechanism for MLCCs discovered as a result of this work involves the delamination of the tin-nickel and silver filled epoxy layers in the metallization end cap. An investigation of the properties of the silver filled epoxy used in this application must be conducted to determine the root cause of this failure mechanism. One investigation should seek to determine the relationship of the elastic modulus to strain rate. This relationship would allow the influence of strain rate hardening in the epoxy on the failure mechanism to be determined. The adhesion strength between the silver filled epoxy and the tin-nickel plating and its dependence on strain rate must also be determined. This study would result in the stress needed to cause the delamination effect seen in the new failure mechanism. Upon discovering the rate dependant properties of the epoxy, an LS-DYNA model could be created taking them into account to determine the stress at the epoxy/tin-nickel interface. With the adhesion strength known, the hypothesis citing strain rate hardening in the epoxy as the cause for delamination could be verified or disproved.

BGA Device Testing

The failure data for BGA devices should be expanded, with additional test replicates run in the loading region established in this work as well as at lower stress values to obtain failures in the 1000 and 10000 cycle range. Lead free solder should be evaluated along with standard leaded eutectic solder. BGA packages from different manufactures, packages with different total I/O (256 I/O packages were investigated in this study), and packages with a different pitch size (1.0 mm pitch was investigated in this study) should all be evaluated and compared against the current data to determine if the apparent master failure curve continues to accurately describe part failure. This work is already in progress and will be part of an upcoming doctoral dissertation.

Appendix A: Quasi-static Bend Testing of MLCC Components

Experimental setup

A four-point bend setup was chosen to achieve a constant bending moment in the center region of the sample board where the components were located. Figure A.1 shows a schematic of this setup. The impulse load was applied using an MTS servo-hydraulic test machine, which is capable of ram speeds up to 11 in/s. Each of the test boards was instrumented with strain gauges in the component region of the board.

The component evaluated in this study was a size 1206 Kemet standard termination MLCC. The dielectric type was X7R, the capacitance value was 2.2μF, and the voltage rating was 16V. In addition to this component, one board populated Syfer FlexiCap™ components and one board populated with CalChip Y5V 1.0μF components were evaluated in this study.

Test boards were fabricated and populated with the components that were to be evaluated. Figure A.2 shows the test board. The six strain gage sites are visible in the central portion of the board. This board was used to evaluate chip capacitors and chip resistors, and the board shown in Figure A.2 is populated with chip resistors. The capacitors were mounted on the board in the locations for size 1206 resistors, allowing 32 capacitors to be tested per board. The 32 locations on the board for size 0603 components were not utilized in this testing.

Since continuity monitoring is nontrivial for capacitors, each capacitor was both visually and electronically evaluated after the delivery of each successive bending impulse. Electronic evaluation was performed via a Sencore Z-meter, a device for measuring capacitance. The failure of a capacitor is defined as a 10% decrease in capacitance as determined by this meter.

Experimental Results

Seven total capacitor boards were tested at various strain levels. Table A.1 summarizes the capacitor results.

Upon cross sectioning the failed capacitors, cracks were discovered in the lower portion of the component near the PWB. These cracks were found to occur in the ceramic portion of the capacitor, and in severe cases, to extend through the solder fillet and end cap metallization. Figure A.3 shows a number of cross sectioned capacitors exhibiting this type of cracking.

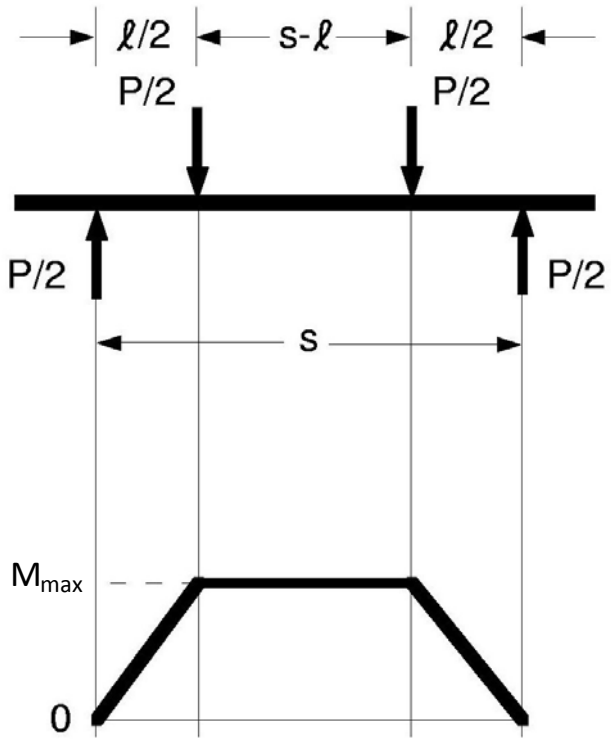

Figure A.1: Schematic of four-point bend setup.

Figure A.2: Chip component test board used for capacitor testing.

Board ID	Maximum PWB Strain (με)	Board Radius of Curvature (mm)	Parts Failed / Total
1	8834	91.4	32/32
2	10686	71.3	29/32
4	4126	184.7	24/32
5	4368	174.5	3/32
6	3770	202.1	26/32
7[1]	4317	176.5	2/12
8[2]	3791	201.0	4/28

Table A.1: Capacitor results for four-point bending experiment.

[1]Tested Syfer FlexiCap™ capacitors
[2]Tested CalChip Y5V, 1μF capacitors

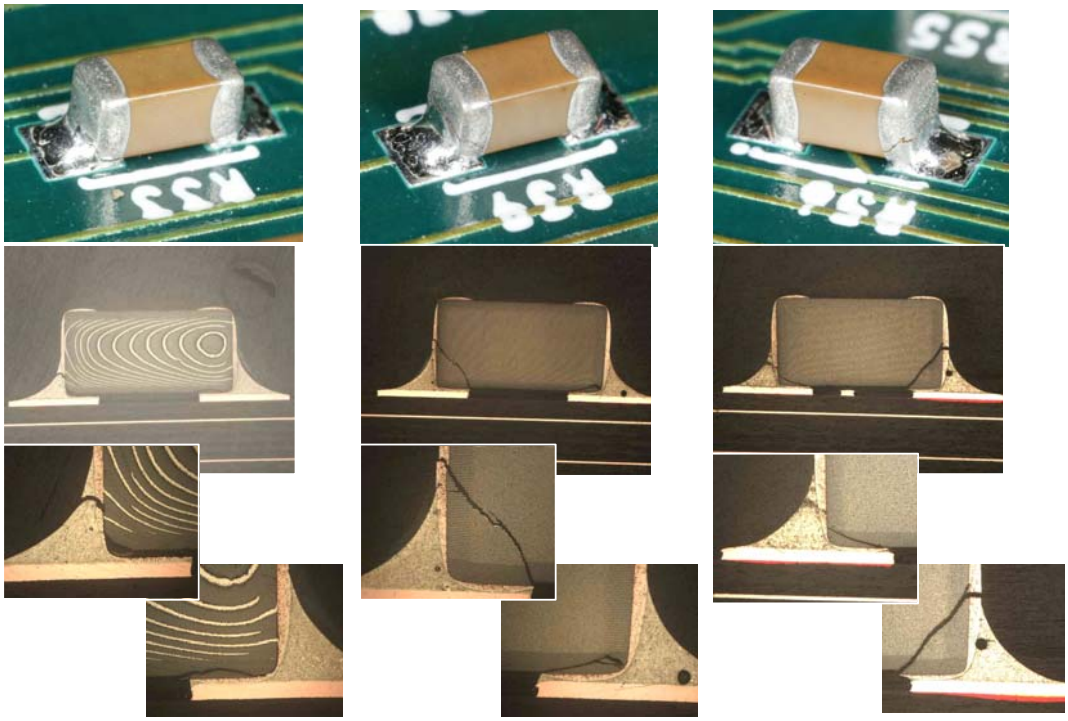

Figure A.3: Cross sectioned capacitors with flex cracks.

Appendix B: Experimental Data for MLCC Drop Testing

The following tables list all results for the drop tower testing of capacitors discussed in Chapters 3 and 4 of this dissertation. Table B.1 lists the results for the whole test board, while tables B.2 through B.7 break down the results according to the ring location on the test board. Results are also broken down by board side. Failures listed for the gaged side of the board occurred on the top of the board surface for the drop event. This top board side (gaged side) saw a compressive loading for the initial deflection of the test board.

For board ID 3 which is populated with size 0402 Kemet components, it was discovered that the test fixture was not fully tightened during the drop event. This data was not included in any of the dissertation chapters, and is listed here only for completeness.

Board ID	Part Size	Manufacturer	Termination	Board Center	# Failed Gaged Side	# Failed Bottom Side	# Failed Total	% Failed
n/a	1206	Kemet	standard	free	52	51	103 / 296	34.80
n/a	1206	Syfer	flexible	free	2	2	4 / 296	1.35
1	0603	Kemet	standard	free	1	1	2 / 296	0.68
2	0603	Syfer	flexible	free	2	0	2 / 296	0.68
3	*0402*	*Kemet*	*standard*	*free*	*8*	*8*	*16 / 296*	*5.41*
4	1206	AVX	standard	free	78	43	121 / 296	40.88
5	0603	Kemet	standard	free	0	0	0 / 296	0.00
6	0402	Kemet	standard	free	2	0	2 / 296	0.68
7	1206	Kemet	standard	fixed	96	106	202 / 296	68.24
8	1206	AVX	standard	fixed	26	66	92 / 296	31.08
9	1206	Syfer	flexible	fixed	142	144	286 / 296	96.62
10	0603	Kemet	standard	fixed	0	0	0 / 296	0.00
11	0603	Syfer	flexible	fixed	45	84	129 / 296	43.58
12	0402	Kemet	standard	fixed	4	2	6 / 296	2.03

Table B.1: Summary of MLCC drop testing data for the entire test board.

Board ID	Part Size	Manufacturer	Termination	Board Center	# Failed Gaged Side	# Failed Bottom Side	# Failed Total	% Failed
n/a	1206	Kemet	standard	free	8	8	16 / 16	100.0
n/a	1206	Syfer	flexible	free	1	2	3 / 16	18.75
1	0603	Kemet	standard	free	1	1	2 / 16	12.50
2	0603	Syfer	flexible	free	0	0	0 / 16	0.00
3	*0402*	*Kemet*	*standard*	*free*	*1*	*1*	*2 / 16*	*12.50*
4	1206	AVX	standard	free	8	8	16 / 16	100.0
5	0603	Kemet	standard	free	0	0	0 / 16	0.00
6	0402	Kemet	standard	free	0	0	0 / 16	0.00
7	1206	Kemet	standard	fixed	3	0	3 / 16	18.75
8	1206	AVX	standard	fixed	2	0	2 / 16	12.50
9	1206	Syfer	flexible	fixed	6	6	12 / 16	75.00
10	0603	Kemet	standard	fixed	0	0	0 / 16	0.00
11	0603	Syfer	flexible	fixed	2	1	3 / 16	18.75
12	0402	Kemet	standard	fixed	0	0	0 / 16	0.00

Table B.2: Summary of MLCC drop testing data for Ring A.

Board ID	Part Size	Manufacturer	Termination	Board Center	# Failed Gaged Side	# Failed Bottom Side	# Failed Total	% Failed
n/a	1206	Kemet	standard	free	15	10	25 / 32	78.13
n/a	1206	Syfer	flexible	free	1	0	1 / 32	3.13
1	0603	Kemet	standard	free	0	0	0 / 32	0.00
2	0603	Syfer	flexible	free	0	0	0 / 32	0.00
3	*0402*	*Kemet*	*standard*	*free*	*0*	*0*	*0 / 32*	*0.00*
4	1206	AVX	standard	free	8	13	21 / 32	65.63
5	0603	Kemet	standard	free	0	0	0 / 32	0.00
6	0402	Kemet	standard	free	1	0	1 / 32	3.13
7	1206	Kemet	standard	fixed	16	16	32 / 32	100.0
8	1206	AVX	standard	fixed	4	15	19 / 32	59.38
9	1206	Syfer	flexible	fixed	16	16	32 / 32	100.0
10	0603	Kemet	standard	fixed	0	0	0 / 32	0.00
11	0603	Syfer	flexible	fixed	7	13	20 / 32	62.50
12	0402	Kemet	standard	fixed	0	0	0 / 32	0.00

Table B.3: Summary of MLCC drop testing data for Ring B.

Board ID	Part Size	Manufacturer	Termination	Board Center	# Failed Gaged Side	# Failed Bottom Side	# Failed Total	% Failed
n/a	1206	Kemet	standard	free	4	3	7 / 64	10.94
n/a	1206	Syfer	flexible	free	0	0	0 / 64	0.00
1	0603	Kemet	standard	free	0	0	0 / 64	0.00
2	0603	Syfer	flexible	free	0	0	0 / 64	0.00
3	*0402*	*Kemet*	*standard*	*free*	*1*	*3*	*4 / 64*	*6.25*
4	1206	AVX	standard	free	4	11	15 / 64	23.44
5	0603	Kemet	standard	free	0	0	0 / 64	0.00
6	0402	Kemet	standard	free	0	0	0 / 64	0.00
7	1206	Kemet	standard	fixed	32	32	64 / 64	100.00
8	1206	AVX	standard	fixed	14	32	46 / 64	71.88
9	1206	Syfer	flexible	fixed	32	32	64 / 64	100.00
10	0603	Kemet	standard	fixed	0	0	0 / 64	0.00
11	0603	Syfer	flexible	fixed	10	22	32 / 64	50.00
12	0402	Kemet	standard	fixed	3	2	5 / 64	7.81

Table B.4: Summary of MLCC drop testing data for Ring C.

Board ID	Part Size	Manufacturer	Termination	Board Center	# Failed Gaged Side	# Failed Bottom Side	# Failed Total	% Failed
n/a	1206	Kemet	standard	free	5	1	6 / 64	9.38
n/a	1206	Syfer	flexible	free	0	0	0 / 64	0.00
1	0603	Kemet	standard	free	0	0	0 / 64	0.00
2	0603	Syfer	flexible	free	0	0	0 / 64	0.00
3	*0402*	*Kemet*	*standard*	*free*	*0*	*0*	*0* / 64	*0.00*
4	1206	AVX	standard	free	11	0	11 / 64	17.19
5	0603	Kemet	standard	free	0	0	0 / 64	0.00
6	0402	Kemet	standard	free	0	0	0 / 64	0.00
7	1206	Kemet	standard	fixed	31	31	62 / 64	96.88
8	1206	AVX	standard	fixed	2	19	21 / 64	32.81
9	1206	Syfer	flexible	fixed	32	32	64 / 64	100.0
10	0603	Kemet	standard	fixed	0	0	0 / 64	0.00
11	0603	Syfer	flexible	fixed	9	14	23 / 64	35.94
12	0402	Kemet	standard	fixed	0	0	0 / 64	0.00

Table B.5: Summary of MLCC drop testing data for Ring D.

Board ID	Part Size	Manufacturer	Termination	Board Center	# Failed Gaged Side	# Failed Bottom Side	# Failed Total	% Failed
n/a	1206	Kemet	standard	free	16	8	24	40.00
n/a	1206	Syfer	flexible	free	0	0	0	0.00
1	0603	Kemet	standard	free	0	0	0	0.00
2	0603	Syfer	flexible	free	0	0	0	0.00
3	*0402*	*Kemet*	*standard*	*free*	*1*	*2*	*3*	*5.00*
4	1206	AVX	standard	free	25	4	29	48.33
5	0603	Kemet	standard	free	0	0	0	0.00
6	0402	Kemet	standard	free	0	0	0	0.00
7	1206	Kemet	standard	fixed	10	11	21	35.00
8	1206	AVX	standard	fixed	0	0	0	0.00
9	1206	Syfer	flexible	fixed	27	29	56	93.33
10	0603	Kemet	standard	fixed	0	0	0	0.00
11	0603	Syfer	flexible	fixed	5	20	25	41.67
12	0402	Kemet	standard	fixed	0	0	0	0.00

Table B.6: Summary of MLCC drop testing data for Ring E.

Board ID	Part Size	Manufacturer	Termination	Board Center	# Failed Gaged Side	# Failed Bottom Side	# Failed Total	% Failed
n/a	1206	Kemet	standard	free	4	21	25	41.67
n/a	1206	Syfer	flexible	free	0	0	0	0.00
1	0603	Kemet	standard	free	0	0	0	0.00
2	0603	Syfer	flexible	free	2	0	2	3.33
3	*0402*	*Kemet*	*standard*	*free*	*5*	*2*	*7*	*11.67*
4	1206	AVX	standard	free	22	7	29	48.33
5	0603	Kemet	standard	free	0	0	0	0.00
6	0402	Kemet	standard	free	1	0	1	1.67
7	1206	Kemet	standard	fixed	4	16	20	33.33
8	1206	AVX	standard	fixed	4	0	4	6.67
9	1206	Syfer	flexible	fixed	29	29	58	96.67
10	0603	Kemet	standard	fixed	0	0	0	0.00
11	0603	Syfer	flexible	fixed	12	14	26	43.33
12	0402	Kemet	standard	fixed	1	0	1	1.67

Table B.7: Summary of MLCC drop testing data for Ring F.

References

[1] J. D. Prymak and J. Berganthal. "Capacitance monitoring while flex testing." IEEE Transactions on Components, Packaging, and Manufacturing Technology, Part A, Vol. 18, No. 1, pp. 180–186, March 1995.

[2] C. Hillman, N. Blattau, and D. Barker. "Design Guidelines for Avoiding Flex Cracking in Ceramic Capacitors." Global SMT and Packaging, Vol. 3, No. 1, pp. 18-21, January/February 2003.

[3] L. Condra, G. Johnson, M. Pecht, and A. Christou. "Evaluation of Manufacturing Variables in the Reliability of Surface Mount Capacitors." IEEE Transactions on Components, Hybrids, and Manufacturing Technology, Vol. 15, No. 4, pp. 542-552, Aug. 1992.

[4] N. Blattau. "Models for Rapid Assessment of Leadless Component Failures During Printed Wiring Board Bending." Ph.D. Dissertation, 2004.

[5] R. Al-Saffar, R. Freer, I. Tribick, and P. Ward. "The Flexure Strength of Multilayer Ceramic Capacitors." British Ceramic Proceedings, Vol. 59, pp. 61-73, 1999.

[6] M. Keimasi, M. Azarian, and M. Pecht. "Isothermal Aging Effects on Flex Cracking of Multilayer Ceramic Capacitors with Standard and Flexible Terminations." Microelectronics Reliability, Vol. 47, pp. 2215-2225, 2007.

[7] K. Franken, H. R. Maier, K. Prume, and R. Waser. "Finite element analysis of ceramic multilayer capacitors: Failure probability caused by wave soldering

and bending loads." Journal of American Ceramic Society, 83 (6), pp. 1433-40, 2000.

[8] M. Azarian, M. Keimasi, and M. Pecht. "Flex Cracking of Multilayer Ceramic Capacitors Assembled with Lead-Free and Tin-Lead Solders." IEEE Transactions on Device and Materials Reliability, Vol. 8, Issue 1, pp 182-192, March 2008.

[9] J. Varghese and A. Dasgupta. "Test methodology for durability estimation of surface mount interconnects under drop testing conditions." Microelectronics Reliability. Vol. 47, Is. 1, pp. 93-103. January 2007.

[10] C. Lim and Y. Low. "Investigating the drop impact of portable electronic products." IEEE Electronic Components and Technology Conference. Proceedings. 52nd. pp. 1270-1274, 2002.

[11] C. Lim, C. Ang, L. Tan, S. Seah, E. Wong. "Drop impact survey of portable electronic products." IEEE Electronic Components and Technology Conference. Proceedings. 53rd. pp. 113-120, 2003.

[12] S. Seah, C. Lim, E. Wong, V. Tan, and V. Shim. "Mechanical response of PCBs in portable electronic products during drop impact." IEEE Electronics Packaging Technology Conference. 4th. pp. 120-125, 2002.

[13] J. Varghese and A. Dasgupta. "An experimental approach to characterize rate-dependent failure envelopes and failure site transitions in surface mount assemblies." Microelectronics Reliability. Vol. 47, Is. 7, pp. 1095-1102. July 2007.

[14] Z. Cheng, W. Huang, X. Cai, B. Xu, L. Luo, X. Li. "A Study of Packaging Effect on the Performance of MEMS for high-G Accelerometer." Electronic Materials and Packaging, 2002. Proceedings of the 4th International Symposium on 4-6 Dec. 2002. pp. 231-238.

[15] T. Brown, B. Davis, D. Hepner, J. Faust, C. Myers, P. Muller, T. Harkins, M. Hollis, C. Miller, B. Placzankis. "Strap-Down Microelectromechanical (MEMS) Sensors for High-G Munition Applications." IEEE Transactions on Magnets, vol. 37, no. 1, Jan 2001.

[16] T. Brown. "Harsh Military Environments and Microelectromechanical (MEMS) Devices." Sensors, 2003. Proceedings of the IEEE, vol. 2, pp. 753-760, Oct. 22-24, 2003.

[17] G. Katulka. "Micro-electromechanical Systems and Test Results of SiC MEMS for High-g Launch Applications." Sensors, 2002. Proceedings of the IEEE, vol. 2, pp. 1134-1138.

[18] Q. Guo, M. Zhao, L. Wei. "SMT Solder Joint's Shape and Location Optimization Using Genetic Algorithm with Neural Networks in High Acceleration Condition." Proc 24th International Conference on Microelectronics (MIEL 2004). Vol 2, Nis, Serbia and Montenegro, 16-19 May, 2004.

[19] J. Hill-Lindsay, J. Yuen. "High G Impact Resistant Digital Data Recorder for Missile Flight Testing." Nonvolatile Memory Technology Review, pp. 109-110, June 22-24, 1993.

[20] IPC/JEDEC-9702, Monotonic Bend Characterization of Board-Level Interconnects, June 2004.

[21] D. Rooney, N. T. Castello, M. Cibulsky, D. Abbott, D. Xie. "Materials Characterization of the Effect of Mechanical Bending on Area Array Package Interconnects." Microelectronics Reliability, vol. 44, 2004.

[22] P. Geng, P. Chen, Y. Ling. "Effect of Strain Rate on Solder Joint Failure Under Mechanical Load." 2002 Electronic Components and Technology Conference.

[23] K. Jonnalagadda. "Reliability of Via-in-pad Structures in Mechanical Cycling Fatigue." Microelectronics Reliability, vol. 42, 2002.

[24] U. D. Perera. "Evaluation of Reliability of μBGA Solder Joints Through Twisting and Bending." Microelectronics Reliability, vol. 39, 1999.

[25] P. L. Tu, Y. C. Chan, K. C. Hung, J. K. L. Lai. "Comparative Study of Micro-BGA Reliability Under Bending Stress." IEEE Transactions On Advanced Packaging, vol. 23, no. 4, Nov. 2000.

[26] L. Leicht, A. Skipor. "Mechanical Cycling Fatigue of PBGA Package Interconnects." Microelectronics Reliability, vol. 40, 2000.

[27] A. Eslambolchi, P. Johnson, M. Kaufmann, Z. Mei. "Electroless Ni/Immersion Au Evaluation – Final Program Report." Hewlett Packard Electronic Assembly Development Center, September 14, 1998.

[28] E. Bradley, K. Banerji. "Effect of PCB Finish on the Reliability and Wettability of Ball Grid Array Packages." IEEE Transactions on Components, Packaging, and Manufacturing Technology, Part B: Advanced Packaging, vol. 19, issue. 2, May 1996.

[29] R. Coyle, D. Hodges Popps, A. Mawer, D. Cullen, G. Wenger, P. Solan. "The Effect of Modifications to the Nickel/Gold Surface Finish on Assembly Quality and Attachment Reliability of a Plastic Ball Grid Array." IEEE Transactions on Components and Packaging Technologies, vol. 26, no. 4, December 2003.

[30] Z. Mei, M. Kaufmann, A. Eslambolchi, P. Johnson. "Brittle Interfacial Fracture of PBGA Packages Soldered on Electroless Nickel / Immersion Gold." 1998 Electronic Components and Technology Conference.

[31] J. Lee, M. Rassaian. "Effective Local Flexural Stiffness of Ball Grid Array Assemblies." Journal of Electronic Packaging, vol. 124, September 2002.

[32] A. Skipor, L. Leicht. "Mechanical Bending Fatigue Reliability and its Application to Area Array Packaging." 2001 Electronic Components and Technology Conference.

[33] P. Roubaud, G. Ng, G. Henshall, S. Prasad, F. Carson, R. Bulwith, R. Herber, S. Kamath, A. Garcia. "Impact of Intermetallic Growth on the Mechanical Strength of Lead-Free BGA Assemblies." IPC SMEMA Council APEX 2001.

[34] P. Geng, R. Aspandiar, T. Byrne, F. Pon, D. Suh, A. McAllister, A. Nazario, P. Paulraj, N. Armendariz, T. Martin, T. Worley. "Alternative Lead-free Solder Joint Integrity Under Room Temperature Mechanical Load." 2004 Inter Society Conference on Thermal Phenomena.

[35] G. Dieter. "Mechanical Metallurgy." McGraw Hill, Boston, MA. 3rd ed, 1986.

[36] A. Boresi and R. Schmidt. "Advanced Mechanics of Materials." John Wiley & Sons, Inc. 6th ed, 2003.